

2015-01-01

Evaluating Methods Of Field-Based 3D Visualization And Their Application To Mapping Metamorphic Terranes: An Example From The Panamint Mountains, California

Jade Ashley Brush

University of Texas at El Paso, jabrush@miners.utep.edu

Follow this and additional works at: https://digitalcommons.utep.edu/open_etd



Part of the [Geology Commons](#), and the [Geotechnical Engineering Commons](#)

Recommended Citation

Brush, Jade Ashley, "Evaluating Methods Of Field-Based 3D Visualization And Their Application To Mapping Metamorphic Terranes: An Example From The Panamint Mountains, California" (2015). *Open Access Theses & Dissertations*. 1004.
https://digitalcommons.utep.edu/open_etd/1004

This is brought to you for free and open access by DigitalCommons@UTEP. It has been accepted for inclusion in Open Access Theses & Dissertations by an authorized administrator of DigitalCommons@UTEP. For more information, please contact lweber@utep.edu.

EVALUATING METHODS OF FIELD-BASED 3D VISUALIZATION AND
THEIR APPLICATION TO MAPPING METAMORPHIC TERRANES: AN
EXAMPLE FROM THE PANAMINT MOUNTAINS, CALIFORNIA

JADE ASHLEY BRUSH

Department of Geological Sciences

APPROVED:

Terry L. Pavlis, Ph.D., Chair

José M. Hurtado Jr., Ph.D.

Jeffrey R. Knott, Ph.D.

Charles Ambler, Ph.D.
Dean of the Graduate School

Copyright ©

by

Jade Ashley Brush

2015

Dedication

This thesis is dedicated to Margret “Lit” Brush, my grandmother, who inspired my interest in geology and the Death Valley region.

EVALUATING METHODS OF FIELD-BASED 3D VISUALIZATION AND THEIR
APPLICATION TO MAPPING METAMORPHIC TERRANES: AN EXAMPLE FROM THE
PANAMINT MOUNTAINS, CALIFORNIA

by

JADE ASHLEY BRUSH

B.S.

Presented to the Faculty of the Graduate School of

The University of Texas at El Paso

in Partial Fulfillment

of the Requirements

for the Degree of

MASTER OF SCIENCE

Department of Geological Sciences

THE UNIVERSITY OF TEXAS AT EL PASO

May 2015

Acknowledgements

I would like to acknowledge Margret “Lit” Brush for letting us use her home as a basecamp during our time in the field. I would also like to acknowledge Joshua Cobb for taking the time to be my field partner, driver, and companion. I would also like to thank Mark Nelson for answering my numerous questions about *Maptek I-Site* and Keith Williams of UNAVCO for his assistance with the LiDAR field-work and post-field questions. Finally, I would like to thank Carlos Montana for installing all of the software for this research.

Abstract

Field geology has traditionally relied on 2D, paper-based workflows, but digital mapping techniques are rapidly replacing these outdated methods because they allow for more efficient and accurate mapping. This research applies digital mapping techniques and two terrestrially-based 3D visualization technologies, photogrammetry and Light Detection and Ranging (LiDAR), to the study of metamorphic terranes in the Panamint Mountains, California. This study reports on the spatial accuracy of TINs (triangulated irregular networks) generated from both photogrammetry and ground-based LiDAR using a terrestrial laser scanner (TLS) and discusses how spatial accuracy can be increased. Two levels of comparison were used to test spatial accuracy. First, the TINs generated from photogrammetry were directly compared to those generated from the TLS in 3D space. The second level of comparison involved making geologic interpretations on both the photogrammetrically- and TLS-derived terrain models and qualitatively comparing them in 2D space to interpretations made in the field. In both levels of comparison, spatial accuracy of the photogrammetrically-derived TINs depends primarily on the ratio between the length of the baseline (line that connects the camera positions) and the distance to the farthest feature in the scene, the number and distribution of ground control points, the number of photographs taken, model error, and GPS precision. The final analysis compared orientation measurements taken from LiDAR-derived TINs to orientations taken from the field. Orientations obtained from LiDAR-derived TINs in areas that could not be reached in the field can supplement field orientation, thus filling in data gaps to yield a more complete understanding of the structure. The workflows developed in this research represent a step toward implementing

3D visualizations into field studies, particularly studies of metamorphic terranes. These workflows may change the way geologists approach field work.

Keywords: 3D visualization; photogrammetry; LiDAR; metamorphic terranes

Table of Contents

Acknowledgements	v
Abstract	vi
Table of Contents	viii
List of Tables	x
List of Figures	xi
List of Plates	xvii
1. Introduction.....	1
2. Study area	4
3. Background.....	6
3.1 Digital technology in field geology	6
3.2 Geology of Pleasant Canyon.....	9
4. Methods	17
4.1 Field methods.....	17
4.2 Office data processing.....	21
5. Results.....	32
5.1 Comparison of 3D terrain models.....	32
5.2 3D interpretation comparison on 2D map.....	34
5.3 Stereonet comparison.....	36
6. Discussion.....	39
6.1 Structural history of Pleasant Canyon.....	39
6.2 Sources of error for photogrammetrically-derived TINs	39
6.3 Sources of error in 3D interpretations.....	44
6.4 Discrepancies in the orientation comparison	45
6.5 Insights into developing photogrammetric terrain models from this work.....	45

7. Conclusions.....	51
References.....	54
Tables.....	64
Figures.....	71
Plates.....	111
Appendix 1.....	113
Appendix 2.....	114
Appendix 3.....	122
Curriculum Vita	124

List of Tables

Table 1. Strain measurements collected from stretched pebbles within the South Park Member of the Kingston Peak Formation. Section 1 represents measurements collected in the foliation plane. Section 2 represents measurements collected perpendicular to lineation. The lengths of the long and short axes of a pebble are measured and the ellipticity is calculated by dividing the length of the short axis by the length of the long axis. The reciprocal is calculated by dividing the length of the short axis by the length of the long axis. Harmonic mean is the number of measurements divided by the sum of the reciprocals and maximum ellipticity is the product of the harmonic means from each section.	64
Table 2. Table of the software used in this research including the version number. The table also includes the purpose for which the software was used.	66
Table 3. Calibration parameters for both the Clair Camp and Noonday Structures. The initial values are the calibration parameters that <i>PhotoScan</i> calculates based on the settings entered (i.e. brand and type of camera, focal length, etc.). The adjusted values represent the parameters calculated after alignment. fx, fy = focal length in the x and y dimensions; cx,cy = principal point coordinates; skew = transformation coefficient, k1 – k4 = radial distortion coefficients; and p1, p2 = tangential coefficients.	67
Table 4. Table containing the number of points within the TLS- and photogrammetrically-derived point clouds of the Clair Camp and Noonday Structures. The table includes the original amount of points that each point-cloud started with prior to processing, the number of points remaining in each point-cloud after removing stray points (clean-up), and the number of points remaining in each point-cloud after applying a 0.45 m filter. No filter was applied to the photogrammetrically-derived point-cloud of the Noonday Structure as it was not necessary. This table shows that the number of points remaining after clean-up is higher for the photogrammetrically-derived point-clouds than the TLS-derived point-clouds.	68
Table 5. Table of ten offset measurements between photogrammetrically-derived TINs and TLS-derived TINs for both the Clair Camp and Noonday Structures. The table also includes offset measurements between the marker-less Clair Camp TIN and the TLS-derived Clair Camp TIN. Average offsets are included at the bottom of the table in highlighted in yellow.	69
Table 6. Table with measurements from the laser sight test. Measurements include range (in meters) and inclination (in degrees). For inclination of the laser rangefinder, horizontal is measured at 90° and values that are less than 90° indicates that the laser was oriented below horizontal. The user successfully hit the target at all designated intervals as the range measured is within centimeters of the actual distance.	70

List of Figures

Figure 1. Photograph of the equipment used for digital field geologic mapping. This research utilized (1.) a GPS (Global Positioning System) receiver connected wirelessly to (2.) an Asus Tablet via Bluetooth, and (3.) A Trimble TDS Recon Pocket PC (Personal Computer) connected to (4.) a LaserCraft Contour XLRic Laser Rangfinder via a serial cable. The Trimble TDS Recon allows for a GPS (Global Positioning System) receiver to be connected to the top. A recording compass inclinometer (5.) was also used in this research..... 71

Figure 2. Map from Google Earth showing the location of Pleasant Canyon west of Death Valley National Park as represented by the green line. The locations of Ballarat and Clair Camp are labeled for reference. The black line represents the graded gravel road from Ballarat to Pleasant Canyon. The light blue line traces the floor of Pleasant Canyon. The area mapped in this study is outlined by a dark blue line. Within the mapped area are the two locations chosen for 3D surface analysis in this study. The red polygon outlines the Clair Camp Structure and the orange polygon (its southern boundary is the floor of Pleasant Canyon) represents the area modeled to make the Noonday Structure. 72

Figure 3. Diagram of the ideal setup for photogrammetry. The baseline between the two camera positions is twice as long as the distance to feature i . The shaded area represents the stereo coverage of the two cameras. Variables used to calculate the coordinates (x_i and y_i) of feature i include: focal length of the cameras (f_1 and f_2), orientation angle of the cameras (δ_1 and δ_2), position of feature i from the center of the image plane from both cameras (C_1 and C_2), ray from the camera positions to feature i (d_i), the angle between the lens axes and d_i (α_1 and α_2), and the angle between d_i and the x -axis for both camera positions (Φ_1 and Φ_2). Modified from Wolf, 1983..... 73

Figure 4. Geologic map of the southern Telescope Peak Quadrangle showing the location of Pleasant Canyon. Tbk = Metasedimentary clasts derived from the Kingston Peak Formation. Tbn = Sedimentary clasts derived from the Noonday Dolomite. Modified from Labotka et al. (1980). 74

Figure 5. Stereonets of poles to planes of S1 foliation strike and dips (left), and the trend and plunge (right) of lineations ($L_{1\min}$ and $L_{1\text{ext}}$) with 1% area contour. The S1 foliation poles show dominantly west dipping structure and lineations trend north-south..... 75

Figure 6. Flinn Diagram of the length of stretched pebbles from the South Park Member of the Kingston Peak Formation. The length of pebbles is measured in the foliation plane (X/Y) and perpendicular to lineation (Y/Z). The harmonic mean of the data plots in the LS-tectonite section within the constriction field. Refer to Table 1 for the measurements used to generate this Flinn Diagram..... 76

Figure 7. Foliation (S1) axial planar to isoclinal folds within the Noonday Dolomite. Photograph taken on the southern wall of Pleasant Canyon. 77

Figure 8. Example of top-north shear within the mylonitic granodiorite (Kmg). Photograph was taken near the mouth of Pleasant Canyon on the northern canyon wall.	78
Figure 9. Stereonet plot of poles to planes of crenulation cleavage (S3) associated with D3. The best fit great circle has a strike and dip of 245.9/68.5° and a π -pole that plunges 21.5° toward 155.9.	79
Figure 10. Photograph of the reverse fault in the mylonitic granodiorite (Kmg) slightly east of the South Park Fault. The mylonitic granodiorite intrusion is in the hanging wall as well as the footwall of the reverse fault.	80
Figure 11. Example dialog boxes from <i>ArcPad</i> Version 10 used for digital mapping in this research. This figure shows the type of data that can be collected when drawing contacts (left) and recording structural orientations (right). Detailed descriptions of the digital mapping workflow can be found Pavlis et al. (2010).	81
Figure 12. Geologic map of Pleasant Canyon focusing on the Clair Camp Structure (north of Clair Camp). Thirteen marker points (green flags) are located throughout the Clair Camp Structure chosen for photogrammetry. Five camera positions (white circles with crosses) are located south of Clair Camp.	82
Figure 13. Geologic map of Pleasant Canyon focusing on the Noonday Structure (north wall of Pleasant Canyon that includes the Noonday Dolomite). No marker points were obtained in the field, but ten camera positions (white circles with crosses) are located on the southern ridge of Pleasant Canyon.	83
Figure 14. Photograph of the Riegl LMS-Z620 TLS used to collect LiDAR data of Pleasant Canyon. The Riegl LMS-Z620 is equipped with a differential GPS receiver and has a Nikon D700 camera mounted on top. This photograph was taken at the Clair Camp site looking southwest.	84
Figure 15. Screenshot of the <i>PhotoScan</i> project for the Clair Camp Structure. In the viewing pane (right) image 7810 is selected from the “Photos” window (bottom right). Within the viewing pane, images can be masked. This screenshot shows the sky has been masked, as denoted by the dark blue color and gray outline along the ridge. The viewing pane is also where marker points are placed in photographs (four of the eight marker points are located in image 7810 and represented by green flags). The GPS coordinates (latitude, longitude, and elevation) for each of the marker points are entered into the “Markers” table (middle left window). GPS coordinates for the camera positions are entered into the “Cameras” table (upper left window). Once camera positions are entered, each photograph can be selected and assigned to the camera position where the photograph was taken.	85
Figure 16. Image from <i>PhotoScan</i> showing the photogrammetrically-derived point-cloud of the Noonday Structure including the locations of the eight marker points (green flags) obtained from the LiDAR point-cloud. This image also includes the ten camera positions (circled crosses) and	

the rays representing the lens axis of each photograph taken (photographs are represented as blue planes) at each camera position. 86

Figure 17. Dense points-clouds of the Clair Camp Structure (top) and the Noonday Structure (bottom) made using *PhotoScan* and viewed using *Maptek I-Site*. The dense point-cloud of the Clair Camp Structure was made using the ultra-high setting, while the dense point-cloud of the Noonday Structure was made using the high setting. Refer to text for further description..... 87

Figure 18. Screenshot showing the photograph draping process in *I-Site*. This example is of the Clair Camp Structure. The dialog box (left) contains the photograph being draped. A feature is chosen in the photograph and manually selected to create a point and then the same feature is manually selected in the model to create a point pair. 88

Figure 19. Image showing a close-up of the photogrammetrically-derived terrain model of the Noonday Structure. The interpretation in green represents the base of the Noonday Dolomite. On steep cliff faces, the interpretation shows errors in the Z-direction..... 89

Figure 20. Image of the photogrammetrically-derived terrain model of the Clair Camp Structure with 3D interpretations viewed in *I-Site*. pCks = Surprise Member of the Kingston Peak Formation, pCkq = Quartzite unit within the Kingston Peak Formation, pCkd = Dolomite Marble unit within the Kingston Peak Formation, and pCkc = Calc-silicate Mineralization within the Kingston Peak Formation. 90

Figure 21. Image of the TLS-derived terrain model of the Clair Camp Structure with 3D interpretations viewed in *I-Site*. pCks = Surprise Member of the Kingston Peak Formation, pCkq = Quartzite unit within the Kingston Peak Formation, pCkd = Dolomite Marble unit within the Kingston Peak Formation, and pCkc = Calc-silicate Mineralization within the Kingston Peak Formation. 91

Figure 22. Image of the photogrammetrically-derived terrain model of the Noonday Structure with 3D interpretations viewed in *I-Site*. pCnd = Noonday Dolomite, and pCsl = Sourdough Limestone Member of the Kingston Peak Formation..... 92

Figure 23. Image of the TLS-derived terrain model of the Noonday Structure with 3D interpretations viewed in *I-Site*. pCnd = Noonday Dolomite, and pCsl = Sourdough Limestone Member of the Kingston Peak Formation..... 93

Figure 24. Diagram showing the general workflow used to build a point-cloud using photogrammetry. Sage green boxes represents the steps that were taken in the field, black boxes represent steps required to build a point-cloud using *PhotoScan*, red boxes represent potential issues, and the blue box represents processing in *Maptek I-Site*. 94

Figure 25. Diagram showing the general workflow for collecting and processing TLS data. The green box represents the step performed in the field, the black boxes represent the steps required to process the TLS point-cloud using *RiScan Professional*, the blue boxes represent the steps

required to build terrain models using *Maptek I-Site*, the red boxes represent potential issues, and the orange box represents additional processing in *MOVE*. 95

Figure 26. Image of the visual comparison viewed in *I-Site* between the marker-less photogrammetrically-derived TIN of the Clair Camp Structure (blue), the TLS-derived TIN (pink), and the photogrammetrically-derived TIN of the Clair Camp Structure that utilized marker points (green). The TLS-derived TIN (pink) is used as a reference. The marker-less photogrammetrically-derived TIN (blue) is located well above the TLS-derived TIN, while the photogrammetrically-derived TIN that utilized marker points (green) is situated slightly underneath the TLS-derived TIN of the Clair Camp Structure. 96

Figure 27. Image of the result of surface analysis in *I-Site*. This image shows the photogrammetrically-derived TIN of the Clair Camp Structure colored by the amount it is offset from the TLS-derived TIN of the Clair Camp Structure. Areas that are colored yellow indicate that that area is situated above the surface of the TLS-derived TIN of the Clair Camp Structure, and areas that are colored blue are situated below the surface of the TLS-derived TIN. 97

Figure 28. MATLAB figure showing the calculations for the amount of offset between ten control points located on the photogrammetrically-derived TIN of the Clair Camp Structure (red circles) and their counterparts on the TLS-derived TIN of the Clair Camp Structure (blue circles). Distance and direction of offset is indicated by the blue line connected pairs of circles. This figure shows that offset between points increases the farther the points are from the origin (camera positions). 98

Figure 29. MATLAB figure showing the calculations for the amount of offset between ten control points located on the marker-less photogrammetrically-derived TIN of the Clair Camp Structure (red circles) and their counterparts on the TLS-derived TIN of the Clair Camp Structure (blue circles). Distance and direction of offset is indicated by the blue line connected pairs of circles. This figure shows that offset between points increases the farther the points are from the origin (camera positions). 99

Figure 30. MATLAB figure showing the calculations for the amount of offset between ten control points located on the photogrammetrically-derived TIN of the Noonday Structure (red circles) and their counterparts on the TLS-derived TIN of the Noonday Structure (blue circles). Distance and direction of offset is indicated by the blue line connected pairs of circles. This figure shows that offset between points increases the farther the points are from the origin (camera positions). 100

Figure 31. Map view of interpretations from the Clair Camp Structure made using *MOVE*: blue lines are interpretations that were made in the field, pink lines are interpretations that were made using the TLS-derived terrain model, and green lines are interpretations that were made using the photogrammetrically-derived terrain model of the Clair Camp Structure. The terrain model-derived interpretations follow the trend of the field interpretations, but deviate at the ridge (north end of the map). 101

Figure 32. Images from *I-Site* showing the photogrammetrically-derived point-cloud (green) and the TLS-derived point-cloud (true color) of the Noonday Structure before registration (top) and after registration (bottom). The TLS-derived point-cloud of the Noonday Structure was used as the reference for registration of the photogrammetrically-derived point-cloud. Registration resulted in a spatially accurate photogrammetrically-derived point-cloud of the Noonday Structure..... 102

Figure 33. Map view of interpretations from the Noonday Structure made using *MOVE*. All interpretations represent the base of the Noonday Dolomite. The blue line is the interpretation that was made in the field, the pink line is the interpretation made using the TLS-derived terrain model, the green line is the interpretation made using the photogrammetrically-derived terrain model, and the yellow line is the interpretation made using the registered photogrammetrically-derived terrain model of the Noonday Structure. All interpretations appear to follow the same trend in map view, except on the east side where the terrain model-derived interpretations deviate..... 103

Figure 34. Cross-section of interpretations from the Noonday Structure made using *MOVE*. All interpretations represent the base of the Noonday Dolomite. The blue line is the interpretation that was made in the field, the pink line is the interpretation made using the TLS-derived terrain model, the green line is the interpretation made using the photogrammetrically-derived terrain model, and the yellow line is the interpretation made using the registered photogrammetrically-derived terrain model of the Noonday Structure. All of the terrain model-derived interpretations appear to follow the same trend, but the field interpretation has a unique character. The reason the field interpretation is different from the terrain model interpretations is most likely due to the limitations of mapping contacts on cliff faces using a 2D map..... 104

Figure 35. Stereonets of poles to planes of the S1 strike and dip orientations collected in the field (top) and extracted from the TLS-derived terrain model (bottom) of the Clair Camp Structure. Both stereonet show dominantly west dipping foliation that scatters from shallow to steep dips as a result of the fold in foliation. The mean principal pole for the orientations obtained from the TLS-derived terrain model plunges 65° toward 075, whereas the mean principal pole from the field orientations plunges 40° toward 090. The stereonet of terrain model-derived orientations from the Clair Camp Structure (bottom) is more scattered along a great girdle than the orientations from the field, providing a clearer definition of the fold orientation for this structure. 105

Figure 36. Stereonets of poles to planes of the S1 strike and dip orientations collected in the field (top) and extracted from the TLS-derived terrain model (bottom) of the Noonday Structure. The mean principal pole from the field orientations from the Noonday Structure is similar to the mean principal pole of the terrain model-derived orientations. The field orientations plunge 75° toward 090 while the terrain model-derived orientations show a mean principal pole that plunges 75° toward 080. The TLS-derived measurements deviate significantly from the field orientations. Independent measurements of small scale folds and fabrics through the area demonstrate that the field data give the proper fold orientation, raising questions on the source of errors in the TIN analysis..... 106

Figure 37. Stereonets of poles to planes of the S1 strike and dip orientations collected in the field (top) and extracted from the TLS-derived terrain model (bottom) representing the entire mapped area of Pleasant Canyon. The mean principal pole from the field orientations is similar to the mean principal pole of the terrain model-derived orientations. The field orientations plunge 55° toward 090 while the terrain model-derived orientations show a mean principal pole that plunges 65° toward 075. The TLS-derived measurements deviate significantly from the field orientations may reflect measurement bias in the field and attempting to obtain measurements on cliff faces from the terrain models. 107

Figure 38. Geologic map of the Clair Camp Structure showing the baseline-to-distance ratio for the photogrammetric array. The angular field of view for each camera position is assumed to be 60° for a 35 mm focal length. Each field of view is oriented so that the optic axis (dashed blue line) is aligned to the farthest feature in the scene (represented by a star). The shaded red area represents the stereo coverage of the array. The baseline is a black dashed line connecting the two most distance camera positions (white circles with crosses) in the array, and a black dashed line is drawn perpendicular to the baseline to the farthest feature producing a baseline-to-distance ratio of 0.35. 108

Figure 39. Geologic map of the Noonday Structure showing the baseline-to-distance ratio for the photogrammetric array. The angular field of view for each camera position is assumed to be 60° for a 35 mm focal length. Each field of view is oriented so that the optic axis (dashed blue line) is aligned to the farthest feature in the scene (represented by a star). The shaded red area represents the stereo coverage of the array. The baseline is a black dashed line connecting the two most distance camera positions (white circles with crosses) in the array, and a black dashed line is drawn perpendicular to the baseline to the farthest feature producing a baseline-to-distance ratio of 1.125. 109

Figure 40. Diagrams showing simplified camera orientations for the Noonday Structure (top) and the Clair Camp Structure (bottom). For the Noonday Structure the optic axis of the camera (dashed black line) was generally oriented perpendicular to the feature being captured. For the Clair Camp Structure, the optic axis of the camera was oriented oblique to the feature being captured. In order to orient the optical axis of a camera perpendicular to the surface of features, such as the Clair Camp Structure, the photographs (or LiDAR scans) must be taken from the air as shown by the blue dashed line. 110

List of Plates

Plate 1. Geologic map of Pleasant Canyon created using the digital mapping techniques described in the text and finalized using ArcGIS. Refer to text for a detailed description of map units and structure. 111

Plate 2. Cross-section of Pleasant Canyon from A-A' on the map (Plate 1). All contacts represent the base of units and the colors of these contacts are the same as the colors on the map (Plate 1). F2 and F3 axial surfaces are labeled and S1 and S3 foliation traces (thin black lines and dark pink lines, respectively) are also present. Kmg = Mylonitic granodiorite, pCnd = Noonday Dolomite, pCksl = Sourdough Limestone Member of the Kingston Peak Formation, pCkb = Basalt Amphibolite unit within the Kingston Peak Formation, pCks = Surprise Member of the Kingston Peak Formation, pCkq = Quartzite unit within the Kingston Peak Formation, pCkd = Dolomite Marble unit within the Kingston Peak Formation, pCkc = Calc-silicate Mineralization within the Kingston Peak Formation, pCqf = Quarzofeldspathic Gneiss. 112

1. Introduction

Geologic study is grounded in basic field work. However, the tools remain relatively unchanged over the last century. Rugged handheld computers and tablets, field Geographic Information System (GIS) software, Global Positioning System (GPS) receivers, high resolution aerial and satellite imagery, detailed topographic datasets, position logging compass inclinometers, digital cameras, and laser rangefinders (Figure 1) are just some of the digital tools suitable for field investigation. Compared to traditional paper mapping, field geologists utilizing these technologies in the field can greatly improve efficiency by increasing accuracy of geolocation, reducing the amount of time spent recording and plotting data, and reducing the amount of time required to draft a finalized map.

Field structural analysis of metamorphic terranes was first described in a book by Sander (1930) that was later translated to English (Turner and Weiss, 1963). The techniques outlined in these works still remain the basis for the way most geologists perform field structural analyses. This approach involves recognizing multiple generations of fabrics, using styles and geometries for grouping generations, systematically measuring linear and planar elements, and attempting to combine the field data on a fixed-scale map. This two-dimensional (2D) approach also includes making 2D cross-sections and stereonet plots (Ramsay and Huber, 1983, 1987; Ramsay and Lisle, 2000). Although this approach is a useful foundation for understanding metamorphic terranes, it is inherently 2D and there are technologies now available that can improve these techniques by making the approach easier, more efficient, and more accurate.

Pavlis et al. (2010) challenged field geologists to adapt digital geologic field work methods (“digital mapping”) and abandon the traditional paper and pen mapping methods that

date as far back as William Smith (1769-1839) and the first geologic maps. Pavlis et al. (2010) promoted the use of various technologies (i.e., tablet computers, digital inclinometers, digital cameras and GPS receivers). Pavlis et al. (2010) stated that metamorphic terranes are often complicated by multiple generations of folding and faulting that require collection of overlapping point and polyline data that often make traditional paper geologic maps illegible. Applying digital mapping techniques to mapping metamorphic terranes improves situational awareness and map legibility. However, applying digital mapping to understanding metamorphic terranes is still a 2D approach to a three-dimensional (3D) problem.

A possible solution to the visualization issues that arise when mapping complex metamorphic terranes is to integrate digital mapping with 3D visualizations. To do this, the 3D visualizations need to accurately represent the terrain being studied, and the interpretations made using the 3D visualizations must correctly correspond spatially to interpretations made in the field. The primary technologies used to achieve 3D visualizations suitable for geologic studies are ground-based LiDAR (Light Detection and Ranging) using a terrestrial laser scanner (TLS) and photogrammetry. The latter has existed for decades, but the development of the structure from motion algorithm (Taylor and Kriegman, 1995) and its incorporation in user-friendly software has the potential to revolutionize 3D studies.

In this study both of these technologies are used to collect large volumes of spatial and geometric data in the field to develop a high resolution terrain model represented by a TIN (triangulated irregular network). A TIN is a vector-based representation of a surface derived from irregularly spaced points with 3D coordinates that are arranged in a network of non-overlapping triangles (Peucker et al., 1978). I evaluate structure from motion based TINs relative to TINs derived from a TLS using the TLS data as a reference because of the inherent a high

precision of this tool that typically allows measurements up to several hundreds of meters away. This study shows that the accuracy of photogrammetrically-derived TINs depends strongly on the ratio between the photographic baseline and distance to the farthest features in the scene as well as the number of photographs and the precision of ground control points used in model construction. These results are important for future studies to consider as these methods become more widespread. This study further considers assessments of geological mapping precision among 2D flat-map based approaches versus 3D mapping and uses these results to suggest modern workflows to incorporate these kinds of 3D data into geologic mapping.

2. Study area

In order to evaluate techniques for mapping complex metamorphic terranes the field site must contain a rock assemblage with readily recognizable rock units, enough outcrop to make rock units visible on imagery, and enough topographic relief to visualize structures in 3D. In addition, to evaluate terrain models derived from photogrammetry vs LiDAR requires sufficient topographic relief and access to apply these different techniques. A location that fits these criteria is Pleasant Canyon located on the western flank of the central Panamint Mountains in southern California just outside of the Death Valley National Park boundary (Figure 2). At the time of this writing, Pleasant Canyon is accessible via a graded gravel road from Ballarat. In this study I mapped an area that begins 380 m west of where the road reaches the floor of Pleasant Canyon and extends to 835 m east of Clair Camp representing a length of 5,730 m along the canyon floor (Figure 2). Pleasant Canyon is a classic wine-glass canyon ranging from zero width at the canyon mouth to ~ 2,000 m in the upper part of the mapped area. Total relief of Pleasant Canyon within the mapped area is 1,317 m.

Two outcrops on the north wall of Pleasant Canyon were chosen in the field for comparison of photogrammetry and TLS-derived TINs and associated geologic mapping. These sites were chosen because of conspicuous structures that are visible from the valley floor. The Clair Camp Structure in the eastern part of the mapped area was chosen for its clear exposure of several rock units and faults as well as modest terrain that allowed field access to rock exposures.

The second site is referred to here as the Noonday Structure. The Noonday Structure was chosen because the white marbles of the Noonday Formation contrast markedly with adjacent metasedimentary units allowing routine picking of lithologic contacts in imagery and the field.

The Noonday Structure also contrasts the Clair Camp Structure with exposure on steep to overhanging cliffs that is not accessible on foot.

3. Background

3.1 DIGITAL TECHNOLOGY IN FIELD GEOLOGY

Traditional methods for resolving structural geometries generally involve systematic mapping of the surface traces of different generations of structural fabrics, along with symmetry analyses (stereographic projection) and constructing cross-sections (Hobbs et al., 1976). These traditional procedures include manually recording strike and dip measurements of structural elements using a geologist's compass. To do so, the traditional geologist must stop, make two different measurements (strike and dip), record the two measurements (typically in a paper notebook), and then take the time to locate that point (typically on a paper map). This procedure is time consuming and the resulting paper maps are often cluttered and incomprehensible to anyone other than the person who did the mapping (Pavlis et al., 2010). Even for the person who did the mapping, quantitative analysis and manipulation of the map data, including visualization and querying, is cumbersome at best. Other issues with the traditional approach include (in)accuracy of data geolocation on paper maps and the fact that paper media is difficult to back-up, store, and transmit.

Digital mapping using a field GIS can eliminate the shortcomings of traditional paper mapping. The placement of orientation data and geologic interpretations on a digital map is more precise with a GIS system tied to a GPS receiver. Digital mapping is also scale-independent allowing the geologist to collect data and populate the map space at an arbitrary scale limited only by the precision of the GPS and the logistical constraints of field work. This means that the geologist can choose, on-the-fly, the appropriate map scale to collect the data needed for the site. Digital mapping also allows for compartmentalization of data into selectable layers that the user can turn on and off as desired. Scale independence and the compartmentalization of data into

selectable layers allows the map to be customized and queried to answer questions and visualize relationships in ways that are impossible with paper maps. A digital map essentially transforms geologic data into a database that can be interactively manipulated and explored visually and quantitatively in ways that can be customized and optimized for the task at hand.

Digital mapping today makes use of portable tablets or handheld computers. These devices can be interfaced with a laser rangefinder in order to accurately map features up to 1-3 km away, depending on the device. The laser rangefinder emits a laser pulse toward an object and calculates distance using the time it takes for the reflection to return to the laser rangefinder. When interfaced with a GPS-enabled computer, the distance translates to a point on the map and multiple points can connect to make lines.

A digital inclinometer allows the user to record strike /dip and trend/plunge at the same time and recorded, together with GPS-based positions, in a downloadable file (Figure 1). These orientations can then be downloaded to a computer and plotted on a digital map rather than manually entered into a notebook and hand-plotted on a paper map. The ability to download and plot orientations collected using a digital inclinometer allows the geologist to add as many orientation points as needed to the digital map at the end of a field day to aid situational awareness for the next day's work. Digital mapping tools and techniques serve to make geologic data more manageable, interactive, and transferable. However, in the context of mapping metamorphic terranes digital mapping is still a 2D approach to a 3D problem.

Technologies such as LiDAR and photogrammetry have been used to build 3D visualizations of surface geologic features (e.g. McCaffrey et al., 2008; Haneberg, 2008). A TLS utilizes pulsed LiDAR time-of-flight to collect 3D geospatial data. The high spatial and geometric accuracy of LiDAR-derived 3D visualizations is well known (e.g. Buckley et al.,

2008; Kurz et al, 2008; McCaffrey et al., 2008), but the equipment is expensive and a TLS can be difficult to transport to remote localities. Airborne LiDAR resolves the transport issue, but is expensive due to aircraft flight costs.

Photogrammetry is a method of recovering the three-dimensional geometry of objects visible in stereo pairs of photographs (or multiple photographs taken from different orientations) using knowledge of the imaging geometry and triangulation of a number of control points that are correlated from image to image (Wolf and Dewitt, 2000). Converting 2D images of 3D features into a 3D TIN involves sets of triangulation equations. By knowing the focal length, baseline, and camera orientation it is possible to calculate the distance to an object using parallax equations (Wolf, 1983: Figure 3). To obtain 3D coordinates of a feature within a 2D image, collinearity equations are used. Collinearity equations relate coordinates in the two-dimensional coordinate system of the image sensor plane within the camera to three-dimensional feature coordinates in the real world outside the camera (Wolf, 1983; Figure 3). The 3D coordinates, parameters of relative motion, and optical characteristics of the camera are refined using bundle adjustment. Bundle adjustment calculations are based on the bundles of light rays that originate from each 3D feature and converge on the camera's optical center and their geometries are defined by the collinearity equations (Wolf and Dewitt, 2000).

Although traditional photogrammetry has been used for decades, the development of the structure-from-motion algorithm (Taylor and Kriegman, 1995) has revolutionized photogrammetry by allowing the use of multiple oblique photographs taken from ground level rather than using nadir-looking aerial photographs. However, the use of oblique photographs is generally limited to “close-range” photogrammetry, meaning that the distance from the camera to the object is ≤ 300 m (Wolf and Dewitt, 2000). Since a digital camera (and optionally a tripod)

is the only equipment required for ground-based photogrammetry, this technique is more cost-effective than LiDAR and the equipment is easier to transport to remote locations than is a TLS.

3.2 GEOLOGY OF PLEASANT CANYON

The central Panamint Mountains are a metamorphic complex that consists of Precambrian basement overlain by Neoproterozoic metasedimentary rocks that were deposited during the initiation of the Cordilleran passive continental margin (Labotka et al., 1980). In the Late Triassic, subduction and arc magmatism interrupted the subsidence of the passive margin (Stevens et al., 1997). This tectonic regime continued through the Mesozoic and formed most of the Sierra Nevada batholith and is responsible for the plutonism metamorphism and deformation in the Panamint Mountains (Stevens et al., 1997; Labotka et al., 1980). Two phases of metamorphism of the central Panamint Mountains occurred as a result of large intrusions that were emplaced during this time of crustal compression. First, a Middle Jurassic (170 to 150 Ma) prograde metamorphism associated with the emplacement of granitic rocks in the Argus-Inyo-White Mountains when the Panamint Range was at ~10 km depth. The second phase is a Late Cretaceous (80 to 70 Ma) retrograde metamorphism associated with the emplacement of the 80 Ma Hall Canyon Pluton, located ~ 4.5 km north of Pleasant Canyon in Surprise Canyon, in the northern Panamint Mountains (Labotka and Albee, 1990; Labotka et al., 1980; Evernden and Kistler, 1970). Cretaceous metamorphism occurred along a low pressure-temperature (P-T) gradient to produce greenschist to amphibolite facies metamorphic rocks whose metamorphic grade decreases to the east (Labotka et al., 1980). Labotka et al. (1980) suggested that coaxial folding in the Mesozoic may have occurred during the emplacement of the Hall Canyon Pluton and seems to have reactivated preexisting dip-slip faults but results of this study indicate that interpretations is an oversimplification.

Basin and Range extension and unroofing of the Panamint metamorphic complex occurred during the Cenozoic (Wernicke et al., 1988; Labotka and Albee, 1990; Wernicke, 1992). There is debate about whether the Panamint Mountains were allochthonous during extension or if the extensional detachment tracks over the Panamint Mountains (Stewart, 1983; Norton, 2011). For this study, the key geologic context of the extensional tectonic system is that west-dipping, low-angle normal fault systems have exhumed a pre-extensional crustal section in the central Panamint Mountains. The pre-extensional crustal section contains highly metamorphosed, amphibolite facies metasedimentary rocks on the west side of the Panamint Mountains and unmetamorphosed to weakly metamorphosed, metasedimentary rocks on the east.

The study area in Pleasant Canyon is underlain by Proterozoic basement and overlying metamorphic strata of the Pahrump Group and the Noonday Dolomite (Figure 4). The Pahrump Group consists of the Crystal Spring Formation, the Beck Spring Dolomite, and the Kingston Peak Formation. The following description of rock units in Pleasant Canyon includes the results of previous work as well as observations from this study. The structural interpretations of Pleasant Canyon described here are the result of field work and digital mapping conducted during this study in support of the TIN analyses. The geologic map produced by the author using digital mapping techniques is introduced here for reference (Plate 1).

3.2.1 World Beater Complex

The oldest rock unit in Pleasant Canyon, the World Beater Complex, makes up the World Beater structural dome east of Clair Camp (Plate 1). Lanphere et al. (1964) used early geochronology techniques to conclude the World Beater Complex consists of a 1,800 Ma augen gneiss that is cross-cut by a 1,400 Ma quartz monzonite, which has been confirmed by modern geochronology (Cobb, 2015). The augen consist of potassium feldspar megacrysts in a biotite

mica groundmass with quartz + plagioclase ribbons that are 3-16 cm thick (this study). The World Beater Complex also contains inclusions of quartz-biotite-muscovite schist. The largest inclusion observed in this study is a band ~3 m thick. The mouth of Pleasant Canyon is underlain by another Precambrian basement rock, a leucocratic quartzofeldspathic gneiss (Labotka et al., 1980), that presumably is an equivalent of the basement assemblage exposed in the World Beater Complex.

3.2.2 Crystal Spring Formation

Weakly metamorphosed Crystal Springs Formation is exposed in the western part of the mapped area where it lies in structural contact with quartzofeldspathic basement gneiss (Plate 1). The contact between the gneissic rocks and the Crystal Springs Formation is a major, west-dipping low-angle normal fault with sinistral-oblique slickensides (South Park Fault). In exposures in Pleasant Canyon, the Crystal Springs Formation crops out as a tan-orange weathering dolomitic marble and purple slate. Outcrops also contain sparse amphibolite dikes with associated talc deposits typical of the middle Crystal Spring Formation. The Crystal Springs Formation in this area is brecciated due to the South Park Fault beneath it (Plate 1) Albee et al. (1981) mapped this brecciated unit as a Tertiary monolithologic breccia derived from the Noonday Dolomite, whereas Andrew and Walker (2009) showed the brecciated rocks as Neo-Mesoproterozoic metasedimentary rocks and basement gneisses in thrust contact with underlying rocks. The mapping described here supports the Andrew and Walker (2009) interpretation of the rock units. Nonetheless, the South Park Fault is demonstrably an oblique normal fault because it places very low-grade metamorphic rocks on medium grade rocks (Plate 1). The older-on-younger juxtaposition is interpreted as either a three-dimensional effect of oblique fault-slip or a

juxtaposition of a higher-level thrust sheet onto a more deeply exhumed metamorphic assemblage in the footwall of the normal fault.

3.2.3 Beck Spring Dolomite

Regionally, the Beck Spring Dolomite conformably overlies the Crystal Springs Formation and is a thick-bedded massive dolomitic marble (Labotka et al., 1980). However, the Beck Spring Dolomite is not found in Pleasant Canyon west of the World Beater Dome (Plate 1) and, according to Albee et al. (1981), it may have been removed by erosion along the unconformity below the overlying Kingston Peak Formation. However, that conclusion is suspect because the Kingston Peak contact with basement is a fault in Pleasant Canyon (Plate 1).

3.2.4 Kingston Peak Formation

The Beck Spring Dolomite is unconformably overlain by the Kingston Peak Formation. The stratigraphy of the Kingston Peak Formation has been extensively studied because of its implications for the Snowball Earth hypothesis (Hoffman and Schrag, 2002; MacDonald et al., 2013). In Pleasant Canyon (Plate 1), the base of the Kingston Peak Formation is not exposed, but above the structural contact with basement, the assemblage begins with a gray phyllite to mica schist. Intercalated within this phyllite-schist is a carbonate unit that has been metamorphosed to calc-silicates and an associated porphyroblastic garnet schist (Plate 1). This assemblage is within a mineralized zone that follows the trend of a presumably normal fault with a strike/dip of 16°/80° with slicken lines that have a trend/plunge of 46°→185° that was exploited by miners in the early 1900s (Ristorcelli and Schlitt, 2015).

The gray phyllite-schist with intercalated calc-silicates is overlain by a layered, gray-tan-orange boudinaged dolomite marble (Plate 1) that becomes interleaved with quartzite up-

structural pseudo-section until it grades into an orange-tan-gray laminated quartzite (Plate 1). The quartzite, in turn, grades into an argillite that marks the base of the first unequivocal unit of the Kingston Peak Formation, a dark brown diamictite (Plate 1). This quartzite-marble-argillite assemblage was mapped by Albee et al. (1981) to represent members of the Kingston Peak Formation, including their Limekiln Spring Member. Although this hypothesis is reasonable, the intensity of deformation in these units is such that this unit could (also) include rocks derived from the Crystal Spring Formation, Beck Spring Dolomite, or both.

The most extensive rock unit in the mapped area is a thick diamictite that makes up the Surprise Member of the Kingston Peak Formation (Albee et al., 1981). The unit becomes more carbonate-rich near the top. The transition from diamictite to more carbonate-rich lithology is marked by a dashed internal contact on the map (Plate 1). In the western part of the mapped area, the diamictite is interleaved with a dark gray to black amphibolite. In low-strain zones, these amphibolites show distinctive pillow structures with metamorphosed chilled margins, indicating these amphibolites originated as submarine basalt flows that were erupted during marine deposition of the Surprise diamictite (Plate 1). According to Labotka et al. (1980), this mafic igneous activity occurred over a large period of time in the Precambrian, but amphibolite is clearly syn-rift basalts associated with the formation of the Neoproterozoic rifted margin of western North America (Stewart and Suczek, 1977).

The Surprise Member is overlain by a thinly-laminated, gray limestone marble known as the Sourdough Limestone Member of the Kingston Peak Formation (Plate 1). The Sourdough marble is intensely deformed and shows evidence of refolding in Pleasant Canyon. The Sourdough Limestone Member is, in turn, overlain by lithologically diverse clastic metasedimentary rocks that include metamorphosed diamictites, quartzites, and conglomerates

that based on lithologic sequence probably constitute the South Park Member of the Kingston Peak Formation. The rocks of the South Park Member are intensely deformed to the point where the conglomerates contain stretched pebbles with high axial ratios, particularly rocks directly beneath the overlying Noonday marble (Table 1).

3.2.5 Noonday Dolomite

The youngest metasedimentary unit, the Neoproterozoic Noonday Dolomite, disconformably overlies the Pahrump Group (Plate 1). In the mapped area, The Noonday Dolomite is a thinly laminated white, gray, green, pink, tan, brown marble that forms bold cliffs and displays numerous small scale folds and refolded folds at a variety of scales. The Noonday Dolomite also contains thinly laminated siliceous dolomite marble.

3.2.6 Intrusions

A mylonitic granodiorite exposed near the western edge of the Pleasant Canyon map area (Plate 1) is the youngest rock unit mapped in this study. It has a U-Pb zircon age of 76.6 ± 0.8 Ma (Andrew, 2002). This rock intruded the amphibolite of the Kingston Peak Formation and was intensely deformed following emplacement (Plate 1).

3.2.7 Structure

The metamorphic rocks in the Pleasant Canyon area record clear evidence of two distinct ductile deformational events overprinted by brittle structures. The oldest recognized structures were observed primarily at mesoscopic scales. Larger, map-scale structures are present but inconspicuous on the geologic map (Plate 1). The oldest deformational event (D1) are recognized primarily as a prominent LS tectonite fabric that forms a layer-parallel continuous cleavage (S1) with an associated mineral ($L1_{min}$) and extension lineation ($L1_{ext}$) in most of the rocks (Figure 5).

Strain measurements taken on north-south trending stretched pebbles in the South Park Member of the Kingston Peak Formation yield a maximum ellipticity of ~11 and plot in the constrictional strain field on a Flinn Diagram, as expected for LS-tectonites (Table 1; Figure 6). The S1 foliation is demonstrably axial planar to mesoscopic isoclinal folds (F1) in thinly laminated rock types (schists and metasandstones), and folds of similar structural style in marbles are presumably of the same generation (Figure 7). The absence of large scale structures associated with D1 handicaps inference of the vergence of these structures, but mylonitic fabrics in Mesozoic plutonic rocks that appear to be of this generation show abundant evidence of a top to the north sense of shear (Figure 8). Though this top to the north shear seems to be part of the main fabric, the mylonitic granodiorite is Cretaceous in age (Andrew 2002), and new evidence suggests that the main north-south trending fabric may be Jurassic in age (Cobb, 2015). Thus, more work is needed to date the deformation in Pleasant Canyon.

The main continuous cleavage is overprinted by a second generation of structures (D2). The most prominent structures of this generation are shallowly-plunging, shallowly-to-moderately inclined, west-vergent folds (F2) in S1 foliation which can be seen on the map (Plate 1) and in the cross-section from A-A' (Plate 2). Evidence for F2 folding is most obvious in the Sourdough Limestone Member and other carbonate units in Pleasant Canyon where numerous S-shaped asymmetric folds (viewed looking north) can be seen on the lower limb of a large F2 synform (Plate 2). This west-vergent folding caused S1 foliations to rotate into a dominantly west-dipping orientation throughout the eastern part of the mapped area (Figure 5). At larger scale (Plate 2), foliation and the axial surface of the macroscopic F2 fold, are warped into an open, upright synform. This geometry suggests that a third generation of structures (D3) has overprinted the earlier generations to produce an east-vergent fold (F3) (Plate 2). The presence of

D3 is also supported by a weakly-developed, steeply-dipping crenulation cleavage (S3) in the Surprise Member of the Kingston Peak Formation along the axis of this open synform (Figure 9).

The youngest deformational event (D4) in the area produced brittle deformation and a series of shallow west-dipping faults within Pleasant Canyon. Where the graded gravel road reaches the floor of Pleasant Canyon (Figure 2; Plate 1), the west-dipping South Park Fault, a low-angle normal fault, separates the Crystal Spring Formation in the hanging wall from quartzofeldspathic basement in the footwall (Plate 1 and 2). Slightly east of the South Park Fault (Plate 1), a west-dipping reverse fault places mylonitic granodiorite (Kmg) over itself and the amphibolite (pCkb) within the Surprise Member of the Kingston Peak Formation (Plate 2 and Figure 10). In the ridges directly north and south of Clair Camp (Plate 1 and 2), west-dipping, low-angle normal faults displace rock units within the Surprise Member of the Kingston Peak Formation (Plate 2). The boundary between the Kingston Peak Formation and the World Beater Complex is a west-dipping, presumably normal, fault (Plate 1 and 2). The low-angle, west-dipping normal faults in Pleasant Canyon are Cenozoic in age and were responsible for exhuming the Panamint Mountains during Basin and Range extension (Hayman et al., 2003; Wernicke et al., 1988).

4. Methods

4.1 FIELD METHODS

The fieldwork in this study was conducted in three stages. The first stage was digital mapping using field traverses and assistance from a laser rangefinder for improved mapping on cliff faces. In this first stage, the two sites (Clair Camp Structure and Noonday Structure) were chosen for 3D TIN analysis. The next stage involved taking photographs of both the Clair Camp Structure and Noonday Structure for photogrammetry. The final stage was scanning Pleasant Canyon using an UNAVCO TLS.

4.1.1 Digital mapping using a laser rangefinder

Mapping metamorphic rocks and structures in Pleasant Canyon was carried out using a GPS-enabled Trimble TDS Recon Pocket PC handheld computer (Figure. 1). Strike and dip measurements were taken using a digital inclinometer with GPS capabilities (Figure. 1). *ArcPad* Version 10 field GIS software and 3D compatible shapefiles were used to collect and display the digital map data (Table 2; Figure 11). Since the focus of this research is to investigate methodologies for better visualizing metamorphic terranes, foliation and fold axial traces were mapped (in polyline shapefiles) to accentuate internal structures of the rock units. The shapefiles and mapping workflow followed the formats outlined in Pavlis et al. (2010).

For remotely mapping contacts at distances up to 1 km, the Trimble TDS Recon was interfaced with a handheld LaserCraft Contour XLRic laser rangefinder (Figure. 1). With range, azimuth, and tilt angle data from the laser rangefinder, the GPS enabled Trimble TDS Recon can accurately place offset points and polylines onto the 2D digital map from a distance and in real time. The location accuracy of offset features mapped with the laser rangefinder depends on the

accuracy of the GPS, which is about 1-5 m horizontal and 10 m vertical accuracy according to the manufacturer (GlobalSat Worldcom Group, 2009). The laser rangefinder made it possible to map the steep cliffs that make up Pleasant Canyon which would have been difficult and time consuming to traverse safely. The location accuracy of offset features mapped with the laser rangefinder is also dependent on the accuracy of the targeting sight, and the steadiness of the person holding the laser rangefinder. The final geologic map (Plate 1) is the result of digital mapping in the field as well as modification of linework in the office using *ArcMap* Version 10 and 2.5-m/pixel resolution Digital Globe satellite imagery from ArcGIS Online (Table 2).

4.1.2 Photogrammetry data collection

Digital photographs of the Clair Camp Structure in Pleasant Canyon were taken with a Canon EOS Rebel T3i DSLR (digital single-lens reflex). The camera has a resolution of 5184 x 3456 pixels (18 megapixels) and a focal length of 34-mm on a Canon zoom lens. Photographs of the Noonday Structure used a Nikon D5300 DSLR with a Nikkor fixed focal length AF-S DX 35mm/f 1.8 lens. All photographs were taken without flash and using automatic white balance. On the Canon camera, the automated camera settings used for all of the photographs taken using auto landscape include an *f*-stop of 11, exposure time of 1/200 s, and ISO of 100. On the Nikon, the photographs were taken in auto landscape with the camera adjusting both exposure time and *f*-stop. All images were stored in JPEG format. These images were used for both context in describing the Noonday and Clair Camp Structures and for use in photogrammetric reconstruction of 3D TINs of these two structures.

In order to obtain sufficient stereoscopic overlap to accurately model the outcrops, it is important to obtain images from several camera positions. The positions should be chosen such that the sum of the distances between the camera positions (baseline) is twice as large as the

distance from the camera position to the farthest feature (Wolf, 1983; Figure 3). Stereoscopic overlap can also be increased by taking several to tens of photographs of an outcrop at each camera position and changing the camera angle slightly for each photograph (Wolf, 1983).

For the Clair Camp Structure, the laser rangefinder was used in the field to capture XYZ coordinates for ground control points (marker points). These marker points were natural objects chosen *in-situ*, such as oddly shaped or distinctively colored rocks that can be readily identified in both the images and in the field. The marker points are used to specify locations within a photograph, set the coordinate system for the photographs used, and serve as fixed locations for photo alignment during processing. The more marker points used, the better the calibration (Stojakovic, 2008) and the manual for *Agisoft PhotoScan Professional* Version 1.1.1 (photogrammetry software used in this study; Table 2) recommends having at least ten marker points. Thirteen marker points for the Clair Camp Structure were collected with the laser rangefinder and stored in a 3D shapefile on the Trimble TDS Recon. However, only eight marker points were used to build a 3D point-cloud of the Clair Camp Structure (Figure 12). Reasons for using only eight marker points for the Clair Camp Structure will be discussed in section 4.2.1. Five camera positions were used in the photogrammetry field array for the Clair Camp Structure and their coordinates were obtained using the GPS (Figure 12).

For the Noonday Structure, photographs were taken from ten camera positions at too large a distance for use of the laser rangefinder (Figure 13). Since the Noonday Structure was out of range of the laser rangefinder, marker points were extracted from the TLS-derived point-cloud. The process of obtaining marker points for the Noonday Structure will be discussed further in section 4.2.1.

After field acquisition of the images and marker points, 3D point-clouds were generated from the data using the photogrammetry tools in *Agisoft PhotoScan Professional* Version 1.1.1 software (<http://agisoft.ru/products/photoscan/professional>). It was initially intended that point-clouds of the Clair Camp and Noonday Structures would be made in the field during evening work sessions on a Lenovo IdeaPad Z575 laptop with AMD A-Series 1.6 Ghz quad-core processor and 6 GB of RAM running 64-bit Windows 7. However, this procedure failed because this laptop did not have sufficient processing power to complete the point-clouds in a reasonable time. For example, modest size projects with 10-20 photographs may take 5-10 days to process on a mid-level 64-bit Windows system, and will not even run under the memory restrictions of a 32-bit Windows system. As a result, the field data had to be processed back in the lab.

4.1.3 LiDAR data collection

A Riegl LMS-Z620 TLS with a maximum range of 2 km and a field of view between 80° and 360° was used to collect point-clouds of Pleasant Canyon (Figure 14). TLS data was collected for most of Pleasant Canyon from Clair Camp to an area in the western part of the canyon just above the South Park Fault (Plate 1). Simultaneously, co-registered digital images were captured with a Nikon D700 12.1 megapixel DSLR camera that was mounted to the scanner. The photographs taken have a resolution of 4256 x 2832 pixels with variable *f*-stop and exposure and ISO of 200. The camera was equipped with a 20-mm, fixed focal length Nikkor lens. These instruments were on loan from UNAVCO.

The TLS operates at a scanning rate of 8000 points/second. The rangefinder on the scanner is accurate to 10 mm and it has a range of up to 2 km away (K. Williams of UNAVCO, personal communication). The TLS is also equipped with a differential GPS receiver that was

post-processes using Trimble Business Center, with which 3 cm horizontal positional accuracy was obtained (K. Williams of UNAVCO, personal communication).

4.2 OFFICE DATA PROCESSING

After the data was collected in the field, they were processed using desktop computers to generate 3D point-clouds. Photographs taken in the field for photogrammetry were processed by the author at The University of Texas at El Paso. The scans of Pleasant Canyon from the TLS were co-registered and georeferenced by UNAVCO using *RiSCAN Professional* Version 1.8.0 and they generated a georeferenced 3D point-cloud of Pleasant Canyon which was then transferred to the author for further adjusting (Table 2). Detailed instructions for various data processing operations can be found in Appendix 2.

4.2.1 Photogrammetry

The images collected in the field at the Clair Camp Structure and the Noonday Structure were processed using the photogrammetry tools in *Agisoft PhotoScan Professional* Version 1.1.1 software to generate 3D point-clouds for both sites (Table 2). Initial work used a dual processor, 64bit Linux system with 16 Gb of RAM. Later work on the project used a more powerful computer, a Dell Precision 7910 with two 1.6 GHz Intel Xeon E5-2603 v3 processors with 12 cores each, 15 MB cache, and 64 gigabytes of 2133 Mhz DDR4 RAM was used to build the 3D point-clouds. Using the 12 core Dell system increased processing speed by more than an order of magnitude relative to the 2 core Linux system, allowing processing of jobs with hundreds of photographs, like the Noonday Structure model, in less than 1 day of processing vs weeks that would have been required on the Linux system. In addition to the photographs, GPS coordinates of camera positions and the marker points captured with the laser rangefinder were included in

the processing. The process of generating a 3D point-cloud in *PhotoScan* is described in the following workflow.

First, the digital photographs are imported into *PhotosScan*. The software accepts any of the following formats: JPEG, TIFF, PNG, BMP, PPM, OpenEXR, and MPO. Since the photographs for this research were stored in JPEG format, they were imported without any format change. Once imported, all of the photographs appear in the *PhotosScan* workspace and each photograph can be selected and viewed for quality checking (Figure 15). Any blurry or overly oblique images are deleted before additional processing is applied. For the 3D point-cloud of the Clair Camp Structure, 19 photographs were used whereas 328 photographs were used for the Noonday Structure 328. The variation in the amount of photographs used was done to quantitatively assess the effect of increasing photograph numbers.

The next step is camera calibration. In *PhotoScan*, the user can select the brand and model of camera used and change calibration parameters. The calibration parameters include focal length, principal point coordinates, skew transformation coefficient, radial distortion coefficients, and tangential distortion coefficients. These parameters serve as a starting point for camera calibration and these parameters are refined during the sixth step which is photograph alignment (Table 3).

After camera calibration, irrelevant features such as sky, background (distant mountains in the case of this research), and unnecessary foreground (shrubs, mounds, etc. that obscure the subject of the photograph) may be masked out to improve processing speed (Figure 15). *PhotoScan* is equipped with a manual masking tool, which allows the user to either triangle select or freehand select features that requiring masking. The other option is the semi-automated magic wand tool, which requires only a single click of the mouse within the feature that the user

wants to mask. *PhotoScan* will then use RGB information from the selected pixel to select all of the surrounding pixels that have the same, or very similar, RGB values. This option works best for masking clear skies based on trial and error using *PhotoScan*. For this study, a combination of magic wand and manual masking was used. Masking irrelevant features from each photograph is not required for generating a 3D point-cloud. Moreover, it would be incredibly time consuming if the user had hundreds of photographs to mask because it would have to be done manually. However, if tens of photographs are used, taking the time to mask irrelevant features will decrease processing time and reduce the amount of point-cloud editing later in the 3D TIN building process.

After the images have been calibrated and masked, the next step is to import the GPS coordinates of the camera positions associated with each photograph. The coordinates are imported either as a CSV file or by manually typing in each coordinate into a table (Figure 15). For the Clair Camp Structure, GPS coordinates of the camera positions were entered manually in *PhotoScan*. Once the coordinates are in *PhotoScan*, the user selects all of the photographs that belong to a specific camera position and assigns them to the appropriate camera position coordinate. The Clair Camp Structure utilized five camera positions (Figure 12), while the Noonday Structure did not utilize the ten recorded camera positions for point-cloud generation due to the time constraints imposed by assigning over 300 photographs to its proper camera position (Figure 13). Note this step of entering camera positions can be eliminated by use of a GPS enabled camera. In addition, camera positions are not essential when marker points are available, but do dramatically decrease processing time for the camera alignment step in the processing workflow.

In addition to camera position coordinates, the marker points are imported in CSV format or manually entered into the marker point table (Figure 15). The use of marker points for ground control allows for more precise georeferencing than using camera positions alone. The descriptions and annotated photographs of the markers made in the field were used to locate the marker points in each of the photographs in *PhotoScan*. There is an undetermined amount of user error associated with the placement of markers in photographs that occurs when markers are not placed precisely where they should be in each photograph.

No marker points were obtained in the field for the Noonday Structure. Marker points for this model used natural objects that were recognizable on the TLS-derived point-cloud of the Noonday Structure. The positions of the marker points were extracted using *Maptek I-Site Studio* Version 5.0 software to query the point-cloud. Eight marker points were extracted from the LiDAR point-cloud for building a 3D point-cloud of the Noonday Structure (Figure 16). The number of marker points selected was determined by the number of prominent features found on the TLS-derived point-cloud that could confidently be located in the field photographs taken of the Noonday Structure. Marker points were taken from the TLS-derived point-cloud in part because the photographs were taken from beyond the range of the laser rangefinder, but also to determine if markers obtained from the TLS-derived point-cloud serve as better ground control than markers collected in the field. When hundreds of photographs are being used to generate a 3D point-cloud, as is the case of the Noonday Structure, guided marker placement is suggested because it speeds up marker placement and reduces the chance of incorrect marker placement (Agisoft PhotoScan User Manual). In guided marker placement, all markers are located on at least one photograph, and then *PhotoScan* locates the markers in the rest of the photographs

automatically. If the guided placement approach is used, the user can also manually refine the marker point locations if necessary, which was done in this case.

The next step of processing is photograph alignment where *PhotoScan* locates the camera position and the orientation for each photograph and generates a sparse point-cloud model. Note that in guided marker replacement, the camera alignment step and construction of a mesh from the sparse point cloud is required prior to marker placement. In the camera alignment step, the software detects features and matches these features in all of the photographs. For photograph alignment the software prompts the user to select the type of pair preselection and the accuracy. Pair preselection speeds up the alignment process by selecting a subset of image pairs to be matched instead of matching features across all of the photographs at once. For both the Clair Camp and the Noonday Structures, pair preselection was based on ground control, which means the overlapping pairs of photographs are selected based on the measured camera positions and the marker points. Accuracy refers to the accuracy of camera positions and the user may select high or low accuracy where higher accuracy will require more processing time for alignment and the low accuracy will result in a rough estimate of the camera positions and take less processing time. For both the Clair Camp and the Noonday Structures, accuracy was set to high. The time it takes to complete the alignment process also depends on the number of photographs used.

After alignment, *PhotoScan* calculates the X-,Y-, and Z-error of each camera position and marker point. The XYZ errors are distance errors and represent the distance in the X, Y, and Z directions from the source position (the coordinate position entered into the *PhotoScan* by the user) to its calculated position in the model after alignment. The total error is the average of the XYZ errors for every camera position or marker point. For the Clair Camp Structure, the total error for the camera positions was 29.5 m and the total error for the marker points was 22.5 m.

For the Noonday Structure, the total error for the marker points was 281.6 m. The total error for the camera positions for the Noonday Structure was not obtained since camera positions were not entered for this structure. For the Clair Camp Structure, marker points that could not be confidently located in any of the photographs or had a positional error >100 m after alignment were removed and the photographs were realigned. Five marker points from the Clair Camp Structure fell into one of these two categories leaving eight marker points to be used to build a 3D point-cloud.

The final step is to build a dense point-cloud using the positions of the camera and the program calculates depth information for each photograph taken to be combined into a dense point-cloud (Figure 17). Building a dense point-cloud requires the user to choose the desired quality of the dense point-cloud. The higher the quality setting, the more detailed the resulting point-cloud by reducing point spacing and increasing point density (Table 4). Higher quality will also result in a more geometrically accurate point-cloud. However, higher quality also means more processing time, and, depending on the number of photographs a high-quality point-cloud can take days to generate even with the Dell Precision 7910 workstation. The dense point-clouds for Clair Camp were made using the ultra-high setting, while the Noonday Structures were generated using the high setting (Figure 17). The lower quality setting selected for the Noonday Structure was chosen to reduce processing time. For the Clair Camp Structure, five days of processing were required to generate a point-cloud from 19 images using the Linux system. On the other hand, only two days of processing were required to generate a point-cloud of the Noonday Structure from 328 images using the Dell Precision 7910 workstation.

4.2.2 Point-cloud processing

Both the photogrammetrically- and TLS-generated 3D point-clouds were imported into *Maptek I-Site Studio* Version 5.0 to produce TINs (Table 2). The point-clouds generated from *PhotoScan* were imported into *I-Site* as ASCII text files. Because the TLS point-cloud consists of Pleasant Canyon as a whole, the point-cloud had to be separated into more reasonably-sized tiles (< 0.5 GB) before being loaded into *I-Site* where point-clouds for the Clair Camp and Noonday Structures were produced. Dividing the TLS point-cloud into smaller tiles was accomplished using *RiSCAN Pro* Version 1.8.0 (Table 2). Fifty-four individual 500 m x 500 m tiles of Pleasant Canyon were produced and exported as ASCII text files. The optimal size of the tiles was determined through trial and error. I started with 2,000 m x 2,000 m tiles and subsequently reduced the size of the tiles by 500 m until the tiles were small enough to load in *I-Site* within a few minutes.

After importing the point-clouds to *I-Site*, they were quality checked. Any stray points (points that are more than 2 m from the next closest point) should be deleted before generating a TIN. Stray points are commonly caused by the presence of sky in the photographs used for photogrammetry or dust particles from TLS data. For the photogrammetry data, there were between tens of thousands to over 3 million stray points removed (Table 4). For the TLS data, tens of millions of stray points were removed (Table 4). The process of removing stray points from a point-cloud is referred to as “clean-up”. Clean-up can be done by scanning the point-cloud for points that seem to float above or below the point-cloud and manually selecting and deleting them. Another way to clean-up a point-cloud is to apply a distance filter. To perform distance filtering, the user sets a maximum range that a point can be from any other point. Any

points located beyond this maximum range are deleted. In order to maintain as many points as possible, stray points were deleted manually for this study.

After eliminating stray points, a TIN is made in *I-Site* using topographic or spherical triangulation. In topographic triangulation, *I-Site* builds triangular facets between points by assuming a map-view origin. This mode of triangulation will generate vectors between points in a downward direction along the Z axis. This means that in a cluster of points *I-Site* will find the point with the highest Z values and will draw vectors from this point to the points with the next highest Z values. This is why it is important to remove stray points because topographic triangulation will produce erroneous spikes in the surface that will require more processing time to remove in order to produce a TIN that is an accurate representation of the surface.

The TINs of the Clair Camp Structure derived from both the TLS and the photogrammetry data were made prior to obtaining the Dell Precision 7910 and thus required extra processing. The Clair Camp Structure point-clouds were processed on a Dell Precision T5500 with two 2.4 GHz Intel E5620 processors (each with four cores, for a total of 8) and 12 GB of RAM. This computer was not as capable at handling the dense point-clouds as the Dell Precision 7910, meaning that loading, manipulating, and processing the point-clouds was more time-intensive on this machine. The main challenge in processing and analyzing TLS- and photogrammetrically-derived point-clouds using the Dell Precision T5500 is minimizing the file size, and thus processing time, without compromising the desired resolution. In order to process the point-clouds without overloading the CPU of the Dell Precision T5500, the density of the Clair Camp Structure point-clouds had to be decreased. The point-cloud files for the Noonday Structure derived from photogrammetry and the TLS data did not require a filter because the Dell Precision 7910 was able to handle the tens of millions of points (Table 4). Due to time

constraints and for the purpose of this study, it was not necessary to reprocess the Clair Camp Structure point-clouds using the Dell Precision 7910.

To decrease the number of points, and thus the file size and processing time, it was necessary to apply a topographic filter to both the photogrammetry- and the TLS-derived point-clouds of the Clair Camp Structure. A topographic filter removes points based on their elevation relative to the lowest point within a user-defined cell. For outcrops with vegetation cover, keeping the lowest point in the cell will best represent the true rock surface because the filter will have the effect of removing the vegetation (McCaffrey et al., 2008). A cell size of 0.45-m was chosen after experimenting with different sizes and seeing their effects on resolution and the time required to generate a TIN after filtering. Using the 0.45-m cell size in the filter produced a point-cloud where the minimum distance between nodes was 0.45 m. Filtering decreased the point count of each point-cloud by an order of magnitude (Table 4), which in turn decreased the time required to generate a TIN from hours to minutes using the Dell Precision T5500.

Finally, in order to make interpretations on the TLS-generated TINs, field photographs were draped onto the TINs to better visualize the different rock units. For the Clair Camp Structure, only one photograph drape was required because the chosen photograph completely covered the structure, whereas the Noonday Structure required two photos to cover most of the structure. Draping photographs onto the photogrammetrically-derived TINs was not necessary since the point clouds derived from photogrammetry utilize high-resolution photographs that are fully integrated with the underlying 3D surface (Haneberg, 2008). Draping a photograph onto a TIN in *I-Site* involves importing the desired image and co-registering it to the TIN using at least eight control points (Figure 18). Once the points are set, the user can display projection vectors that, ideally, extend from each of the control points and converge on a single point in space

that represents the camera position. If the vectors do not converge, then the points need to be corrected, more points need to be selected, or both in order for the photograph to be draped onto the surface in the proper position (Figure 18).

4.2.3 3D interpretations on terrain models using *Maptek I-Site*

Once photographs were draped onto the TLS-derived TINs and photogrammetrically-derived TINs the resultant terrain models were interpreted to develop a 3D geologic model. In *I-Site*, polylines can be drawn directly on the terrain model to trace lithologic contacts, faults, foliations, etc. In *I-Site* vertices will snap to the surface, but the line segments between vertices will not, which leads to a visualization artifact where line segments can float above the terrain model, pass beneath it, or both. This effect can be eliminated by projecting the interpreted polyline to the TIN elevation surface. However, *I-Site* only projects in the Z-direction, so if interpretations are made on steep cliff faces, the resulting projection will produce significant errors (Figure 19). Interpretations made on both the Clair Camp and Noonday Structure terrain models were, therefore, not projected to the TIN elevation surface because both contain steep cliff faces. Instead, to minimize the effect of floating line segments, the length of line segments was reduced by selecting many vertices when making interpretations (Figure 20, 21, 22 and 23; Animation 1, 2, 3 and 4; Appendix 1).

Strike and dip measurements were also determined from the TLS-derived terrain models using the Geotechnical Module in *I-Site*. The process involves selecting a minimum of three points that represent the same plane, as in a traditional three-point problem, and computing the orientation of that plane in geographic space using trigonometry. In a steep canyon, it is imperative to quality check the resulting strike and dip using the 3D visualization tools in *I-Site*. Common problems are when the selected points describe the orientation of the erosional façade

of a cliff and not of a geologically-relevant plane such as bedding. Thirty strike and dip measurements of interpreted foliation planes and lithologic boundaries were obtained with this method for both the Clair Camp and Noonday Structure terrain models.

The benefit of 3D terrain models for geologic mapping is that they allow the interpreter to make more detailed interpretations and obtain strike and dip data in inaccessible areas. For example, geologic interpretations can be made and orientation data can be collected on hard to reach cliffs, such those in the Noonday Structure, that would be both dangerous and time-consuming to visit in the field.

The final 3D geologic interpretations made on the terrain models were exported from *I-Site* in DXF format and imported into Midland Valley's *MOVE* Version 2014.2 where they could be evaluated against interpretations made in the field using digital mapping techniques (Table 2). Orientation data obtained from the TLS-derived terrain models of the Clair Camp and Noonday Structures were also exported from *I-Site* in DXF format and imported into *MOVE* where they could be plotted on stereonets and evaluated against field orientation data. The workflows used to make TINs derived from both photogrammetry and TLS data are summarized in Figures 24 and 25 and detailed description of the workflow is documented in Appendix 2.

5. Results

The photogrammetrically-derived TINs from both the Clair Camp and the Noonday Structures were directly compared to the corresponding TLS-derived TINs in order to determine the spatial accuracy of the photogrammetrically-derived TINs. In addition, geologic interpretations made on the terrain models of both the Clair Camp and the Noonday Structures were compared to their corresponding interpretations made in the field. The TLS-derived terrain models from both the Clair Camp and the Noonday Structures were also used to obtain orientations of lithologic boundaries and foliation traces and these orientations were plotted on a stereonet and compared to the orientations taken from the field.

5.1 COMPARISON OF 3D TERRAIN MODELS

The TIN generated from photogrammetry was quantitatively compared to the LiDAR TIN to evaluate the spatial accuracy of TINs derived from photogrammetry. In this analysis, the TLS-derived TIN was used as the reference surface due to its high resolution and centimeter-scale equipment precision. A visual comparison in *I-Site* shows that the photogrammetrically-derived TIN of the Clair Camp Structure does not align with the TLS-derived TIN of the same structure and is instead situated beneath it (Figure 26 and Animation 5; Appendix 1). The horizontal extent of the photogrammetrically-derived TIN of the Clair Camp Structure is also smaller than the TLS-derived TIN and stretching of the photogrammetrically-derived TIN would be required in order to better represent the structure.

A photogrammetrically-derived TIN of the Clair Camp Structure that was generated in *PhotoScan* without marker points was also made to evaluate how the use of marker points improves the accuracy of photogrammetrically-derived TINs. Animation 5 (Appendix 1) shows

that the photogrammetrically-derived TIN of the Clair Camp Structure without markers is displaced well above the TLS-derived TIN and is also tilted at an angle relative to the TLS-derived TIN. This result is not surprising and undoubtedly results from the lack of marker points. This result illustrates that TINs generated without reference markers should be used with caution in any analysis that involves absolute positioning and orientation.

A surface analysis tool in *I-Site* was used to compare the two TINs in an attempt to quantify the offset of the photogrammetrically-derived TINs from the TLS-derived TINs. However, the results of using the surface analysis tool were inconclusive since the tool only estimates offset in the Z-direction as opposed to measuring absolute change (Figure 27).

In order to obtain the total vector offset in the X-, Y-, and Z-directions, a MATLAB code (Appendix 3) was written. To calculate the total vector offset between TINs, ten points were chosen and their coordinates were obtained from the photogrammetrically-derived TINs. The same ten points were then located on the TLS-derived TINs. The MATLAB script calculates the Euclidian distance in between the photogrammetrically-derived point and its TLS counterpart. This analysis shows that the 3D position of the photogrammetrically-derived TIN of the Clair Camp Structure is offset from the TLS-derived TIN by 12 m to 200 m, with an average offset of 64 m (Table 5; Figure 28).

To evaluate the use of marker points to improve the 3D position of photogrammetrically-derived TINs, the MATLAB code was used to compare the photogrammetrically-derived TIN of the Clair Camp Structure that did not utilize marker points (referred to as the “marker-less” Clair Camp TIN) to the TLS-derived TIN of the Clair Camp Structure. The marker-less Clair Camp TIN was generated using the same photographs, camera positions, and parameters used in generating the photogrammetrically-derived Clair Camp TIN that utilized marker points,

ensuring that the only variable was the presence/absence of marker points. The marker-less Clair Camp TIN is offset from the TLS-derived TIN by between 132 m and 252 m with average offset of 186 m (Table 5; Figure 29). Although use of markers reduces the average spatial error, it is still offset from the TLS-derived TIN by a significant amount. In both analyses, the point sets with the least offset were closer to the origin (camera position for photogrammetry) and offset increased with increasing distance from the origin (Figure 28 and 29).

The photogrammetrically-derived TIN of the Noonday Structure was compared to the TLS-derived TIN of the Noonday Structure using the MATLAB script and ten-point process used to calculate 3D offset of the Clair Camp Structure TINs. This analysis yielded a range of offsets between the photogrammetrically-derived TIN and the TLS-derived TIN of the Noonday Structure of 2-45 m with an average offset of 22 m (Figure 30).

5.2 3D INTERPRETATION COMPARISON ON 2D MAP

Geologic interpretations made using the terrain models generated from both TLS and photogrammetry data were each qualitatively compared to interpretations made in the field. These comparisons focused on observing any differences in the linework drawn from the same lithologic contacts visible on the different terrain models. At the Clair Camp Structure, the TLS-derived terrain model with a 5184 x 3456 pixels (18 megapixels) photograph draped on it made it easy to identify lithologic and fault contacts. For the photogrammetrically-derived terrain model it was not necessary to drape photographs because lithologic contacts and faults could be seen by activating the point-cloud (with 0.45 m minimum point spacing) in *I-Site*. The linework interpretations from the TLS-derived terrain model and the linework interpretations from the photogrammetrically-derived terrain model of the Clair Camp Structure follow the trend of the interpretations made in the field near the canyon floor, but deviate as the interpretations approach

the ridge when viewed in 2D map view (Figure 31). The maximum amount of deviation of terrain model- and photogrammetrically-derived 3D interpretations from the field interpretations of the Clair Camp Structure is ~ 45 m.

The Noonday Structure is a complex refolded fold based on the 2D map (Plate 1) and cross-sections (Plate 2). The contact at the base of the Noonday Dolomite is conspicuous on all imagery and allows a clear assessment of mapping accuracy using different approaches. The TLS- and photogrammetrically-derived terrain models of the Noonday Structure were first registered, thus removing model mismatch, and interpretations were made on both models for comparison. Interpretations made in the field using 2D orthophoto map approaches and those made on a pre-registered photogrammetrically-derived terrain model of the Noonday Structure were also compared (Figure 32). Registration was done with the registration tool in *I-Site*, using the TLS-derived point-cloud as the reference. It was possible to register the photogrammetrically-derived Noonday Structure point-cloud to the TLS-derived point-cloud because of the positional accuracy of the photogrammetrically-derived point-cloud (Figure 32). It is possible to make interpretations on the registered terrain model that are even more accurate and detailed than interpretations made from the TLS-derived terrain model (Animation 3 and 4). This level of detail could not be achieved using 2D mapping techniques, digital or otherwise. Since these detailed 3D interpretations are digital, they can be transferred to various other software programs, such as *MOVE*, for further analysis (i.e. Figures 33 and 34).

In map view, the photogrammetrically- and TLS-derived interpretations, made using *MOVE*, of the base of the Noonday Dolomite are very similar to each other and the field interpretations, which is not surprising given that all are a horizontal plane representation of the 3D line traces. The exception is on the east side of the structure where the interpretations made

from the TLS-derived terrain model deviate to the west from the interpretations made in the field (Figure 33). In cross-section view, however, the photogrammetrically- and TLS-derived interpretations are similar to each other, but the field interpretations have a unique character (Figure 34). The reason that the field interpretations are different from the terrain model-derived interpretations is because these interpretations were made in an area of the Noonday Structure with steep terrain. Where the terrain is steep, more detailed interpretations can be made on terrain models than 2D maps because map view will naturally obscure features found within cliff faces. Animation 4 (Appendix 1) shows an interpretation of part of the west wall of the Noonday Structure where one can see interpretations made on the steep terrain. Animation 4 (Appendix 1) also shows both F2 and F3 fold axes as well as internal parasitic folds. These detailed interpretations of D1, D2, and D3 structures would not be possible using 2D map approaches because these interpretations are found on a steep cliff face.

5.3 STEREONET COMPARISON

Stereonets were made in *I-Site* for S1 strike and dip orientations extracted from the TLS-derived terrain models of both the Noonday Structure and the Clair Camp Structure. These orientations were compared to measurements taken in the field (Figure 35 and 36). The stereonet of 30 TLS-derived terrain model orientations from the Clair Camp Structure is similar to that of the 51 orientations taken in the field (Figure 35). Both stereonets show (1) dominantly west dipping foliation that scatters from shallow to steep dips as a result of the fold in foliation and (2) a π -pole in the southwest quadrant reflecting the axis of the fold. The mean principal pole for the orientations obtained from the TLS-derived terrain model plunges 65° toward 075° , whereas the mean principal pole from the field orientations plunges 40° toward 090° . The stereonet of terrain model-derived orientations from the Clair Camp Structure is more scattered along a great girdle

than the orientations from the field, providing a clearer definition of the fold orientation for this structure.

The 31 TLS-derived terrain model S1 strike and dip orientations from the Noonday Structure were plotted on a stereonet and show a scatter that is significantly different than the stereonet of the 27 orientations recorded from the Noonday Structure in the field (Figure 36). Not only do the TLS-derived measurements deviate significantly from the field data but the resultant best fit great circle and corresponding π -pole suggest very different fold geometries (fold axis trending NNW from the field data vs SW for the TLS-derived orientations). In this case, independent measurements of small scale folds and fabrics through the area demonstrate that the field data give the proper fold orientation, raising questions on the source of errors in the terrain model analysis. However, the terrain model of the Noonday Structure allowed for strike/dip measurements to be obtained from areas that were unreachable in the field. The mean principal pole from the field orientations from the Noonday Structure is similar to the mean principal pole of the terrain model-derived orientations. The field orientations plunge 75° toward 090 while the terrain model-derived orientations show a mean principal pole that plunges 75° toward 080 .

The terrain model-derived orientations were combined to make a stereonet of all 61 orientations from Pleasant Canyon (Figure 37). Comparing the terrain model-derived orientations to the 210 orientations collected in the field shows similar mean principal poles (Figure 37). The mean principal pole for the field data is plunges 55° toward 090 , while the mean principal pole for the terrain model-derived orientations plunges 65° toward 075 (Figure 37). The π -pole for the terrain model-derived orientations (plunging 30° toward 235) deviates significantly from the π -pole of the field orientations (plunging 5° toward 180) and may reflect

measurement bias in the field and attempting to obtain measurements on cliff faces from the terrain models.

6. Discussion

6.1 STRUCTURAL HISTORY OF PLEASANT CANYON

Using the field interpretations and their resulting cross-sections, four deformational events were distinguished, starting with an LS-tectonite fabric (D1) with top to the north sense of shear and an associated S1 foliation that is axial planar to mesoscopic isoclinal folds (F1). The next deformational event (D2) formed shallowly-plunging and shallowly-inclined west-vergent folds (F2) in S1=S0 foliation. This event may be related to Cretaceous plutonism (Andrew, 2000). The third deformational event (D3) is east-vergent deformation which refolded west-vergent folds and formed an S3 crenulation cleavage. Both D2 and D3 were most likely associated with the Laramide Orogeny due to their relative age and the inference that they affect Cretaceous age plutons (Andrew, 2000; Parsons, 1995). These two Mesozoic events (D2 and D3) suggest an interpretation that differs from that of Andrew (2000). Andrew (2000) interpreted an east-vergent deformation that was refolded by west-vergent deformation. However, this research shows that the earliest deformation was associated with a top-north motion of unknown origin followed by a west-vergent deformation and an even younger east-vergent deformation. The final deformational event (D4) observed in Pleasant Canyon produced Cenozoic-aged, west-dipping faults associated with Basin and Range extension (Wernicke et al., 1988).

6.2 SOURCES OF ERROR FOR PHOTOGRAMMETRICALLY-DERIVED TINs

The average offset between the photogrammetrically-derived TIN and the TLS-derived TIN of the Noonday Structure is ~40 m less than the amount of offset between the photogrammetrically-derived TIN and TLS-derived TIN of the Clair Camp Structure. In addition to the relatively low offset values for the Noonday Structure in comparison to the Clair Camp

Structure, the photogrammetrically-derived TIN of the Noonday Structure does not appear to require stretching in order to match the geometry of the TLS-derived TIN of the same structure. However, the photogrammetrically-derived TINs of both the Clair Camp and the Noonday Structures were significantly offset from the TLS-derived TINs of these structures. I suggest here that there are three key sources of error contributing the spatial offset between the photogrammetrically-derived TINs and the TLS-derived TINs.

6.2.1 Geometry of the photogrammetric array in the field

The primary source of error in constructing photogrammetrically-derived TINs is the geometry of the photogrammetric array in the field. The main consideration when setting up the photogrammetric array is knowing the ratio of the baseline length (length of the line that connects the two farthest camera positions) to the distance from the baseline to the farthest feature in the scene, which is measured perpendicular to the baseline (Figure 3). In photogrammetry, depth calculations are more accurate when the baseline-to-distance ratio is 2:1 (Knötzl and Reiterer, 2010). The baseline at the Clair Camp Structure is ~360 m long and the distance from the baseline to the farthest object is ~1,020 m yielding a baseline-to-distance ratio of ~0.35 (Figure 38). At the Noonday Structure, the baseline is ~1,140 m long and the distance to the farthest object is ~1,020 m, yielding a baseline-to-distance ratio of ~1.12 (Figure 39). Neither the Clair Camp Structure nor the Noonday Structure photogrammetric array geometry has a baseline-to-distance ratio of 2:1 for the most distant features. The photogrammetric array for the Noonday Structure has a baseline-to-distance ratio that is slightly greater than 1:1 for the farthest object whereas the baseline-to-distance ratio for the Clair Camp Structure is less than 1:1. The difference in baseline-to-distance ratios may explain why the photogrammetrically-derived TIN of the Noonday Structure is more spatially accurate than the photogrammetrically-derived TIN

of the Clair Camp Structure relative to their TLS-derived counterparts. The baseline-to-distance ratio also explains why the amount of offset increases the further an object is from the camera positions or baseline. The objects that are closer to the baseline will have a greater baseline-to-distance ratio than objects that are further away from the baseline. The baseline-to-distance ratio also has implications for the stereo coverage of an area. The closer the baseline-to-distance ratio is to 2:1, the greater the stereo coverage (Wolf and Dewitt, 2000).

In addition to the baseline-to-distance ratio, the arrangement of marker points influences the spatial accuracy of photogrammetrically-derived models (Wolf, 1983). Marker points should be fairly widely spaced and evenly distributed throughout the scene being modeled (Wolf, 1983). For the Clair Camp Structure, marker points were generally located in the middle of the scene, and marker points were not collected beyond the range of the laser rangefinder. This means that features outside of the range of the laser rangefinder (1000 m), and outside the distribution of marker points in general, were not well constrained spatially. This poor distribution of marker points and lack of marker points beyond the range of the laser rangefinder may have contributed to the larger offset between the photogrammetrically-derived TIN and the TLS-derived TIN of features that are further from the camera positions and outside the range of the laser rangefinder for the Clair Camp Structure. For the Noonday Structure, the marker points were evenly distributed across the scene in an east-west direction (Figure 16). However, these marker points are generally located near the floor of Pleasant Canyon meaning features located at higher elevations are poorly constrained spatially. This distribution of marker points for the Noonday Structure may have contributed the fact that the offset in the photogrammetrically-derived TIN of the Noonday Structure is more offset between the photogrammetrically-derived TIN and the

TLS-derived TIN around the higher elevations and less offset in features near the floor of Pleasant Canyon.

6.2.2 Model error in *PhotoScan*

The second factor is the error associated with point-cloud generation in *PhotoScan*. Once all of the data (photographs, GPS coordinates of camera positions, GPS coordinates of marker points, etc.) are entered in *PhotoScan*, the program uses algorithms to generate a 3D point-cloud model of the scene captured in the photographs. This process has an associated error produced by the difference between the information that was put into the system and the information that was calculated. For the Clair Camp Structure, the total error for the camera positions was 29.5 m and the total error for the marker points was 22.5 m. The Noonday Structure did not utilize camera positions, but the total error for the marker points was 281.6 m. The amount of overlap in photographs contributes to this error (Agisoft PhotoScan User Manual). Using more photographs to build the point-cloud in *PhotoScan* increases the resolution and through greater numbers of pixels for comparison in the processing. The photogrammetrically-derived TIN of the Noonday structure utilized ten times more photographs than the photogrammetrically-derived TIN of the Clair Camp Structure, which may have contributed to the increased accuracy of the photogrammetrically-derived TIN of the Noonday Structure.

6.2.3 GPS accuracy of marker points and camera positions

The third factor contributes to the georeferencing accuracy of the photogrammetry model and it is the accuracy of marker point and camera position coordinates. For the photogrammetrically-derived TIN of the Noonday Structure, no camera positions were utilized. However, marker points used to generate the photogrammetrically-derived point-cloud of the

Noonday Structure were obtained directly from the TLS-derived TIN. The coordinates of eight marker points found on the TLS-derived TIN of the Noonday Structure were entered in *PhotoScan*, and these marker points were located in each photograph of the Noonday Structure using *PhotoScan*'s guided placement option. Aligning the photographs of the Noonday Structure using known positions derived from the TLS-derived TIN would naturally yield a photogrammetrically-derived TIN that is spatially close to the TLS-derived TIN. However, guided placement of markers should still be quality checked in each photograph to make sure the markers were placed correctly in each photograph. The total error associated with marker point placement for the Noonday Structure was 281 m, primarily because of one poorly placed marker that went unnoticed until further along in the processing. The marker point and camera position accuracy of the photogrammetrically-derived TIN of the Clair Camp Structure, on the other hand, is subject to 1 to 5 m GPS horizontal error, 10 m vertical GPS error, as well as unquantified error associated with shaking while using the laser rangefinder to collect coordinates for marker points and the manual placement of marker points on the photographs used in *PhotoScan*.

6.2.4 Other potential sources of error

Another source of error that was thought to have contributed to the error associated with the location of marker points in the field was the accuracy of the sight attached to the laser rangefinder. To test this, a target was placed at intervals of 10, 50, and 100 m away from the laser rangefinder. The target chosen for this test needed to be large enough for the user to see at 100 m away, but small enough to constrain the precision of the sight. The target chosen was 10 cm in diameter. The three horizontal intervals chosen were measured out and the user looked through the sight and attempted to hit the target with the laser pulse (Table 6). If the user hit the

target, the horizontal distance measured by the laser rangefinder would equal the horizontal distance measured on the ground for that interval. The user successfully hit the target at all intervals, so the accuracy of locating features through the sight was determined to be the 10 cm diameter, which are easily located at 100 m. This test yields a maximum angular error of $5.7 \times 10^{-2}^\circ$ and is considered a very minor contributor to the overall offset of photogrammetrically-derived TINs.

6.3 SOURCES OF ERROR IN 3D INTERPRETATIONS

Deviation in the TLS-derived terrain model interpretations from the field interpretations of the Clair Camp Structure may be the result of stretching in the draped photograph (Animation 2; Appendix 1). Deviation in the photogrammetry interpretations from the field interpretations of the Clair Camp Structure is dominantly the result of the offset of photogrammetrically-derived TIN. Interpretations made on the TLS-derived terrain model of the Noonday Structure were deviated to the west, which is most likely due to the fact that the interpretations were made using a photograph draped onto the TIN of the Noonday Structure. The look direction of the photograph is toward the east and so the edges of the photograph are stretched in that direction instead of properly wrapping around the structure to the north (Animation 4; Appendix 1). However, where the photograph drape is accurate on the TLS-derived TINs of the Clair Camp Structure and the Noonday Structure, the linework is also accurately placed. This observation indicates that a photographic interpretation is only as good as the accuracy of the georeferencing of the photograph to the earth model.

6.4 DISCREPANCIES IN THE ORIENTATION COMPARISON

The clearer definition of fold orientation in the terrain model-derived orientations from the Clair Camp Structure is probably due to the fact that more of the fold could be accessed using the terrain model than could be obtained on foot in the field. The source of error in the terrain model-derived orientations of the Noonday Structure is most likely the result of attempting to obtain orientations from cliff faces, which have very limited space for an accurate three-point calculation.

6.5 INSIGHTS INTO DEVELOPING PHOTOGRAMMETRIC TERRAIN MODELS FROM THIS WORK

To generate a spatially accurate terrain model derived using photogrammetry there are three main factors to consider. The first factor is the geometry of the field array, second is the selection and placement of marker points, and the third factor is the type of equipment used. The types of equipment used to collect and process data have an effect on efficiency. Implementing the recommendations discussed in this section regarding equipment, processing procedures, and collecting strike/dip measurements from terrain models can increase efficiency by minimizing the time required for collecting data and decreasing processing time. Insights regarding when to use aerial scanning or photogrammetry technology over terrestrial-based technologies (TLS or terrestrial photogrammetry) are also discussed.

6.2.1 Geometry of the field array

This study demonstrates some well-understood issues in conventional photogrammetry remain an issue in modern, structure-from-motion based software like *PhotoScan*. A site for photogrammetry should be chosen prior to going into the field. Preselecting a site for photogrammetry will ensure that proper equipment (e.g. laser rangefinder vs targets for locating

marker points) and logistical preparations are made prior to starting field work. Once a site for photogrammetry is chosen, the first step is to define the boundaries of the scene and then determine where the baseline should be located. To do this, locate on the map a feature that represents the farthest object in the scene (usually the highest point on a ridge) and measure the distance in map view from this object to an area that is logistically practical for setting up a baseline. This area should be reachable on foot for a distance that is at least twice as large as distance from the baseline to the farthest object. These measurements can easily be made in map view using a topographic map or utilities such as Google Earth, which will give a sufficient estimate of the baseline-to-distance ratio. For a more precise estimation of the baseline-to-distance ratio, elevation should be taken into account. If the baseline is higher or lower in elevation than the farthest feature in the scene, then this elevation difference should be considered and the distance from the baseline to the feature should be calculated. If a laser rangefinder is being used to obtain the coordinates of marker points instead of setting out targets, then the maximum range of the laser rangefinder should be taken into account when determining the boundaries of the scene and the geometry of the field array.

6.2.2 Selection and placement of marker points

Once the boundaries of the scene for photogrammetry have been defined, marker points need to be placed (or located if using natural objects) evenly throughout the scene within this boundary (Wolf, 1983). This means that marker points should be placed (or located) in the corners and in the center of the scene. Using targets that can be placed throughout the scene is more time consuming and limits photogrammetry to scenes that are easily accessible on foot. On the other hand, using targets will make it easier to locate the marker points in photographs during processing and thus reduce the error associated with placing marker points in photographs. Using

targets can also reduce the errors associated with the laser rangefinder since the GPS of the targets can be recorded during placement. If targets are the preferred marker type, then targets should be brightly colored flat surfaces that are large enough to be located in photographs taken from the maximum distance from the farthest feature to the baseline. To use natural objects as targets it is best to select natural objects that have flat surfaces, are not in shadow, are light colored (preferably white), and can be located easily in every photograph taken. The benefit of using digital cameras with LCD (liquid crystal display) screens is that photographs can be viewed immediately after they are taken. This means that natural markers chosen in the field can be verified to exist in all photographs immediately after the photographs are taken. Instant viewing of photographs can also allow the user to select natural markers from the photographs themselves, thus ensuring that the natural markers are easily located in each photograph, and GPS coordinates of these natural markers can be obtained right after photographs have been taken. In addition, detailed and well organized notes should be recorded for the natural object along with annotated reference photographs of the object in order to ensure that the object can be found during processing. Notes should include a detailed description of the natural object including the type of natural object (vegetation, rock, man-made structure, etc.), its shape, color, texture, and a description of the natural objects general location (e.g. a description of the natural features around the object, topographic location, etc.). A reference photograph of the natural object should be annotated by circling the object in the photograph and labeling it with a reference number. If natural objects are being used for marker points, then they must be within the range of the laser rangefinder. Using natural objects does not require traversing the scene on foot and thus reduces field-time and does not limit the type of scene modeled by

photogrammetry (meaning that steep cliffs and other unreachable terrain can be modeled using photogrammetry).

6.2.3 Equipment considerations

There are certain pieces of equipment that can speed up data collection in the field as well as processing in the office and potentially reduce spatial errors. For the field, using a GPS that is not attached to the camera generally does not introduce a very large error (approximately <0.5 m), but using a camera with GPS capabilities can eliminate this error. Using a camera with GPS capabilities will also reduce processing time in *PhotoScan* because the program will automatically obtain the GPS location of each photograph from the metadata. Allowing *PhotoScan* to automatically assigning GPS location to each photograph is much faster than importing coordinates later and manually assigning the coordinates to each photograph. A camera with GPS capabilities becomes more important when greater amounts of photographs are used to generate a point-cloud. Manually assigning GPS coordinates to hundreds of photographs can be time-intensive and tedious. If a point-cloud with a large point count is desired, then large amounts of photographs need to be taken (hundreds). In which case, a camera with GPS capabilities is recommended. Where a camera with GPS capabilities is not feasible, the coordinates of marker points and camera positions can be located more precisely using a differential GPS.

Two different computers were used in this study for point-cloud processing. This was the result of starting with a computer (Dell Precision T5500) that was thought capable of handling the processing and discovering that it was too slow for many of the data sets. Later on in the research, new computers were purchased (Dell Precision 7910) which ultimately were the ones best equipped for processing the data. The point-cloud files are large (general tens of gigabytes)

with the largest point-cloud file in this study being the photogrammetrically-derived point-cloud of the Noonday Structure, which is over 7.5 Gb. Processing large point-cloud files requires a machine that is capable of running the programs desired for generating and processing point-clouds; as well as loading, manipulating, and performing analysis on large amounts of data. It is also important that the computer has an up-to-date graphics card that is capable of viewing 3D models.

6.2.4 Recommendations for obtaining strike/dip from terrain models

To obtain strike/dip measurements from terrain models that best represent the structure care should be taken as to where strike/dips are measured. Flat cliff faces should be avoided when obtaining strike/dips because there is not enough exposed surface to obtain an accurate measurement. In order to best represent the structure, strike/dip measurements should be extracted throughout the surface to obtain an even distribution of measurements.

6.2.5 When to use aerial-based technologies over terrestrial-based technologies

Terrestrial photogrammetry and terrestrial laser scanning work best when the features being photographed or scanned are oriented perpendicular to optical axis of the camera or scanner (Figure 40). For the photogrammetrically-derived point-cloud of the Noonday Structure, the camera positions were located on the ridge directly across from the scene being photographed, so the optical axis of each camera position was perpendicular (or nearly perpendicular) to the steep ridge being photographed (Figure 40). Aerial LiDAR would not be the preferred method for features with steep cliffs like those in the Noonday Structure because features located directly beneath the cliffs would be obscured from view, which is similar to the issues observed in 2D mapping. In the case of the Clair Camp Structure, the scene being

photographed for photogrammetry was not as steep as the Noonday Structure. This means that the optical axis of the camera positions was oblique to the surface of the Clair Camp Structure (Figure 40). For features with a slope that is significantly less than 90° , it may be best to use aerial LiDAR over terrestrial tools. Future studies should be conducted to determine the minimum slope required for optimal results using terrestrial-based tools.

7. Conclusions

Supplementing 3D terrain models with field work allows the geologist to make more detailed interpretations than are possible on a 2D map. Using 3D terrain models for geologic interpretations also makes it possible to make accurate interpretations in places that are difficult to traverse in the field or areas that could not be explored due to limited field time.

Another benefit of supplementing field work with analysis of 3D surface models is that quantitative 3D information can be extracted from these models, such as orientation data. This is useful for filling in information in areas that either could not be traversed in the field or were simply not surveyed in the time allowed. By extracting strike and dip information from terrain models, these data gaps can be filled and thus give a better representation of the structure in the study area. Care needs to be taken in these approaches, however, in order to capture the information at the appropriate scale to avoid issues like inadvertent measurements of a cliff face orientation rather than the orientation of underlying geologic structures.

It is widely accepted that point-clouds generated from LiDAR are accurate geometrically and spatially (Bellian et al., 2005; Thurmond et al., 2005; Alfarhan et al., 2014). However, this technology is expensive and TLS systems can be difficult to carry to remote or rough locations. Photogrammetry is a promising alternative way to generate 3D terrain models because a digital camera and a GPS are tools regularly carried by field geologists. The only addition would be a 3.5 lbs. laser rangefinder or a requirement for additional field time to place targets for marker points.

In Pleasant Canyon we tested the limits of photogrammetry by attempting to model outcrops that are over 300 m from the camera position (long-range photogrammetry) and beyond the range of the laser rangefinder. This research shows that spatially-constrained models (those

with marker points located on the outcrop) result in 3D terrain models that are more spatially accurate than those built using camera positions alone. Nonetheless, even with marker points, the photogrammetrically-derived TINs are not as spatially accurate as the TLS-derived TINs, and the inaccuracy increases the farther away an object is from the camera positions or baseline.

The large amount of spatial error seen in the photogrammetrically-derived TINs can be minimized by increasing the length of the baseline such that it is about the twice the distance from the baseline to the farthest feature. Increasing the length of the baseline will also improve stereo coverage. Stereo coverage and point-cloud density can also be increased by using more photographs. Accurate placement and even distribution of marker points within the area of interest is also important for creating spatially accurate 3D surface models of an outcrop. The marker points for the photogrammetrically-derived TIN of the Clair Camp Structure were focused in the center of the structure and were not thoroughly spread to the edges of the structure due to the edges being out of range for the laser rangefinder. This suggestion regarding the distribution of marker points should be tested in future research.

Other sources of error can be minimized as well, such as holding the laser rangefinder more steady by using a tripod. Another source of error is placement of markers in each photo back in the lab. Annotated photographs and thorough notes should be taken in the field when choosing natural objects as marker points so that the marker point can be located accurately back in the lab and then select the guided placement option in *PhotoScan* allowing the program to automatically locate the marker points in the remaining photographs. The final source of error that can be mitigated is using sub-meter accuracy differential GPS.

Although photogrammetry may not be able to generate a spatially accurate 3D terrain model of an entire canyon wall the way LiDAR can, it can still be a useful 3D aid for making

interpretations. For example, any terrain model generated by these methods has a resolution that is 1 to 3 orders of magnitude better than terrain models from shuttle radar or other sources, thus even with significant absolute spatial errors, the relative positions for modeling geologic structure are vastly improved. Finally, because the models generated by photogrammetry and TLS are analogous, future work should emphasize methods for better georeferencing the photogrammetry models, including post-processing referencing similar to georeferencing aerial photography in GIS.

As a result of this research, workflows were established for collecting, processing, and making interpretations on 3D terrain models derived from both photogrammetry and TLS. These workflows can increase efficiency and minimize errors for future researchers using these technologies and software.

References

Agisoft, “Agisoft PhotoScan Professional edition.” Accessed: 14 December 2013.

<<http://agisoft.ru/products/photoscan/professional>>

Albee, A.L., Labotka, T.C., Lanphere, M.A., and McDowell, S.D., 1981, *Geologic map of the Telescope Peak Quadrangle, California*: U.S. Geological Survey Geologic Quadrangle Map GQ-1532, scale 1:62,500.

Alfarhan, M., White, L., Tuck, D., and Aiken, C., 2014, Laser rangefinders and ArcGIS combined with three-dimensional photorealistic modeling for mapping outcrops in the Slick Hills, Oklahoma: *Geosphere*, v. 4, n. 3, p. 576-587.

Andrew, J.E., 2002, *The Mesozoic and Tertiary tectonics of the Panamint Range and Quail Mountains, California* (Ph.D. dissertation): The University of Kansas, 387 pp, UMI n. 3053977.

Andrew, J.E. and Walker, J.D., 2009, Reconstructing late Cenozoic deformation in Central Panamint Valley, California: Evolution of slip partitioning in Walker Lane: *Geosphere*, v. 5, n. 3, p. 172-198.

Buckley, S.J., Howell, J.A., Enge, H.D., Leren, B.L.S., and Kurz, T.H., 2006. Integration of terrestrial laser scanning, digital photogrammetry and geostatistical methods for high-resolution modelling of geological outcrops, *in* The International Archives of the

Photogrammetry, Remote Sensing and Spatial Information Sciences: Dresden, Germany, Vol. XXXVI, Part B5, proceedings CD.

Buckley, S.J., Howell, J.A., Enge, H.D., and Kurz, T.H., 2008, Terrestrial laser scanning in geology: data acquisition, processing and accuracy considerations: *Journal of the Geological Society* [London], v. 165, n. 3, p. 625-638.

Burchfiel, B.C. and Stewart, J.H., 1966, "Pull-apart" origin of the central segment of Death Valley, California: *Geological Society of America Bulletin*, v. 77, p. 439-442.

Cobb, J.A. and Pavlis, T.L., 2015, *Understanding the contractional history of Surprise Canyon, California through digital field mapping, 3D modeling, and geochronology* (M.S. thesis): The University of Texas at El Paso, in press.

Dai, F. and Lu, M., 2013, Three-dimensional modeling of site elements by analytically processing image data contained in site photos: *Journal of Construction Engineering and Management*, v. 139, n. 7, p. 881-894.

Evernden, J.F. and Kistler, R.W., 1970, Chronology of emplacement of Mesozoic batholithic complexes in California and western Nevada: *U.S. Geological Survey Professional Paper* 623, p. 1-42.

GlobalSat Worldcom Group, “BC-337 User Manual version 1.1”, 2009. Accessed: 17 May 2015, <http://www.globalsat.com.tw/productspage.php?menu=2&gs_en_product_id=2&gs_en_product_cnt_id=51&img_id=416&product_cnt_folder=8>

Haneberg, W.C., 2008, Using close range terrestrial digital photogrammetry for 3-D rock slope modeling and discontinuity mapping in the United States: *Bulletin of Engineering Geology and the Environment*, v. 67, n. 4, p. 457-469.

Hayman, N.W., Knott, J.R., Cowen, D.S., Nemser, E, and Sarna-Wojcicki, A.M.S., 2003, Quaternary low-angle slip on detachment faults in Death Valley, California: *Geological Society of America Geology*, v. 31, n. 4, p. 343-346.

Hobbs, B.E., Means, W.D., and Williams, P.F., 1976, *An Outline of Structural Geology*: John Wiley & Sons (New York), 571 pp.

Hodges, K.V., Walker, J.D., and Wernicke, B.P., 1987, Footwall structural evolution of the Tucki Mountain detachment system, Death Valley region, southeastern California (Geological Society [London] Special Publication 28), p. 393-408.

Hodges, K.V., McKenna, L.W., and Harding, M.B., 1990, Structural unroofing of the central Panamint Mountains, Death Valley region, southeastern California, in (Wernicke, B.P., ed.) *Basin and Range Extensional Tectonics Near the Latitude of Las Vegas, Nevada* (Geological Society of America Memoir 176), p. 377–390.

Hoffman, P.F. and G.P., Schrag, D.P., 2002, The snowball Earth hypothesis: Testing the limits of global change: *Terra Nova*, v. 14, n. 3, p. 129-155.

Johnson, B.K., 1957, Geology of a part of the Manly Peak quadrangle, southern Panamint Range, California: *University of California Publications in Geological Sciences*, v. 30, p. 353-424.

Knötzl, C., & Reiterer, A., 2010, Evaluation of an image-assisted deformation monitoring system, in *Junior Scientist Conference 2010*, p. 43 - 44.

Kurz, T., Buckley, S., Howell, J., and Schneider, D., 2008, Geological outcrop modelling and interpretation using ground based hyperspectral and laser scanning data fusion: *Int Arch Photogramm Remote Sens*, v. 37, p. 1,229-1,234.

Labotka, T.C. and Albee, A.L., 1990, Uplift and exposure of the Panamint metamorphic complex, California, in (Wernicke, B.P., ed.) *Basin and Range Extensional Tectonics Near the Latitude of Las Vegas, Nevada* (Geological Society of America Memoir 176), p. 345-362.

Labotka, T.C., Albee, A.L., Lanphere, M.A., and McDowell, S.D., 1980, Stratigraphy, structure, and metamorphism in the central Panamint Mountains (Telescope Peak quadrangle), Death

Valley area , California : Summary: *Geological Society of America Bulletin*, v. 91, n. 3, p. 125-129.

Lanphere, M.A., Wasserburg, G.J.F., Albee, A.L., and Tilton, G.R., 1964, Redistribution of strontium and rubidium, isotopes during metamorphism, World Beater Complex, Panamint Range, California, *in* (Craig, H., Miller, S.L., and Wasserburg, G.J.F., eds.) *Isotopic and Cosmic Chemistry*: North Holland Publishing Company (Amsterdam), p. 269-320.

MacDonald, F.A., Prave, A.R., Petterson, R., Smith, E.F, Pruss, S.B., Oates, K., Waechter, F., Trotzuk, D., and Fallick, A.E., 2013, The Laurentian record of Neoproterozoic glaciation, tectonism, and eukaryotic evolution in Death Valley, California: *Geological Society of America Bulletin*, v. 125, n. 7-8, p. 1,203-1,223.

McCaffrey, K., Feely, M., Hennessy, R., and Thompson, J., 2008, Visualization of folding in marble outcrops, Connemara, western Ireland: An application of virtual outcrop technology: *Geosphere*, v. 4, p. 588-599.

McKenna, L., 1986, New Rb-Sr constraints on the age of detachment faulting in the Panamint Range, Death Valley, California: *Geological Society of America Abstracts with Programs*, v. 89, p. 33-49.

- Miller, J.M., 1985, Glacial and syntectonic sedimentation; The Upper Proterozoic Kingston Peak Formation, southern Panamint Range, eastern California: *Geological Society of America Bulletin*, v. 96, p. 1,537-1,553.
- Norton, I., 2011, Two-stage formation of Death Valley: *Geosphere*, v. 7, n. 1, p. 171-182.
- Parsons, T., 1995, Chapter 7: The Basin and range province: in *Continental Rifts: Evolution, Structure, Tectonics*, Olsen, K.H., editor, v. 25, p. 277-324.
- Pavlis, T.L., 2013, The Neoproterozoic Noonday Formation, Death Valley region, California: Discussion, by. Petterson et al., 2011: *Geological Society of America Bulletin*, v. 125, n. 1-2, p. 249-251.
- Pavlis, T.L., Langford, R., Hurtado, J.M. (Jr.), and Serpa, L., 2010, Computer-based data acquisition and visualization systems in field geology: Results from 12 years of experimentation and future potential: *Geosphere*, v. 6, p. 275-294.
- Petterson, R., Prave, A.R., Wernicke B.P., and Fallick, A.E., 2011, The Neoproterozoic Noonday Formation, Death Valley region, California: *Geological Society of America Bulletin*, v. 123, p. 1,317-1,336.

- Peucker, T.K., Fowler, R.J., Little, J.J., Mark, D.M., 1978, The triangulated irregular network: *American Society of Photogrammetry Proceedings Digital Terrain Models Symposium*, v. 516, p. 96-103.
- Ramsay, J.G. and Huber, M.I., 1983, *The Techniques of Modern Structural Geology: Applications of Continuum Mechanics in Structural Geology*: Academic Press (London), 307 pp.
- Ramsay, J.G. and Huber, M.I., 1987, *The Techniques of Modern Structural Geology Volume 2: Folds and Fractures*: Academic Press (London), 394 pp.
- Ramsay, J.G. and Lisle, R.J., 2000, *The Techniques of Modern Structural Geology Volume 3: Applications of Continuum Mechanics in Structural Geology*: Academic Press (London), 360 pp.
- Ristorcelli, S., and Schlitt, W.J., 2015, Amended technical report World Beater gold property Inyo County, California: *in Mine Development Associates Mine Engineering Services*, CMC Metals Ltd., p. 1-80.
- Sander, B., 1930, *Gefügekunde der Gesteine*: Springer-Verlag OHG (Vienna), p. 307-384.
- Stevens, C.H., Stone, P., Dunne, G.C., Greene, D.C., Walker, J.D., and Swanson, B.J., 1997, Paleozoic and Mesozoic evolution of east-central California: *International Geology Review*, v. 39, p. 788-829.

- Stewart, J.H. and Suczek, C.A., 1977, Cambrian and latest Precambrian paleogeography and tectonics in the western United States, *in* Stewart, J.H., Stevens, C.H., and Fritsche, A.E., eds., Paleozoic paleogeography of the western United States: Society of Economic Paleontologists and Mineralogists, Pacific Section, Pacific Coast Paleogeography Symposium, 1st, p. 1-17.
- Stewart, J.H., 1983, Transport of the Panamint Range structural block 80 km northwestward: *Geology*, v. 11, p. 153-157.
- Stojakovic, V., 2008, Terrestrial photogrammetry and application to modeling architectural object: *Architecture and Civil Engineering*, v. 6, n. 1, p. 113-125.
- Taylor, C.J. and Kreigman, D., 1995, Structure and motion from line segments in multiple images: *The IEEE Transactions on Pattern Analysis and Machine Intelligence*, v. 17, n. 11, p. 1,021-1,032.
- Thurmond, J., Loseth, T., Rivenaes, J., Martinsen, O., Xu, X., and Aiken C., 2005, Using outcrop data in the 21st Century – New methods and applications, with example from the Ainsa Turbidite System, Ainsa, Spain, *in* (Nilsen, T. et al., eds.) Deep-water outcrops of the world atlas: Tulsa, Oklahoma: American Association of Petroleum Geologists Special Publication CD-ROM.

Turner, F.J. and Weiss, L.E., 1963, *Structural Analysis of Metamorphic Tectonites*: McGraw Hill, Co. (New York), 545 pp.

“USGS NED n37w118 1/3 arc-second 2013 1 x1 degree DEM.” United States Geological Survey. 24 September 2014. < <http://nationalmap.gov/viewer.html>>

Wernicke, B., 1992, Cenozoic extensional tectonics of the U.S. Cordillera, in the Cordilleran Orogen: Conterminous U.S., edited by B.C. Burchfiel, P.W. Lipman, and M.L. Zoback, *Geol. Soc. Am., The Geol. of North America, G-3*, p. 553-581.

Wernicke, B.P., Axen, G.J., and Snow, J.K., 1988a, Basin and range extensional tectonics at the latitude of Las Vegas, Nevada: *Geol. Soc. America Bulletin*, v. 100, p. 1,738-1,757.

Wernicke, B.P., Walker, J.D., and Hodges, K.V., 1988b, Field guide to the northern part of the Tucki Mountain fault system, Death Valley region, California, in *This Extended Land: Geological Journeys in the Southern Basin and Range* (field trip guidebook, 1988 Geological Society of America Fall Meeting, Las Vegas, Nevada), p. 58-63.

Wolf, P.R., 1983, *Elements of Photogrammetry, With Air Photo Interpretation and Remote Sensing* (2nd edition): McGraw-Hill (Boston), 628 pp.

Wolf, P.R. and Dewitt, B.A., 2000, *Elements of Photogrammetry With Applications to GIS* (3rd edition): McGraw-Hill (Boston), 608 p.

Wright, L.A., Drake, R.E., and Troxel, B.W., 1974, Turtleback surfaces of Death Valley viewed as phenomena of extension: *Geology*, v. 2, p. 53-54.

Tables

Table 1. Strain measurements collected from stretched pebbles within the South Park Member of the Kingston Peak Formation. Section 1 represents measurements collected in the foliation plane. Section 2 represents measurements collected perpendicular to lineation. The lengths of the long and short axes of a pebble are measured and the ellipticity is calculated by dividing the length of the short axis by the length of the long axis. The reciprocal is calculated by dividing the length of the long axis by the length of the short axis. Harmonic mean is the number of measurements divided by the sum of the reciprocals and maximum ellipticity is the product of the harmonic means from each section.

Section	Long	Short	Ellipticity	Ln of Ellipticity	Reciprocol	Harmonic Mean	Max Ellipticity
1	10	2	5.00	1.61	0.20	4.74	11.14
1	21	6	3.50	1.25	0.29		
1	120	24	5.00	1.61	0.20		
1	42	9	4.67	1.54	0.21		
1	38	4	9.50	2.25	0.11		
1	27	7	3.86	1.35	0.26		

Table 1. Strain measurements collected from stretched pebbles within the South Park Member of the Kingston Peak Formation. Section 1 represents measurements collected in the foliation plane. Section 2 represents measurements collected perpendicular to lineation. The lengths of the long and short axes of a pebble are measured and the ellipticity is calculated by dividing the length of the short axis by the length of the long axis. The reciprocal is calculated by dividing the length of the short axis by the length of the long axis. Harmonic mean is the number of measurements divided by the sum of the reciprocals and maximum ellipticity is the product of the harmonic means from each section. – Continued

Section	Long	Short	Ellipticity	Ln of Ellipticity	Reciprocol	Harmonic Mean	Max Ellipticity
2	45	17	2.65	0.97	0.38	2.35	11.14
2	29	10	2.90	1.06	0.34		
2	28	16	1.75	0.56	0.57		
2	45	27	1.67	0.51	0.60		
2	38	17	2.24	0.80	0.45		
2	17	10	1.70	0.53	0.59		
2	18	7	2.57	0.94	0.39		
2	16	8	2.00	0.69	0.50		
2	32	12	2.67	0.98	0.38		
2	29	16	1.81	0.59	0.55		
2	25	17	1.47	0.39	0.68		
2	24	9	2.67	0.98	0.38		
2	20	9	2.22	0.80	0.45		
2	17	8	2.13	0.75	0.47		
2	20	9	2.22	0.80	0.45		
2	10	4	2.50	0.92	0.40		
2	14	3	4.67	1.54	0.21		
2	10	7	1.43	0.36	0.70		
2	27	7	3.86	1.35	0.26		
2	21	11	1.91	0.65	0.52		
2	17	7	2.43	0.89	0.41		
2	17	3	5.67	1.73	0.18		
2	17	2	8.50	2.14	0.12		
2	17	3	5.67	1.73	0.18		
2	18	9	2.00	0.69	0.50		

Table 2. Table of the software used in this research including the version number. The table also includes the purpose for which the software was used.

Software	Version	Purpose
ArcPad	10	2D digital mapping in the field
ArcMap	10	Editing and finalizing 2D digital map
Agisoft PhotoScan Pro	1.1.1	Generating 3D point-clouds derived from photogrammetry
RiScan Pro	1.8.0	Processing and tiling TLS data
Maptek I-Site Studio	5	TIN and 3D interpretation generation
Midland Valley 3D Move	2014.2	Cross-section and stereonet generation, and visualizing 3D interpretations

Table 3. Calibration parameters for both the Clair Camp and Noonday Structures. The initial values are the calibration parameters that *PhotoScan* calculates based on the settings entered (i.e. brand and type of camera, focal length, etc.). The adjusted values represent the parameters calculated after alignment. fx, fy = focal length in the x and y dimensions; cx,cy = principal point coordinates; skew = transformation coefficient, k1 – k4 = radial distortion coefficients; and p1, p2 = tangential coefficients.

Settings	Clair Camp Structure		Noonday Structure	
Number of Photos	19	19	328	328
focal length	34	34	35	35
pixels	5184x3456	5184x3457	6000x4000	6000x4001
Parameters	Initial	Adjusted	Initial	Adjusted
fx	7720.96	8146.17	8666.67	9157.87
fy	7720.96	8146.17	8666.67	9157.87
cx	2592	2599.52	3000	2999.93
cy	1728	1777.41	2000	2005.33
skew	0	0	0	0
k1	0	-0.0236	0	-0.1871
k2	0	0.0003	0	0.2101
k3	0	0.8761	0	0.0014
k4	0	0	0	0
p1	0	0	0	0
p2	0	0	0	0

Table 4. Table containing the number of points within the TLS- and photogrammetrically-derived point clouds of the Clair Camp and Noonday Structures. The table includes the original amount of points that each point-cloud started with prior to processing, the number of points remaining in each point-cloud after removing stray points (clean-up), and the number of points remaining in each point-cloud after applying a 0.45 m filter. No filter was applied to the photogrammetrically-derived point-cloud of the Noonday Structure as it was not necessary. This table shows that the number of points remaining after clean-up is higher for the photogrammetrically-derived point-clouds than the TLS-derived point-clouds.

Data Type	Structure	Original Point Count	Point Count After Clean-Up	After Filter (0.45 m)
TLS	Clair Camp	18875953	18872412	1226600
	Noonday	96420349	67873492	861838
Photogrammetry	Clair Camp	32165653	32100960	1110764
	Noonday	71569348	67950001	No Filter

Table 5. Table of ten offset measurements between photogrammetrically-derived TINs and TLS-derived TINs for both the Clair Camp and Noonday Structures. The table also includes offset measurements between the marker-less Clair Camp TIN and the TLS-derived Clair Camp TIN. Average offsets are included at the bottom of the table in highlighted in yellow.

Point Number	Clair Camp Structure	Marker-Less Clair Camp Structure	Noonday Structure
	Offset (m)	Offset (m)	Offset (m)
1	200.39	251.67	19.47
2	37.47	169.43	3.87
3	110.52	207.58	13.31
4	11.68	132.07	1.68
5	10.93	137.81	3.61
6	43.00	174.91	40.86
7	94.65	233.00	44.60
8	50.62	190.89	17.97
9	38.40	180.46	43.98
10	38.15	180.90	28.57
Average	63.58	185.87	21.79

Table 6. Table with measurements from the laser sight test. Measurements include range (in meters) and inclination (in degrees). For inclination of the laser rangefinder, horizontal is measured at 90° and values that are less than 90° indicates that the laser was oriented below horizontal. The user successfully hit the target at all designated intervals as the range measured is within centimeters of the actual distance.

	10 m		50 m		100 m	
	Range (m)	Inclination (deg)	Range (m)	Inclination (deg)	Range (m)	Inclination (deg)
Trial 1	10.2	88	50.3	89.7	100.3	89.8
Trial 2	10.1	89.1	50.3	89.5	100.2	89.6
Trial 3	10.2	88.6	50.1	89.5	100.1	89.7
Trial 4	10.1	88.8	49.9	89.5	100	89.6
Trial 5	10.2	88.4	50.1	89.6	100.1	89.7
Average	10.16	88.58	50.14	89.56	100.14	89.68

Figures



Figure 1. Photograph of the equipment used for digital field geologic mapping. This research utilized (1.) a GPS (Global Positioning System) receiver connected wirelessly to (2.) an Asus Tablet via Bluetooth, and (3.) A Trimble TDS Recon Pocket PC (Personal Computer) connected to (4.) a LaserCraft Contour XLRic Laser Rangfinder via a serial cable. The Trimble TDS Recon allows for a GPS (Global Positioning System) receiver to be connected to the top. A recording compass inclinometer (5.) was also used in this research.

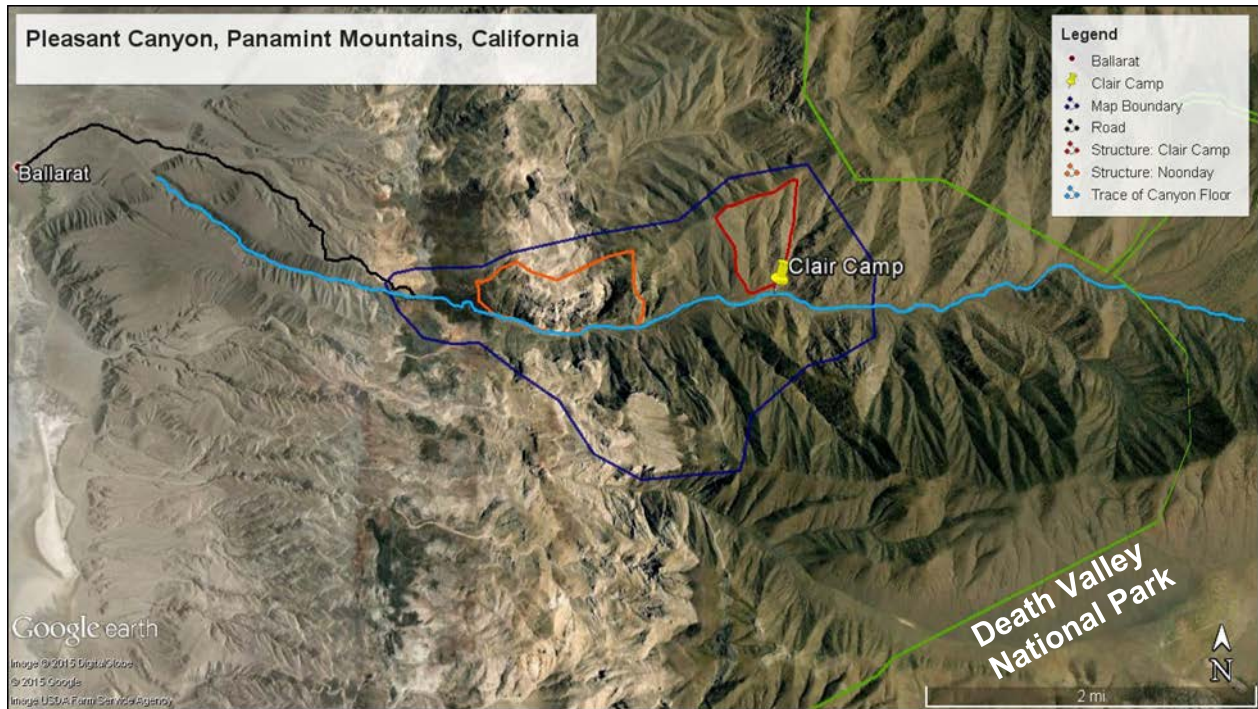


Figure 2. Map from Google Earth showing the location of Pleasant Canyon west of Death Valley National Park as represented by the green line. The locations of Ballarat and Clair Camp are labeled for reference. The black line represents the graded gravel road from Ballarat to Pleasant Canyon. The light blue line traces the floor of Pleasant Canyon. The area mapped in this study is outlined by a dark blue line. Within the mapped area are the two locations chosen for 3D surface analysis in this study. The red polygon outlines the Clair Camp Structure and the orange polygon (its southern boundary is the floor of Pleasant Canyon) represents the area modeled to make the Noonday Structure.

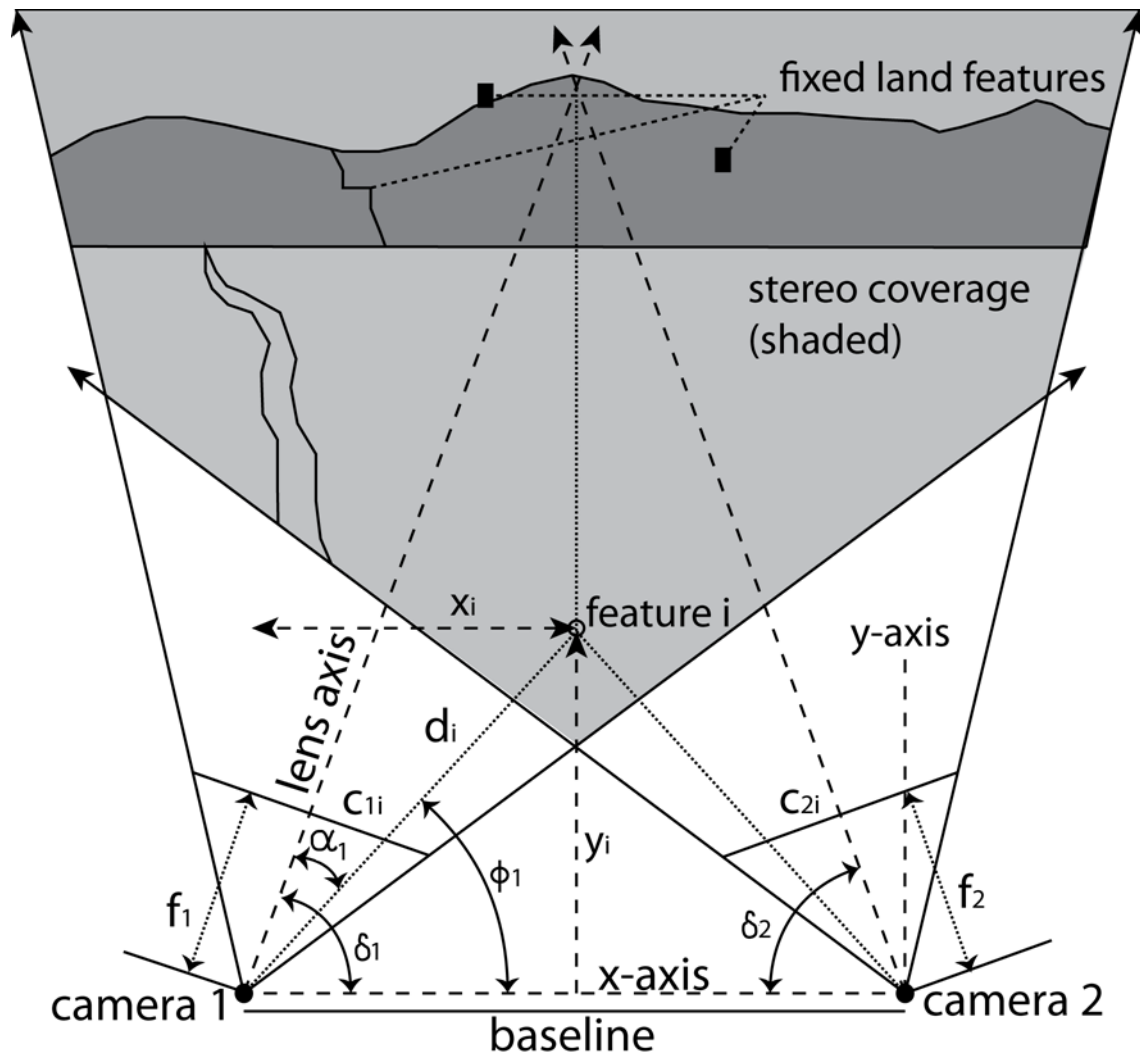


Figure 3. Diagram of the ideal setup for photogrammetry. The baseline between the two camera positions is twice as long as the distance to feature i. The shaded area represents the stereo coverage of the two cameras. Variables used to calculate the coordinates (x_i and y_i) of feature i include: focal length of the cameras (f_1 and f_2), orientation angle of the cameras (δ_1 and δ_2), position of feature i from the center of the image plane from both cameras (C_1 and C_2), ray from the camera positions to feature i (d_i), the angle between the lens axes and d_i (α_1 and α_2), and the angle between d_i and the x-axis for both camera positions (ϕ_1 and ϕ_2). Modified from Wolf, 1983.

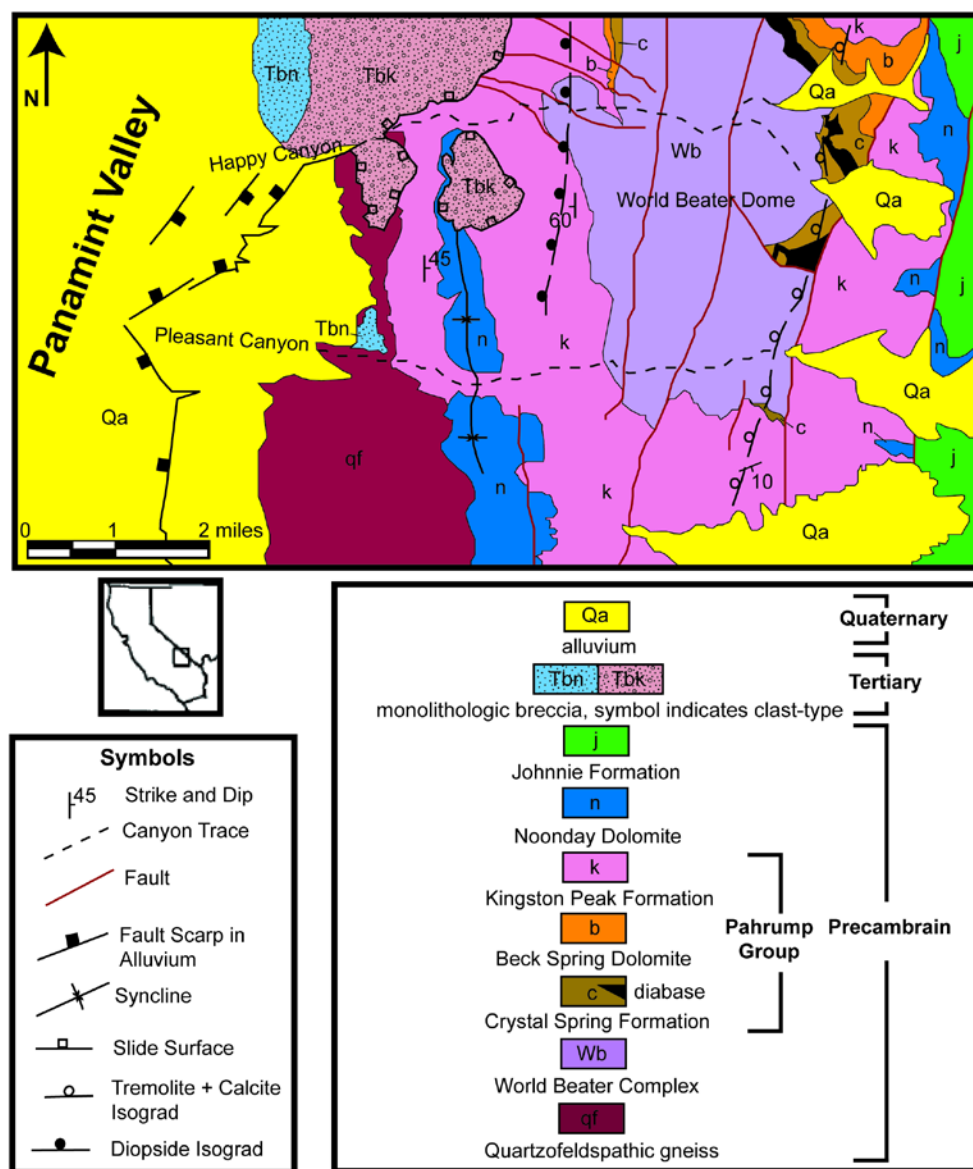


Figure 4. Geologic map of the southern Telescope Peak Quadrangle showing the location of Pleasant Canyon. Tbn = Metasedimentary clasts derived from the Kingston Peak Formation. Tbn = Sedimentary clasts derived from the Noonday Dolomite. Modified from Labotka et al. (1980).

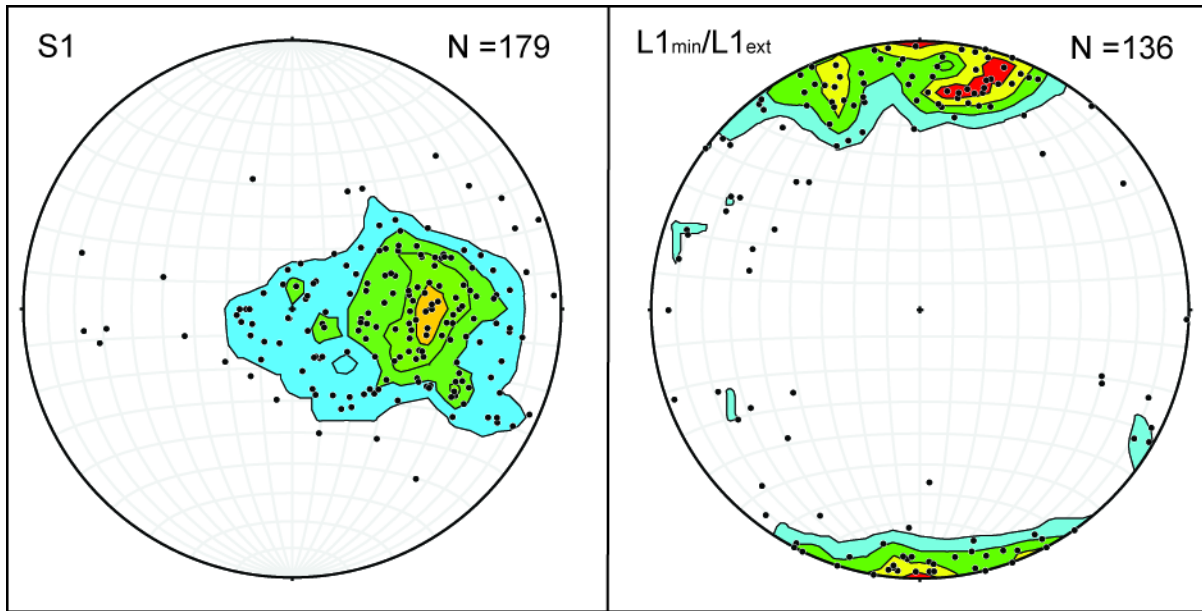


Figure 5. Stereonets of poles to planes of S1 foliation strike and dips (left), and the trend and plunge (right) of lineations ($L1_{\min}$ and $L1_{\text{ext}}$) with 1% area contour. The S1 foliation poles show dominantly west dipping structure and lineations trend north-south.

Figure 6. Flinn Diagram of the length of stretched pebbles from the South Park Member of the Kingston Peak Formation. The length of pebbles is measured in the foliation plane (X/Y) and perpendicular to lineation (Y/Z). The harmonic mean of the data plots in the LS-tectonite section within the constriction field. Refer to Table 1 for the measurements used to generate this Flinn Diagram.



Figure 7. Foliation (S1) axial planar to isoclinal folds within the Noonday Dolomite. Photograph taken on the southern wall of Pleasant Canyon.

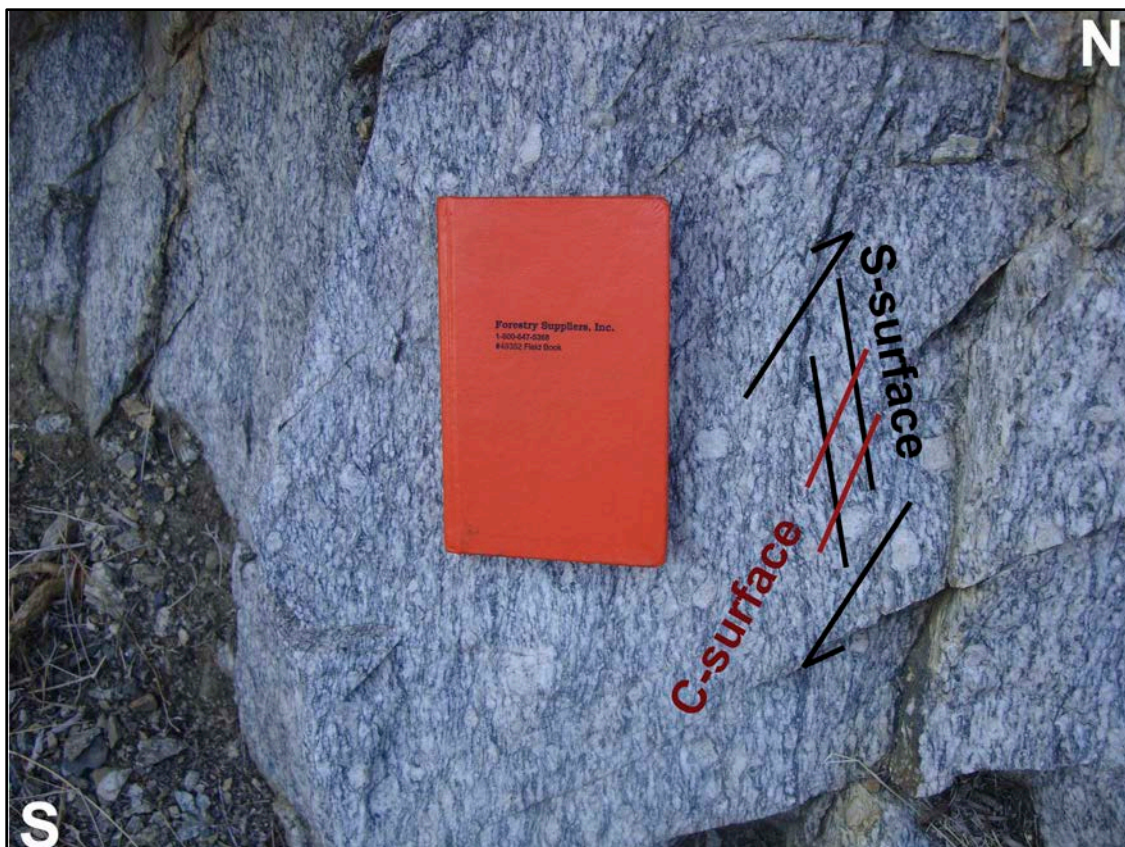


Figure 8. Example of top-north shear within the mylonitic granodiorite (Kmg). Photograph was taken near the mouth of Pleasant Canyon on the northern canyon wall.

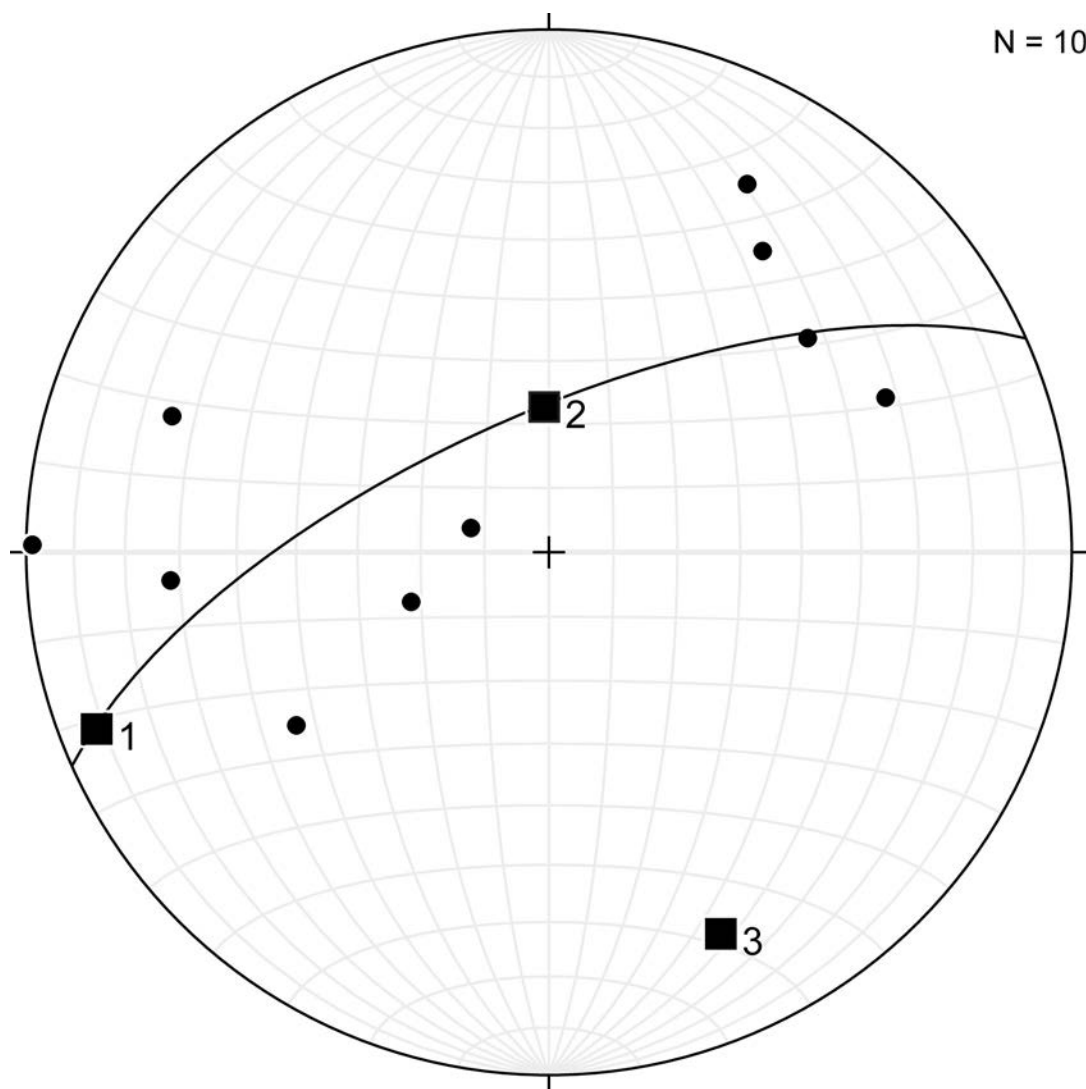


Figure 9. Stereonet plot of poles to planes of crenulation cleavage (S3) associated with D3. The best fit great circle has a strike and dip of $245.9/68.5^{\circ}$ and a π -pole that plunges 21.5° toward 155.9 .

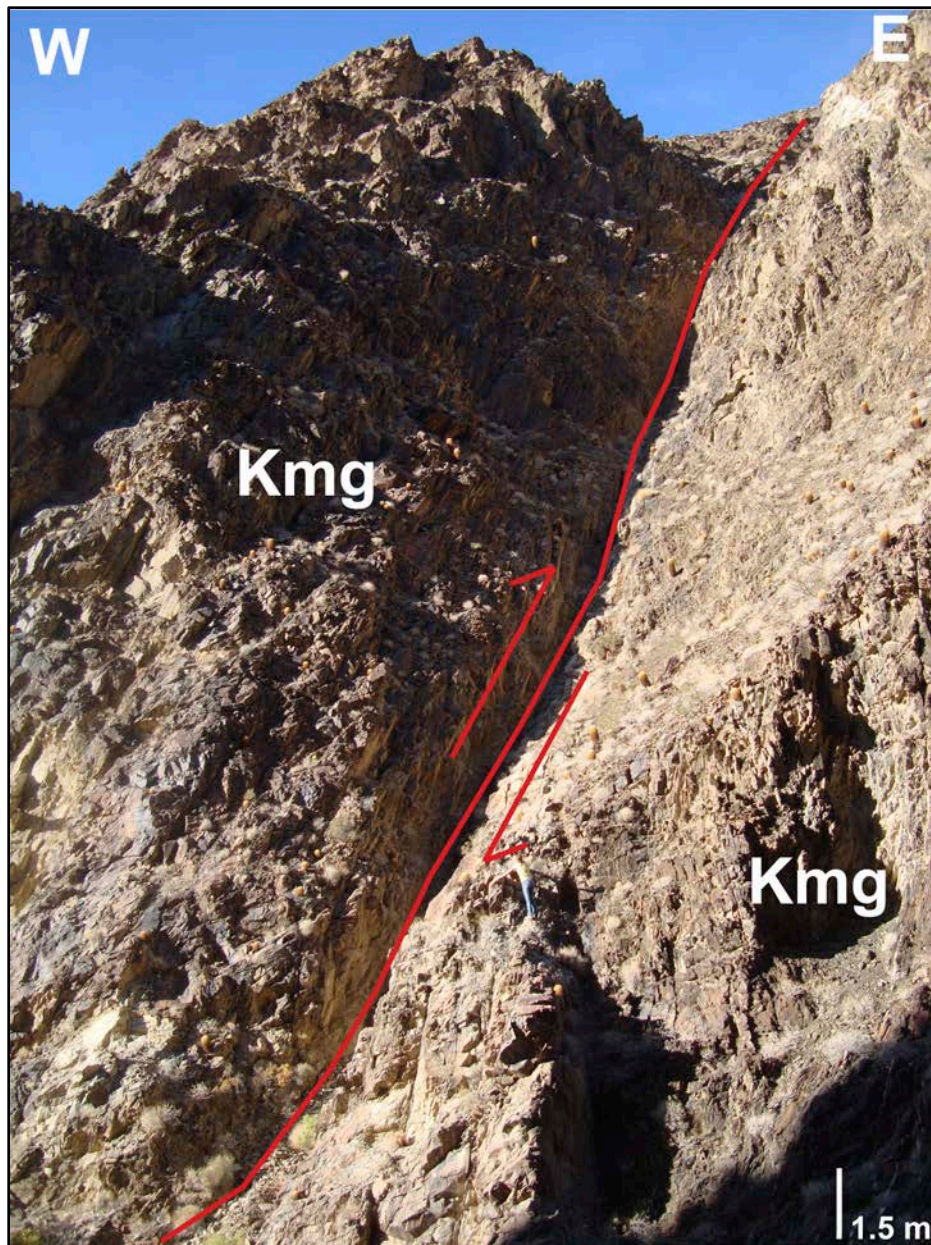


Figure 10. Photograph of the reverse fault in the mylonitic granodiorite (Kmg) slightly east of the South Park Fault. The mylonitic granodiorite intrusion is in the hanging wall as well as the footwall of the reverse fault.

Figure 11. Example dialog boxes from *ArcPad* Version 10 used for digital mapping in this research. This figure shows the type of data that can be collected when drawing contacts (left) and recording structural orientations (right). Detailed descriptions of the digital mapping workflow can be found Pavlis et al. (2010).

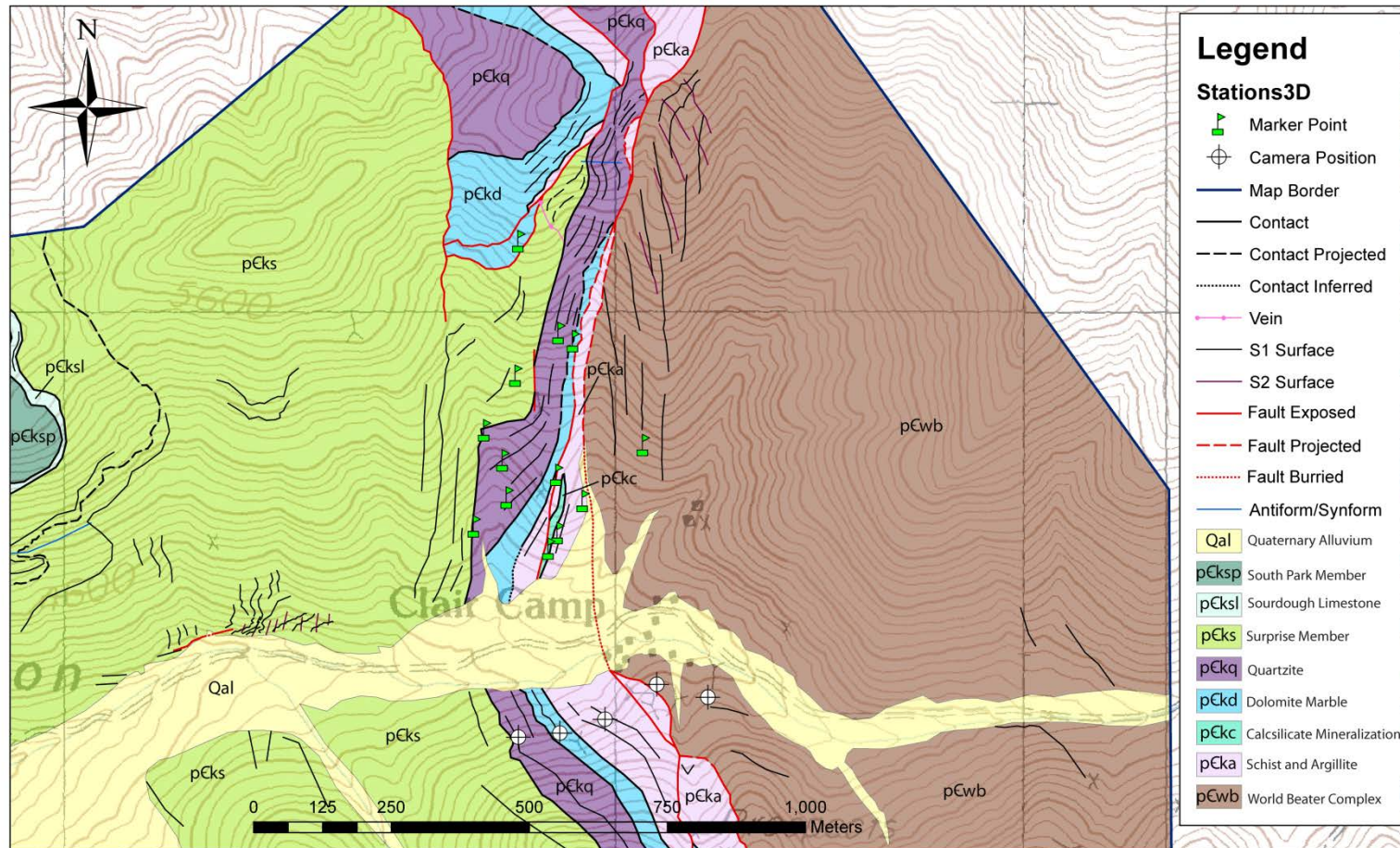


Figure 12. Geologic map of Pleasant Canyon focusing on the Clair Camp Structure (north of Clair Camp). Thirteen marker points (green flags) are located throughout the Clair Camp Structure chosen for photogrammetry. Five camera positions (white circles with crosses) are located south of Clair Camp.

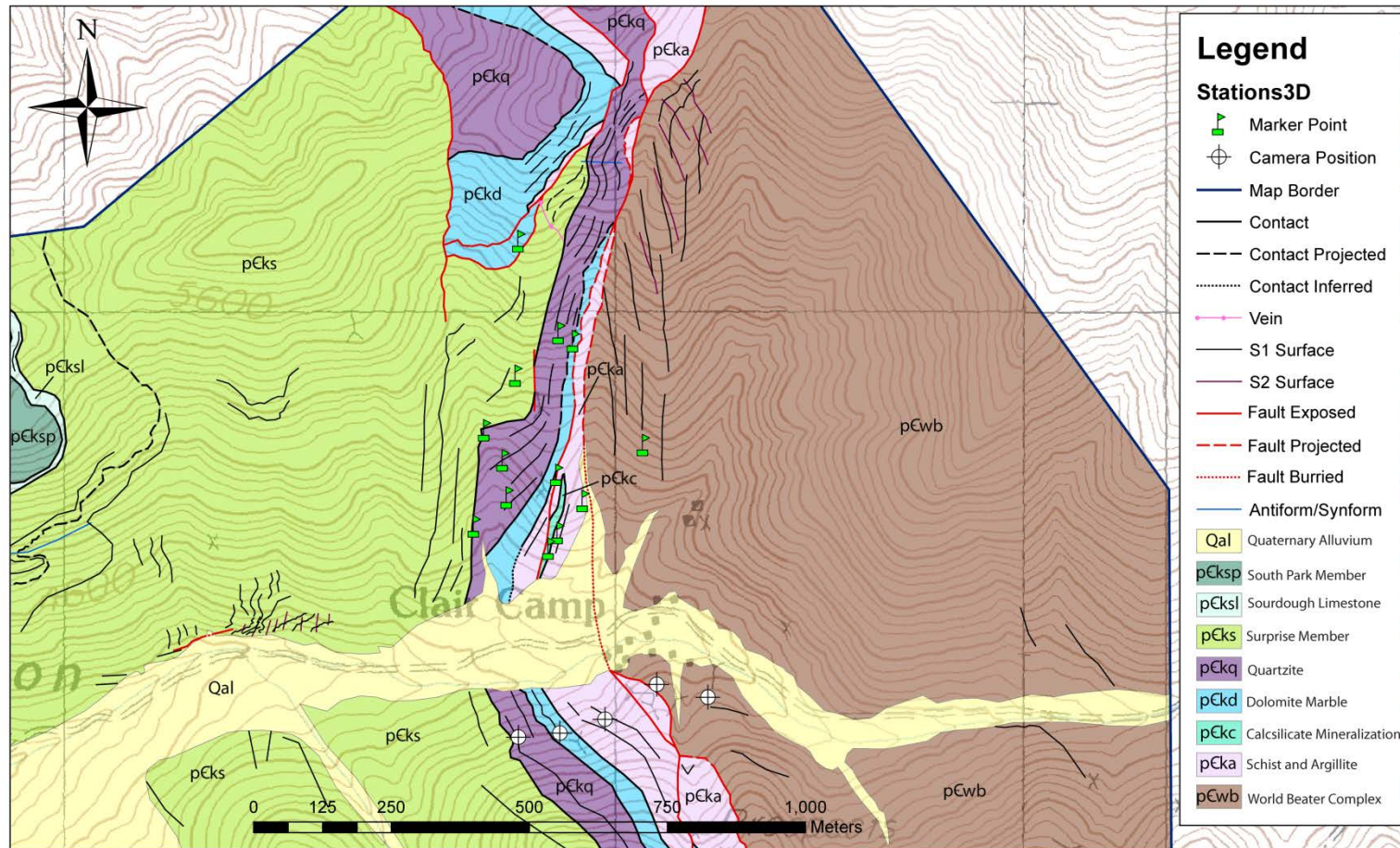


Figure 13. Geologic map of Pleasant Canyon focusing on the Noonday Structure (north wall of Pleasant Canyon that includes the Noonday Dolomite). No marker points were obtained in the field, but ten camera positions (white circles with crosses) are located on the southern ridge of Pleasant Canyon.



Figure 14. Photograph of the Riegl LMS-Z620 TLS used to collect LiDAR data of Pleasant Canyon. The Reigl LMS-Z620 is equipped with a differential GPS receiver and has a Nikon D700 camera mounted on top. This photograph was taken at the Clair Camp site looking southwest.

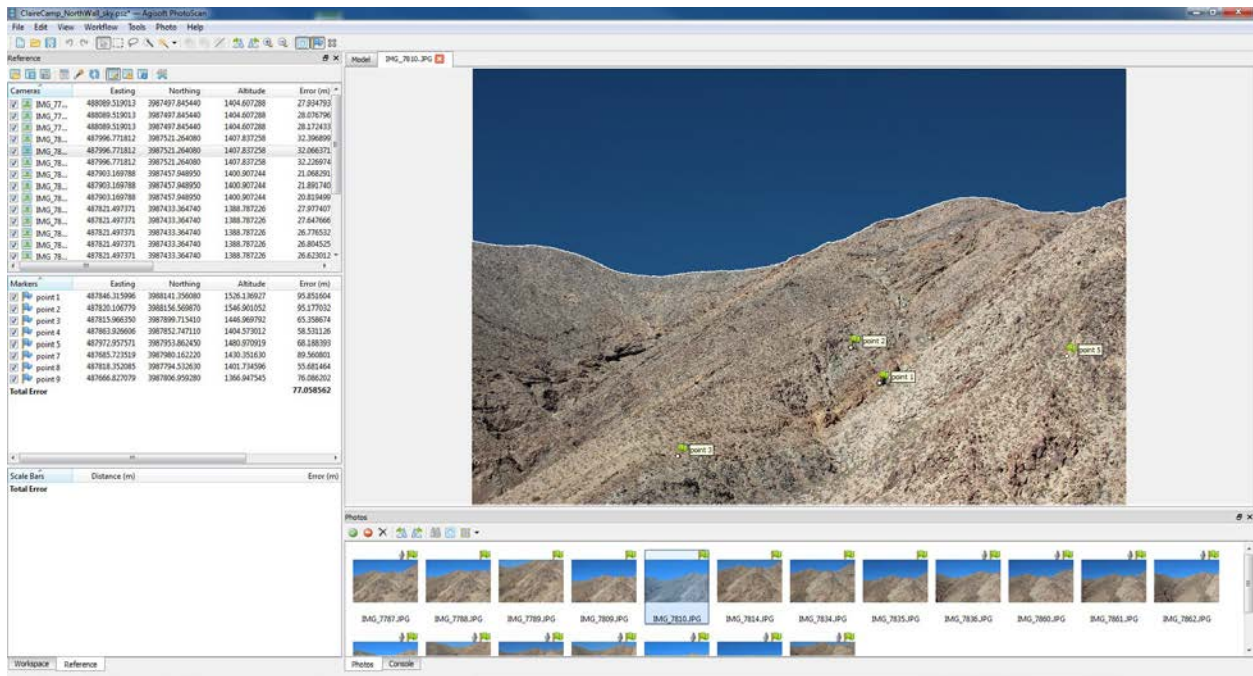


Figure 15. Screenshot of the *PhotoScan* project for the Clair Camp Structure. In the viewing pane (right) image 7810 is selected from the “Photos” window (bottom right). Within the viewing pane, images can be masked. This screenshot shows the sky has been masked, as denoted by the dark blue color and gray outline along the ridge. The viewing pane is also where marker points are placed in photographs (four of the eight marker points are located in image 7810 and represented by green flags). The GPS coordinates (latitude, longitude, and elevation) for each of the marker points are entered into the “Markers” table (middle left window). GPS coordinates for the camera positions are entered into the “Cameras” table (upper left window). Once camera positions are entered, each photograph can be selected and assigned to the camera position where the photograph was taken.

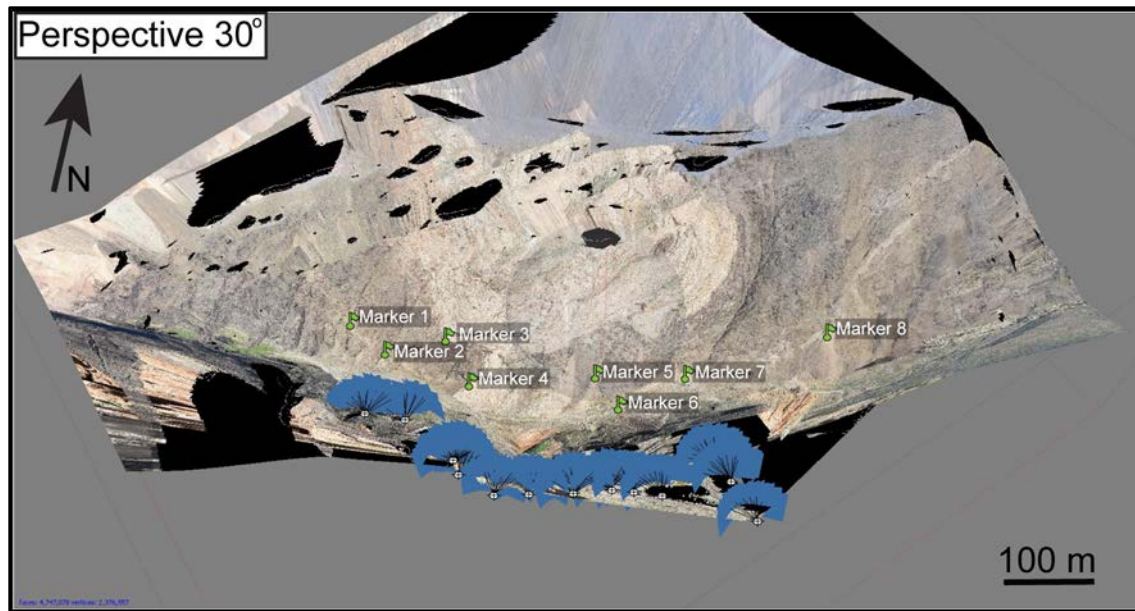


Figure 16. Image from *PhotoScan* showing the photogrammetrically-derived point-cloud of the Noonday Structure including the locations of the eight marker points (green flags) obtained from the LiDAR point-cloud. This image also includes the ten camera positions (circled crosses) and the rays representing the lens axis of each photograph taken (photographs are represented as blue planes) at each camera position.

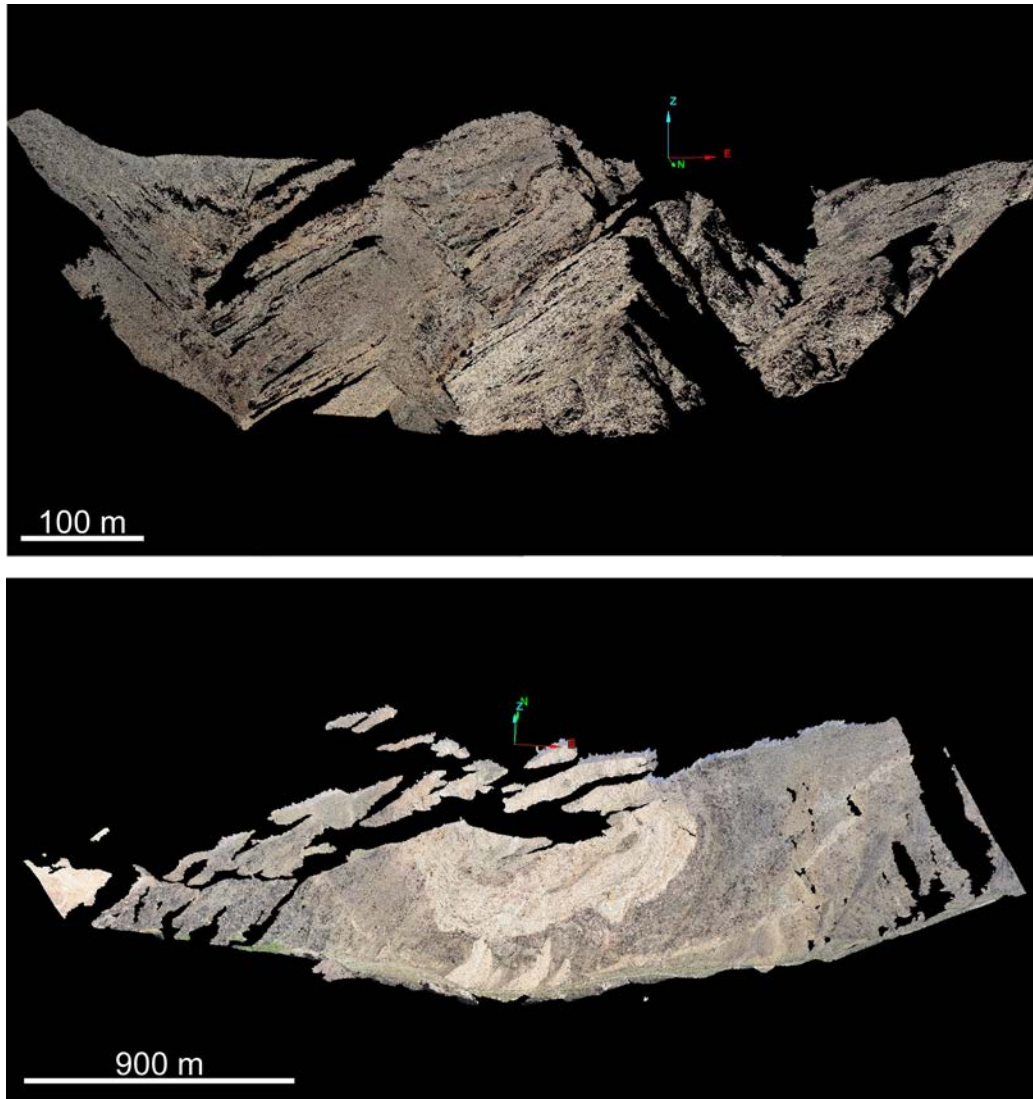


Figure 17. Dense points-clouds of the Clair Camp Structure (top) and the Noonday Structure (bottom) made using *PhotoScan* and viewed using *Maptek I-Site*. The dense point-cloud of the Clair Camp Structure was made using the ultra-high setting, while the dense point-cloud of the Noonday Structure was made using the high setting. Refer to text for further description.

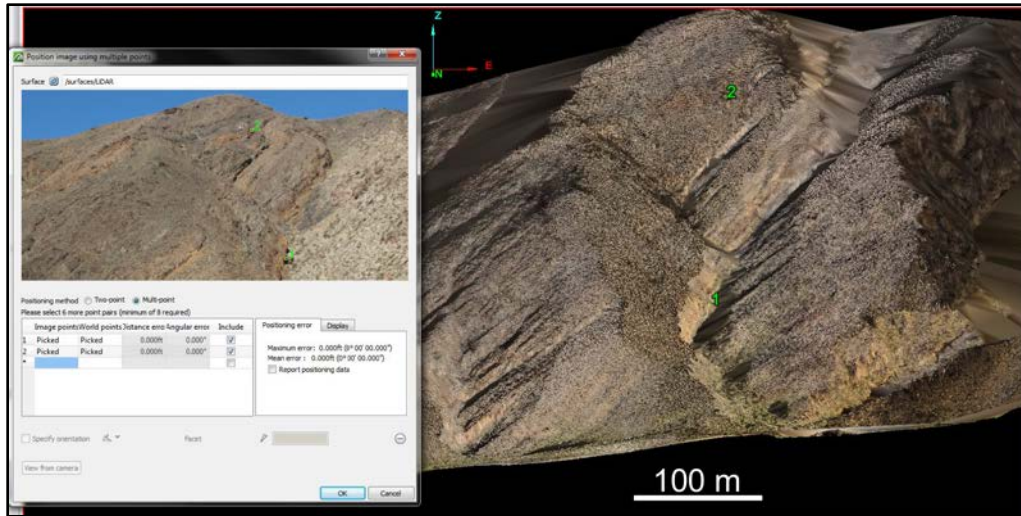


Figure 18. Screenshot showing the photograph draping process in *I-Site*. This example is of the Clair Camp Structure. The dialog box (left) contains the photograph being draped. A feature is chosen in the photograph and manually selected to create a point and then the same feature is manually selected in the model to create a point pair.

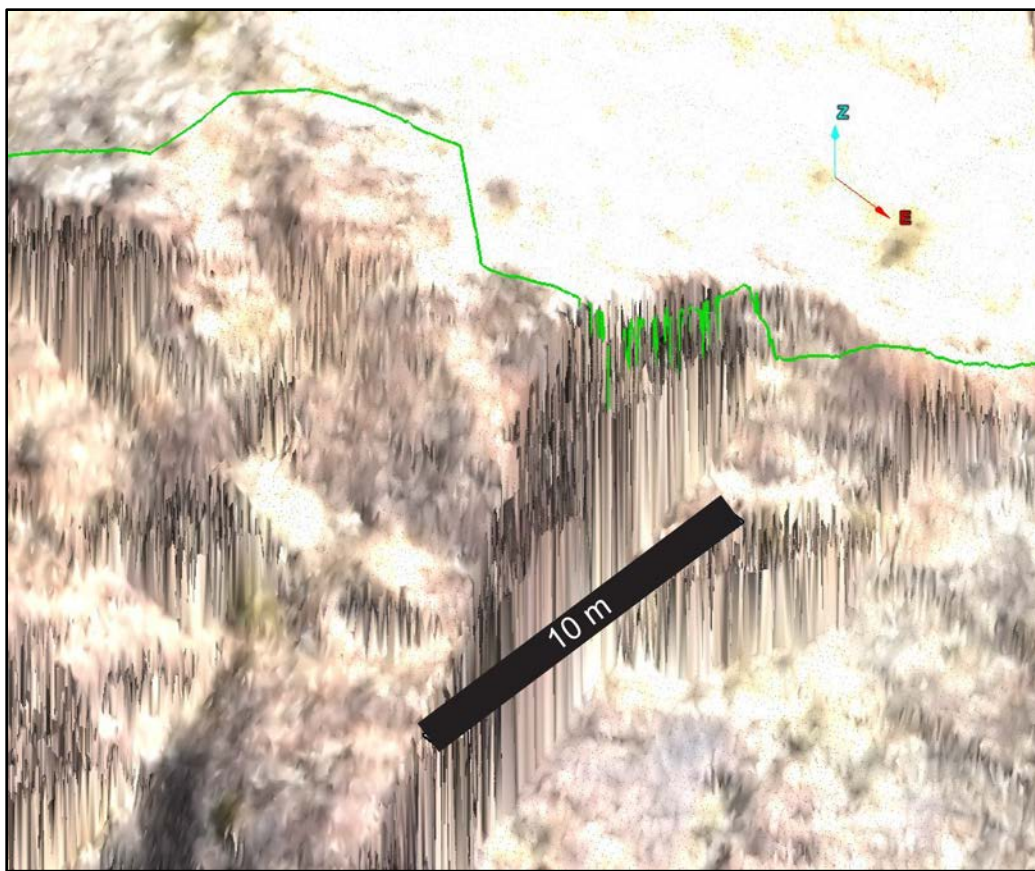


Figure19. Image showing a close-up of the photogrammetrically-derived terrain model of the Noonday Structure. The interpretation in green represents the base of the Noonday Dolomite. On steep cliff faces, the interpretation shows errors in the Z-direction.

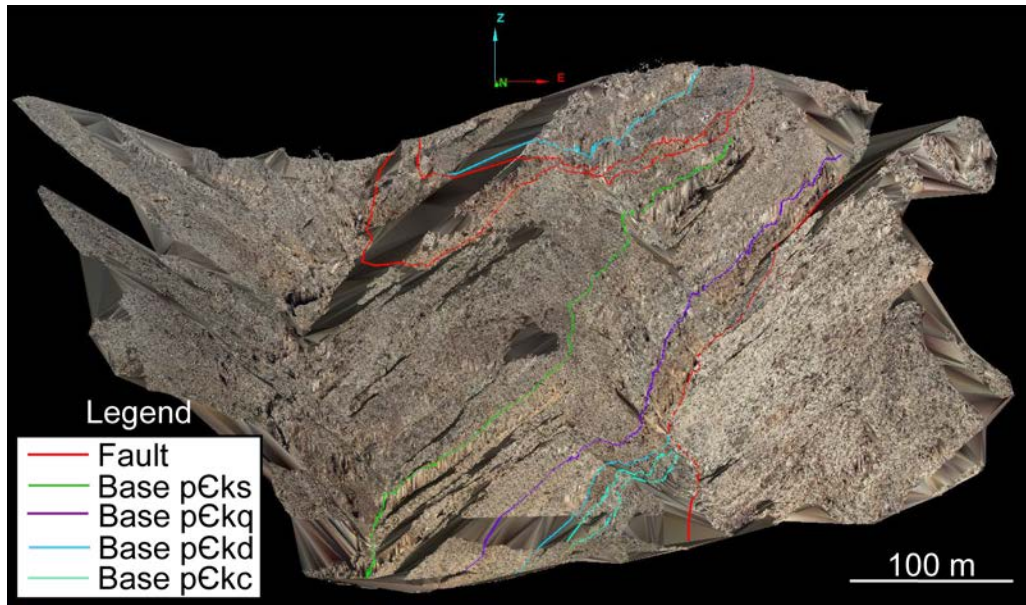


Figure 20. Image of the photogrammetrically-derived terrain model of the Clair Camp Structure with 3D interpretations viewed in *I-Site*. p€ks = Surprise Member of the Kingston Peak Formation, p€kq = Quartzite unit within the Kingston Peak Formation, p€kd = Dolomite Marble unit within the Kingston Peak Formation, and p€kc = Calc-silicate Mineralization within the Kingston Peak Formation. Refer to Animation 1, Appendix 1.

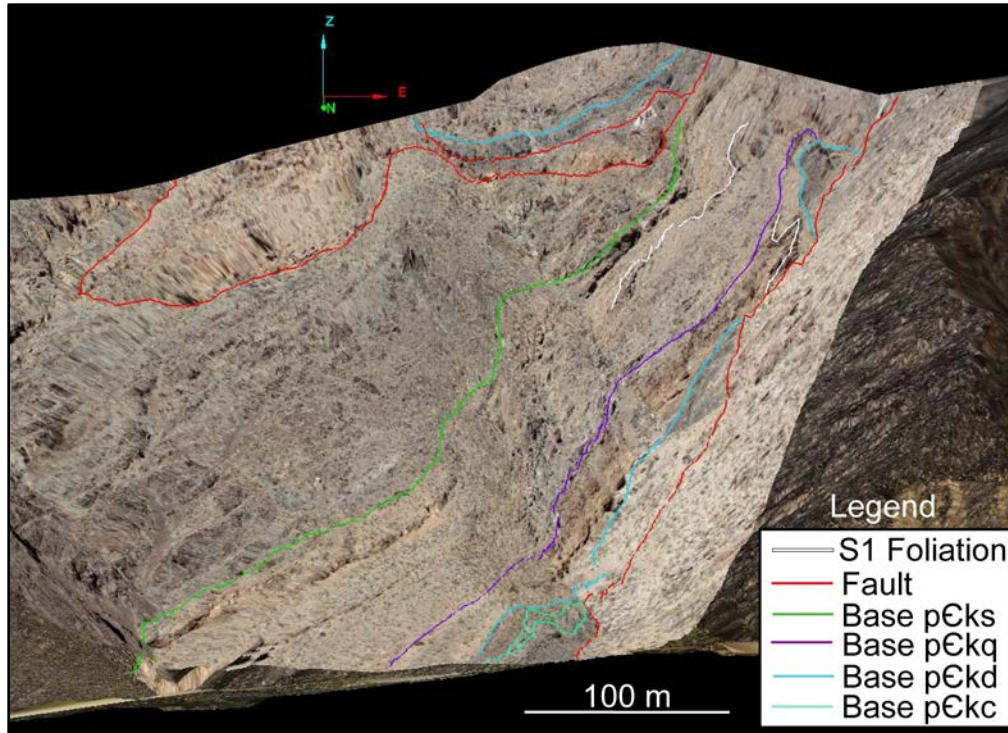


Figure 21. Image of the TLS-derived terrain model of the Clair Camp Structure with 3D interpretations viewed in *I-Site*. pCks = Surprise Member of the Kingston Peak Formation, pCkq = Quartzite unit within the Kingston Peak Formation, pCkd = Dolomite Marble unit within the Kingston Peak Formation, and pCkc = Calc-silicate Mineralization within the Kingston Peak Formation. Refer to Animation 2, Appendix 1.

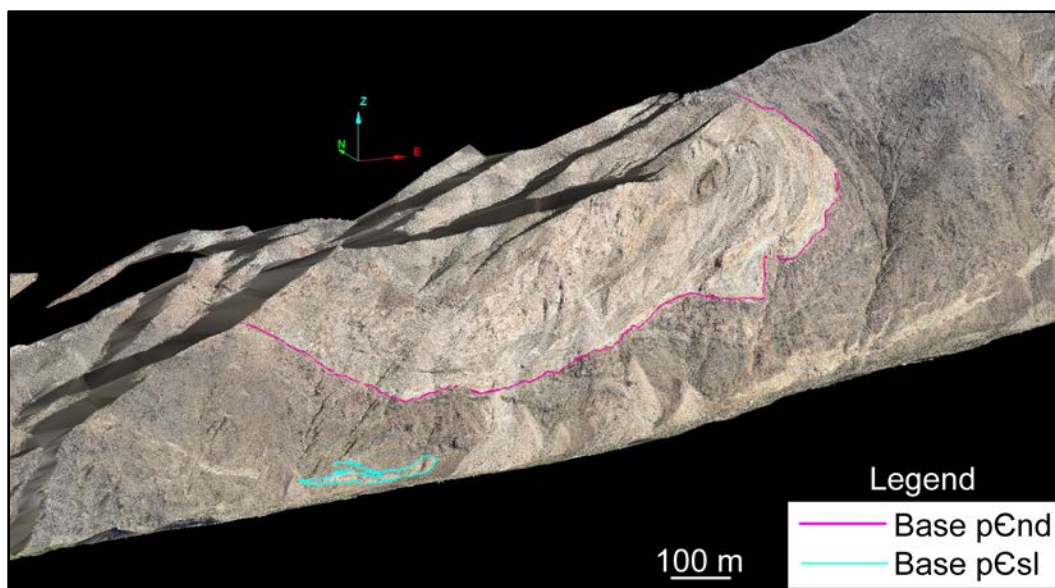


Figure 22. Image of the photogrammetrically-derived terrain model of the Noonday Structure with 3D interpretations viewed in *I-Site*. pEnd = Noonday Dolomite, and pCsl = Sourdough Limestone Member of the Kingston Peak Formation. Refer to Animation 3, Appendix 1.

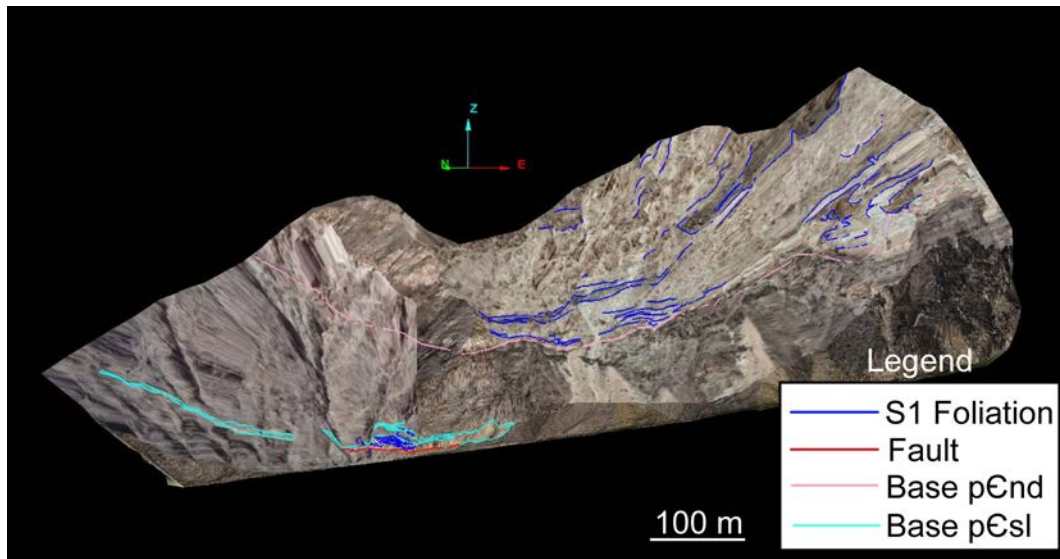


Figure 23. Image of the TLS-derived terrain model of the Noonday Structure with 3D interpretations viewed in *I-Site*. pCnd = Noonday Dolomite, and pCsl = Sourdough Limestone Member of the Kingston Peak Formation. Refer to Animation 4, Appendix 1.

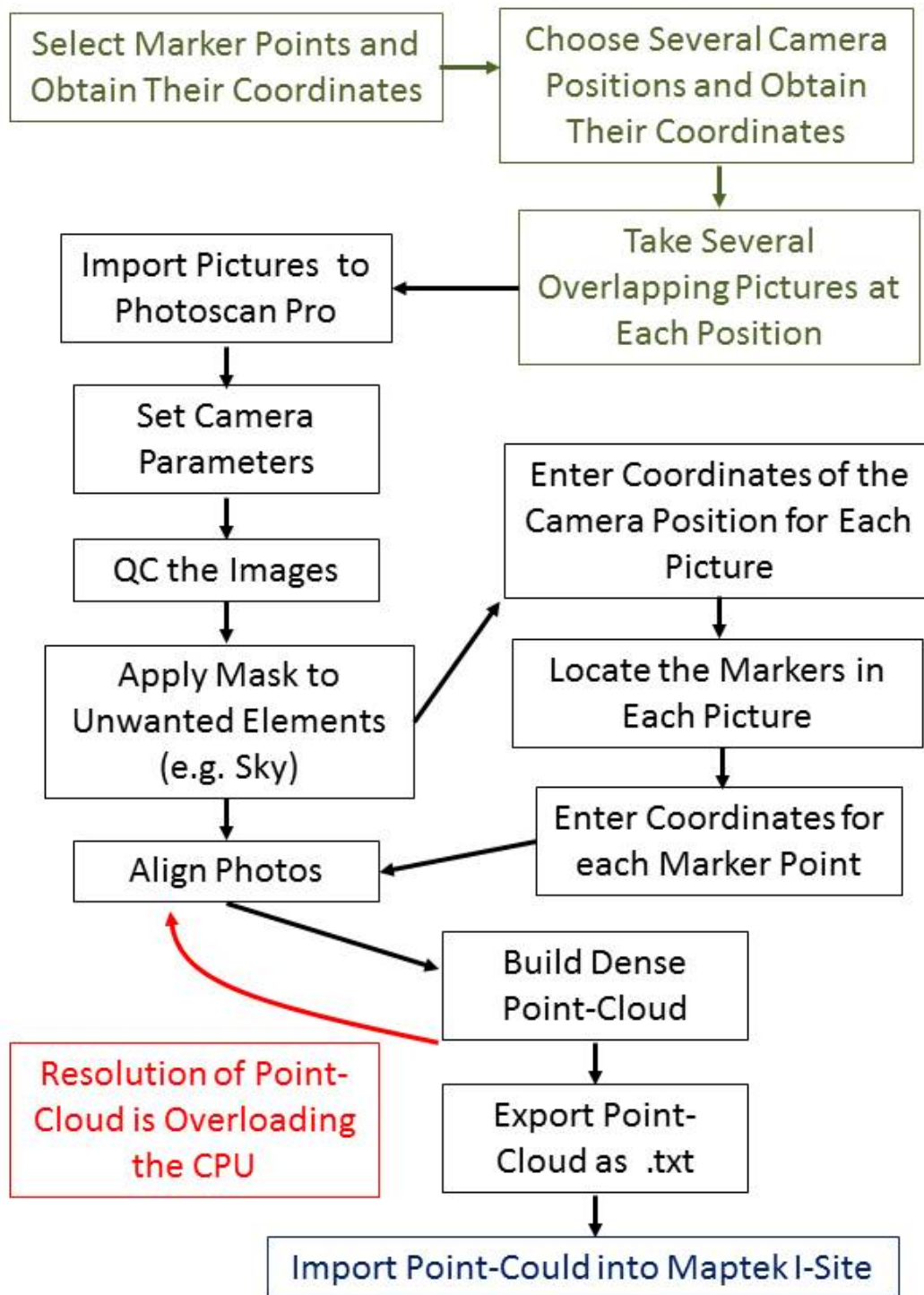


Figure 24. Diagram showing the general workflow used to build a point-cloud using photogrammetry. Sage green boxes represents the steps that were taken in the field, black boxes represent steps required to build a point-cloud using *PhotoScan*, red boxes represent potential issues, and the blue box represents processing in *Maptek I-Site*.

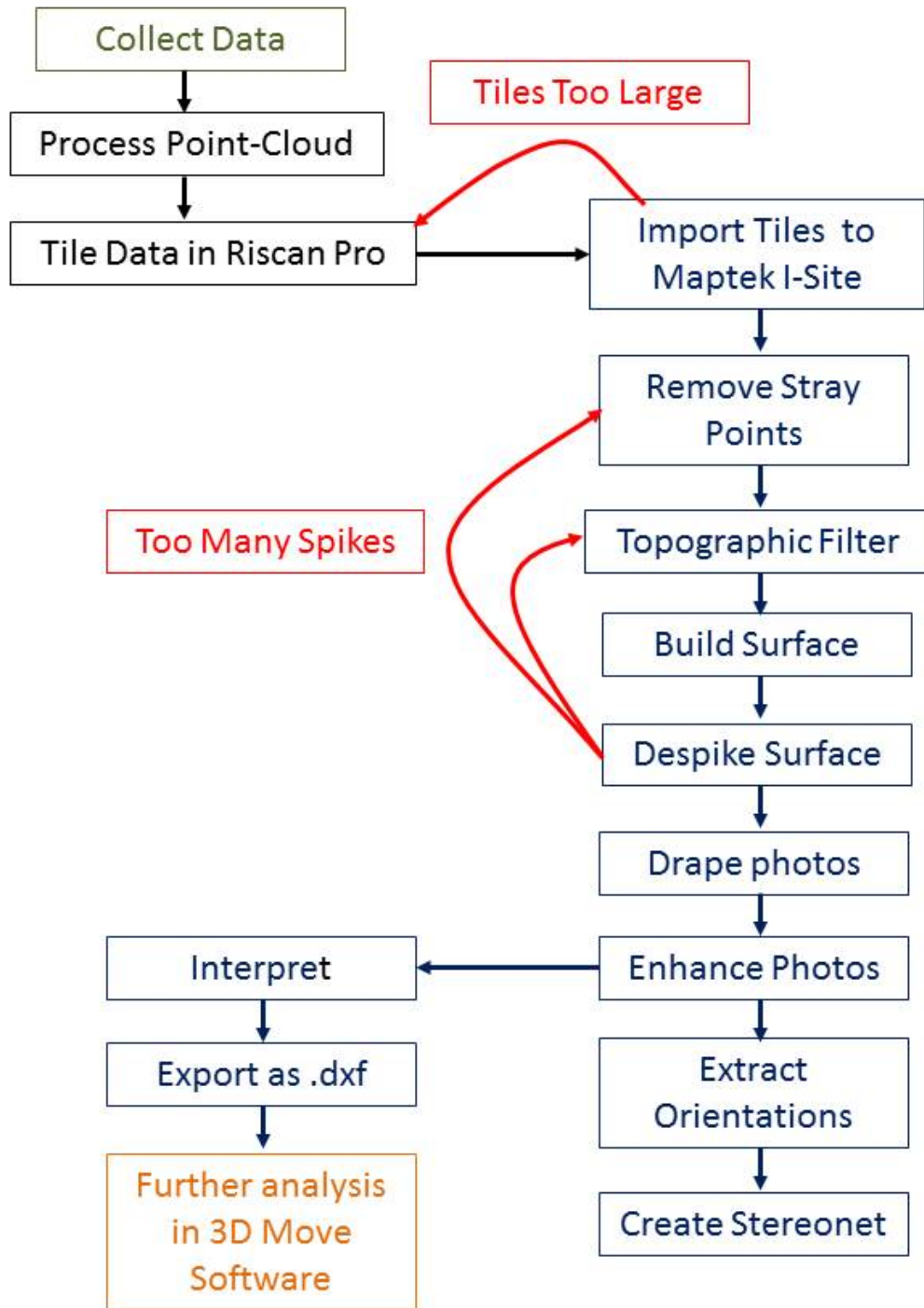


Figure 25. Diagram showing the general workflow for collecting and processing TLS data. The green box represents the step performed in the field, the black boxes represent the steps required to process the TLS point-cloud using *RiScan Professional*, the blue boxes represent the steps required to build terrain modes using *Maptek I-Site*, the red boxes represent potential issues, and the orange box represents additional processing in *MOVE*.

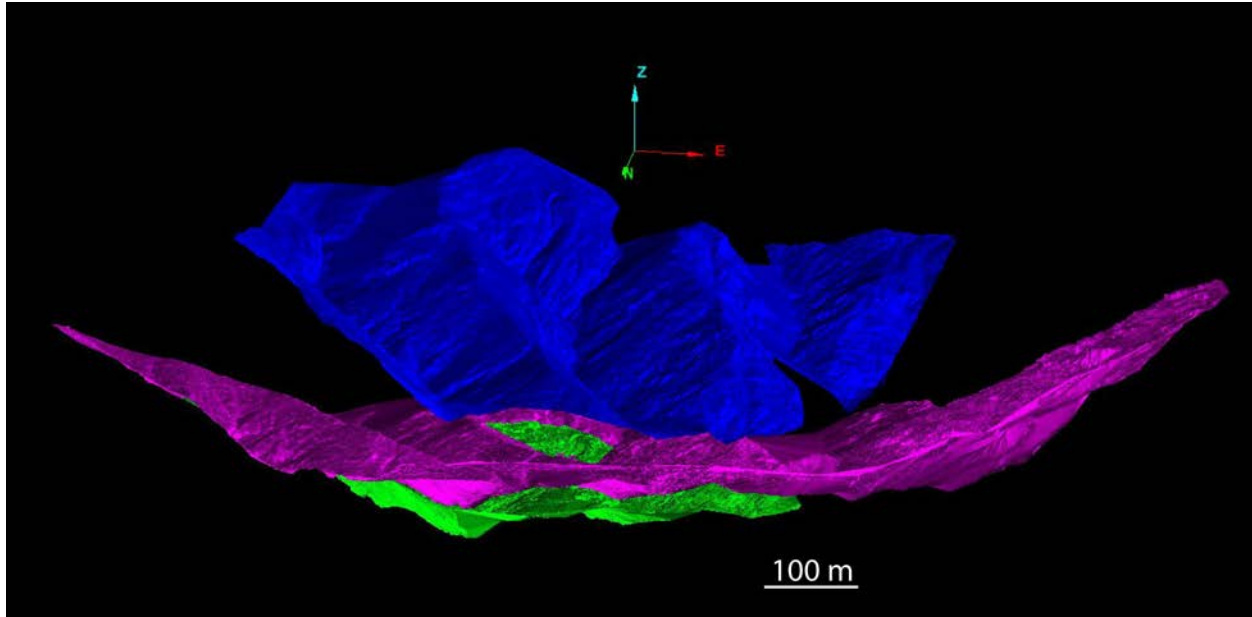


Figure 26. Image of the visual comparison viewed in *I-Site* between the marker-less photogrammetrically-derived TIN of the Clair Camp Structure (blue), the TLS-derived TIN (pink), and the photogrammetrically-derived TIN of the Clair Camp Structure that utilized marker points (green). The TLS-derived TIN (pink) is used as a reference. The marker-less photogrammetrically-derived TIN (blue) is located well above the TLS-derived TIN, while the photogrammetrically-derived TIN that utilized marker points (green) is situated slightly underneath the TLS-derived TIN of the Clair Camp Structure. Refer to Animation 5, Appendix 1.

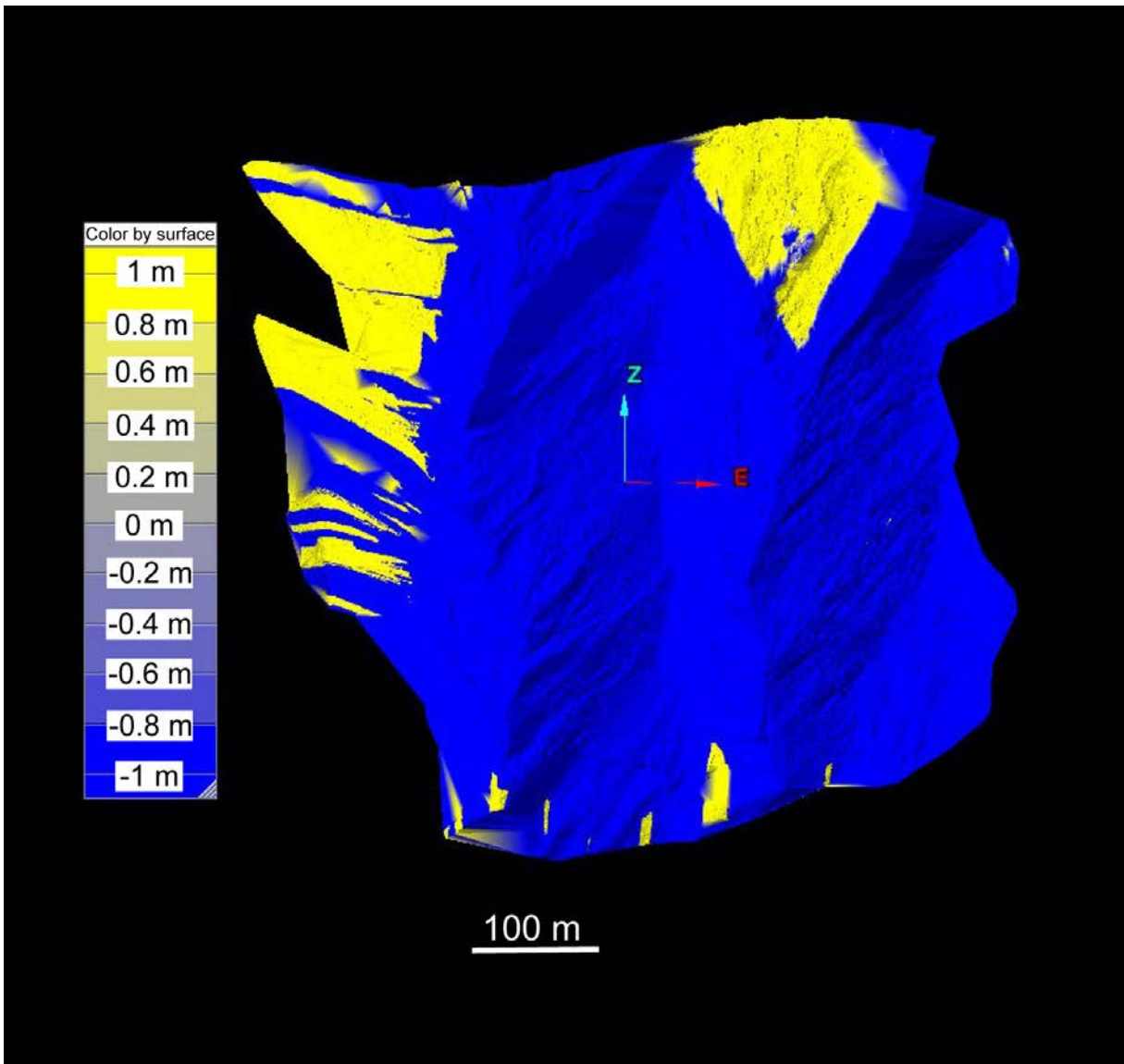


Figure 27. Image of the result of surface analysis in *I-Site*. This image shows the photogrammetrically-derived TIN of the Clair Camp Structure colored by the amount it is offset from the TLS-derived TIN of the Clair Camp Structure. Areas that are colored yellow indicate that that area is situated above the surface of the TLS-derived TIN of the Clair Camp Structure, and areas that are colored blue are situated below the surface of the TLS-derived TIN.

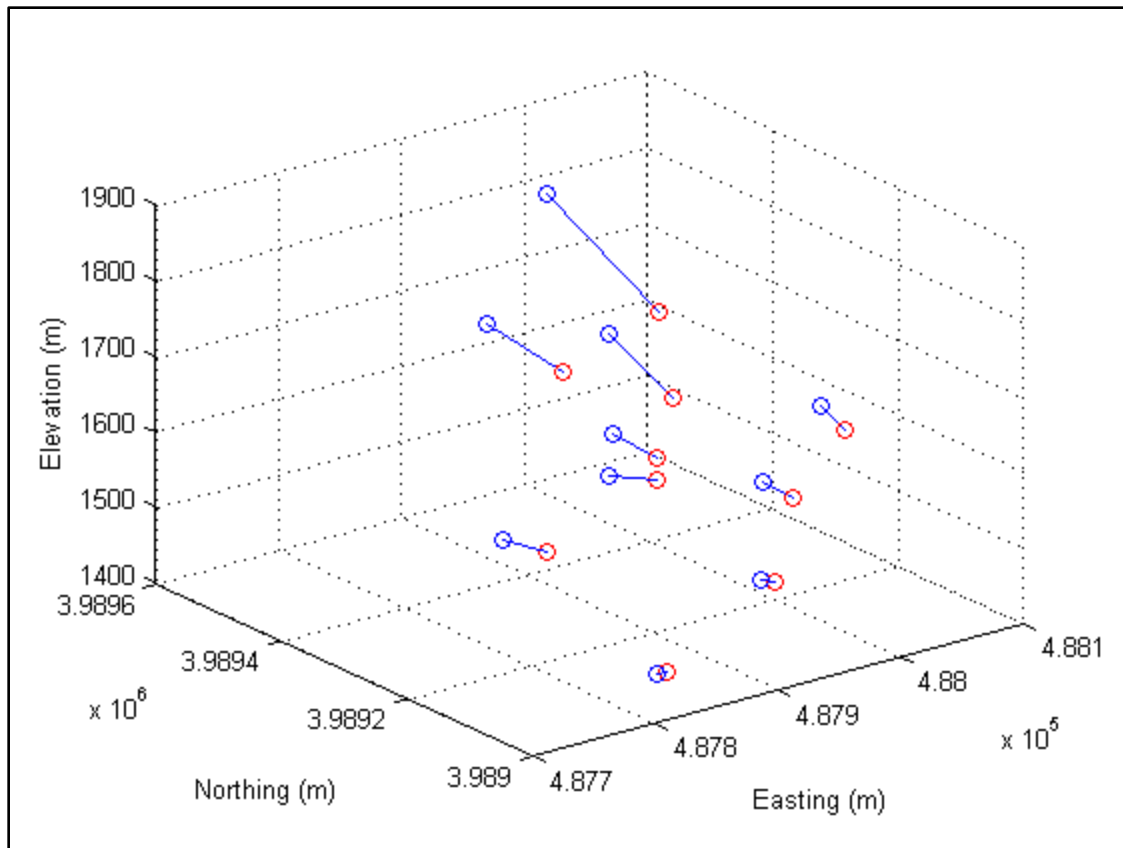


Figure 28. MATLAB figure showing the calculations for the amount of offset between ten control points located on the photogrammetrically-derived TIN of the Clair Camp Structure (red circles) and their counterparts on the TLS-derived TIN of the Clair Camp Structure (blue circles). Distance and direction of offset is indicated by the blue line connected pairs of circles. This figure shows that offset between points increases the farther the points are from the origin (camera positions).

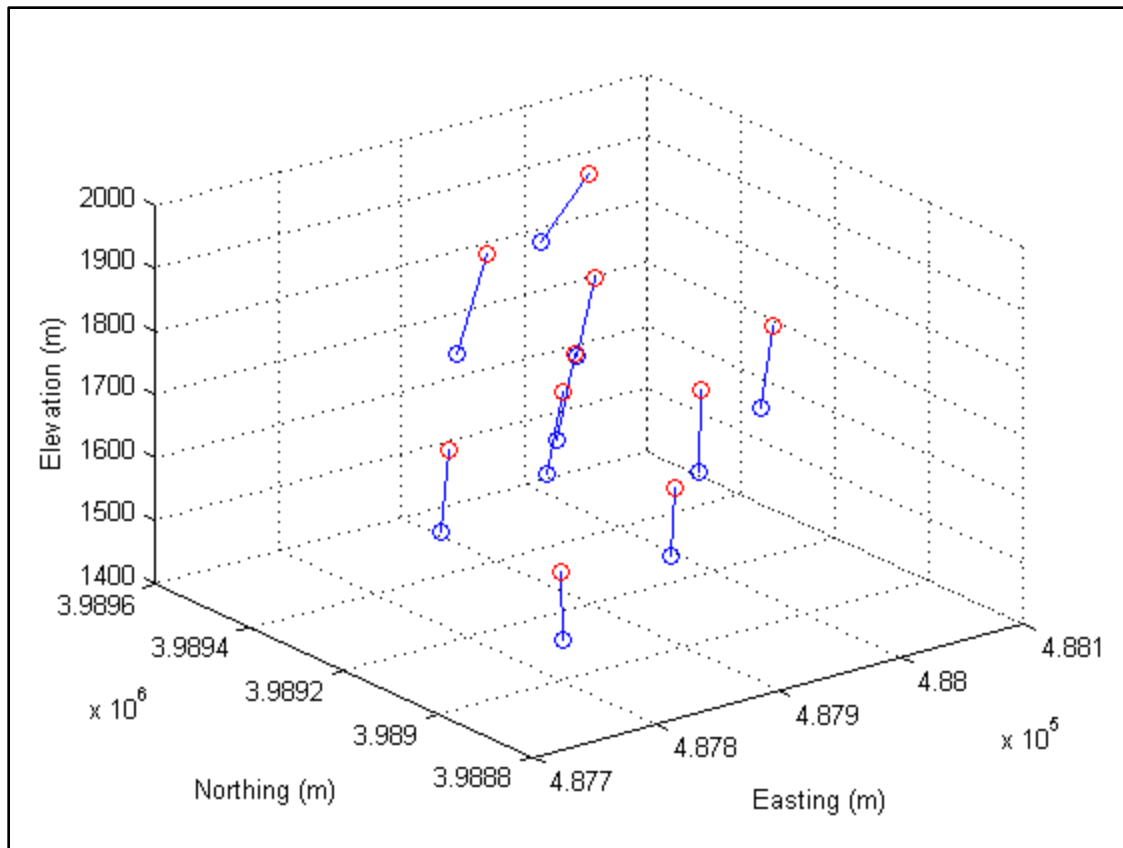


Figure 29. MATLAB figure showing the calculations for the amount of offset between ten control points located on the marker-less photogrammetrically-derived TIN of the Clair Camp Structure (red circles) and their counterparts on the TLS-derived TIN of the Clair Camp Structure (blue circles). Distance and direction of offset is indicated by the blue line connected pairs of circles. This figure shows that offset between points increases the farther the points are from the origin (camera positions).

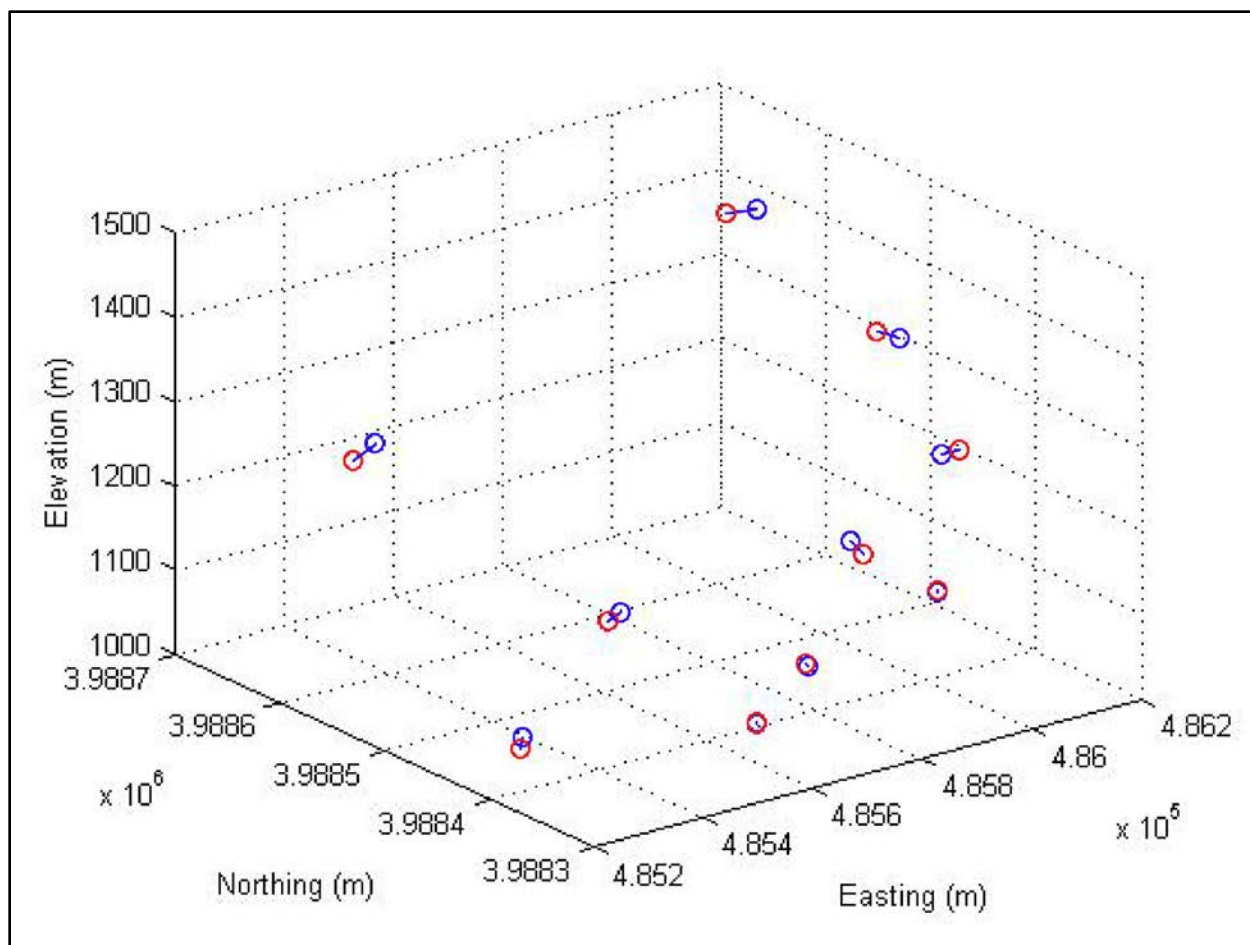


Figure 30. MATLAB figure showing the calculations for the amount of offset between ten control points located on the photogrammetrically-derived TIN of the Noonday Structure (red circles) and their counterparts on the TLS-derived TIN of the Noonday Structure (blue circles). Distance and direction of offset is indicated by the blue line connected pairs of circles. This figure shows that offset between points increases the farther the points are from the origin (camera positions).

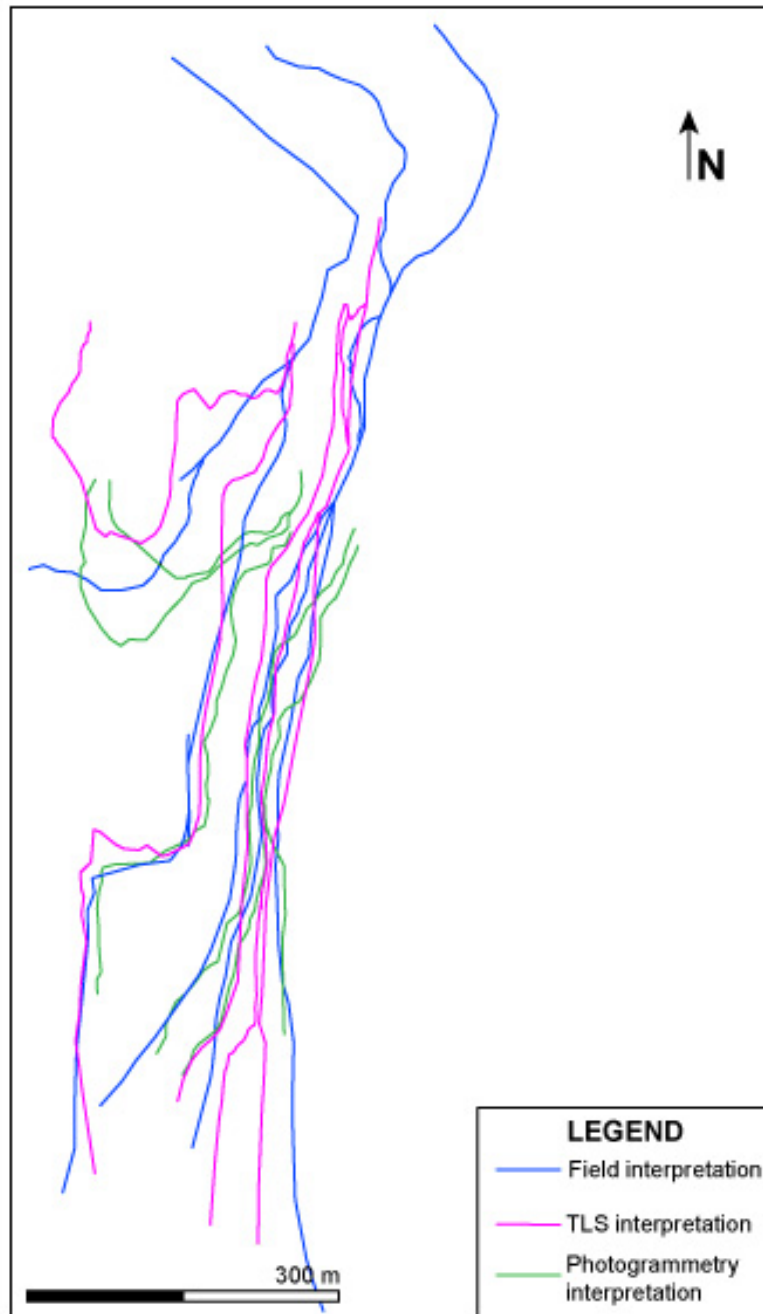


Figure 31. Map view of interpretations from the Clair Camp Structure made using *MOVE*: blue lines are interpretations that were made in the field, pink lines are interpretations that were made using the TLS-derived terrain model, and green lines are interpretations that were made using the photogrammetrically-derived terrain model of the Clair Camp Structure. The terrain model-derived interpretations follow the trend of the field interpretations, but deviate at the ridge (north end of the map).

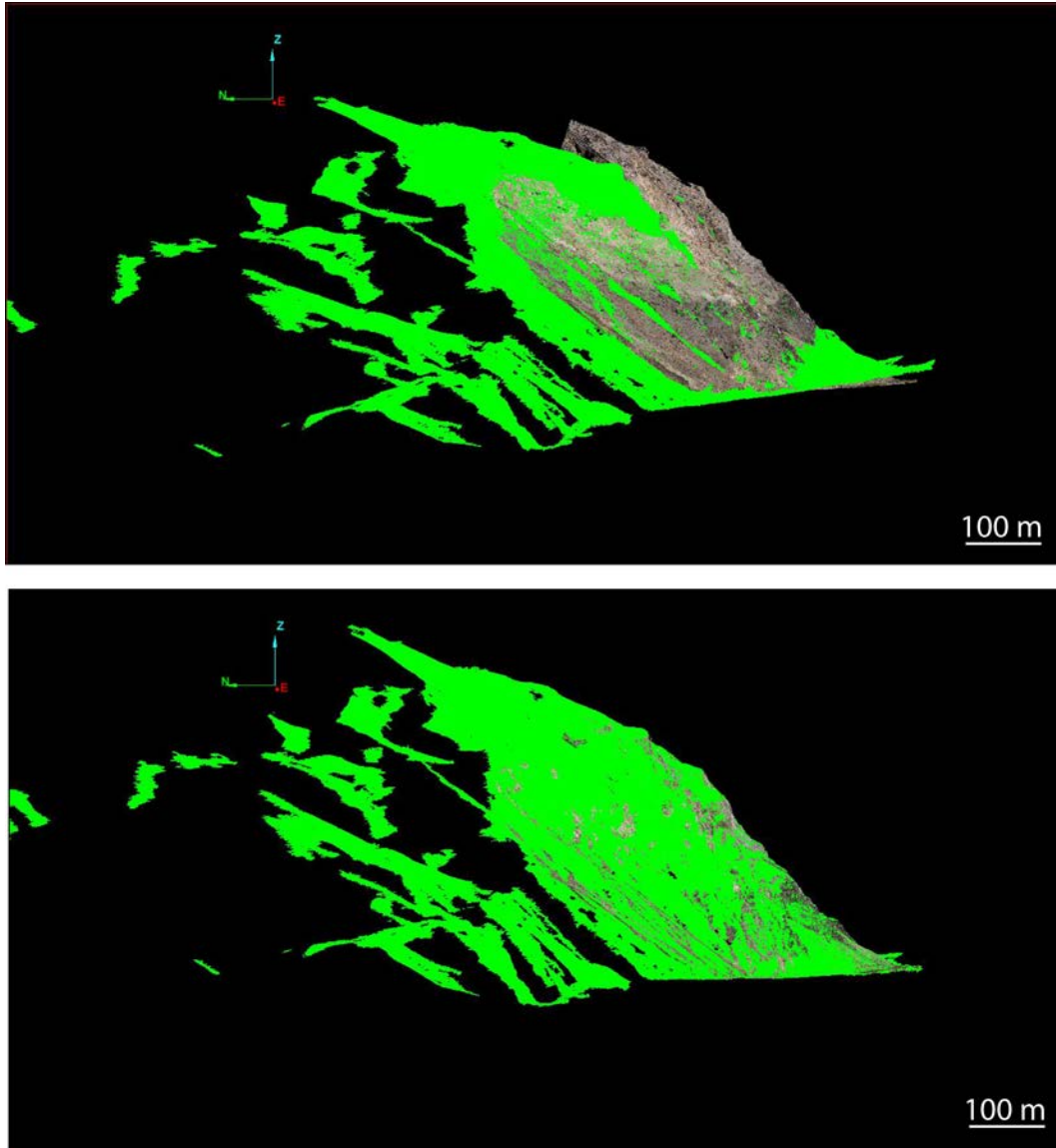


Figure 32. Images from *I-Site* showing the photogrammetrically-derived point-cloud (green) and the TLS-derived point-cloud (true color) of the Noonday Structure before registration (top) and after registration (bottom). The TLS-derived point-cloud of the Noonday Structure was used as the reference for registration of the photogrammetrically-derived point-cloud. Registration resulted in a spatially accurate photogrammetrically-derived point-cloud of the Noonday Structure.

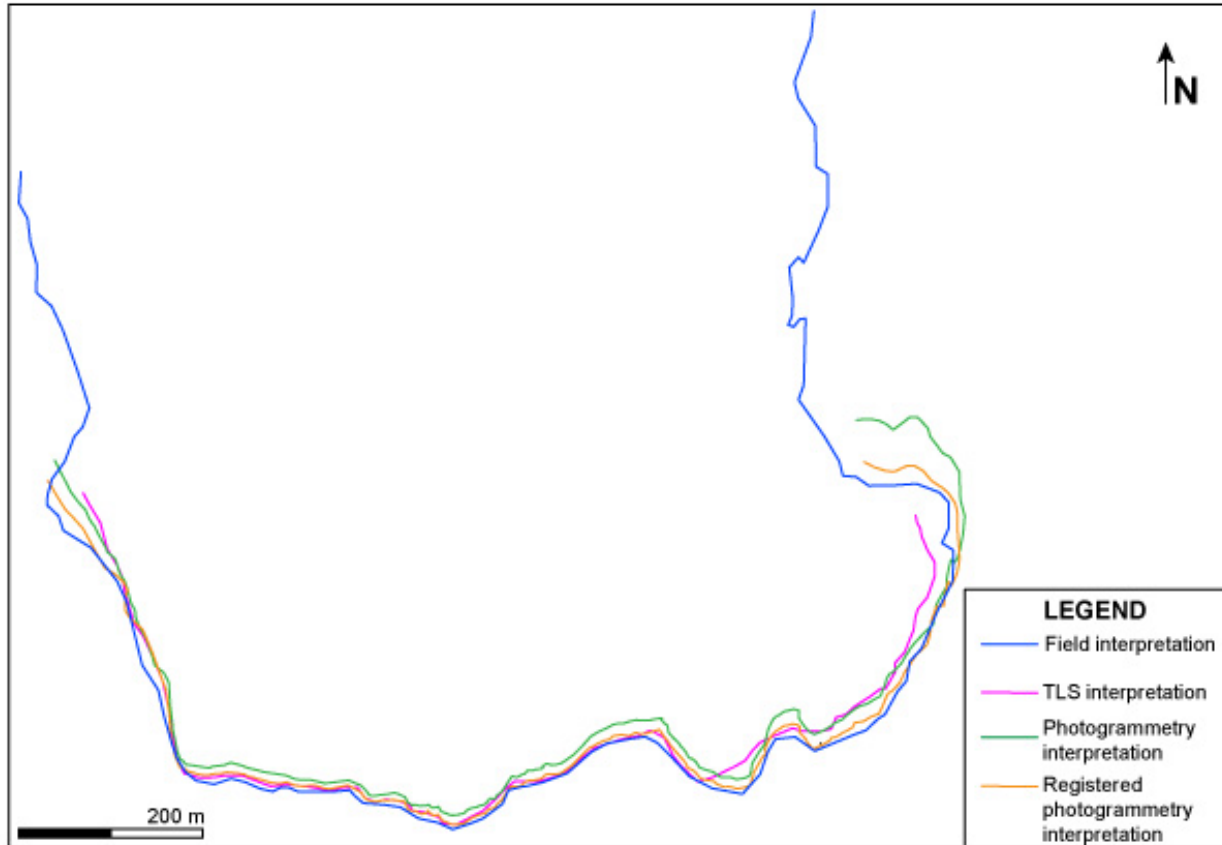


Figure 33. Map view of interpretations from the Noonday Structure made using *MOVE*. All interpretations represent the base of the Noonday Dolomite. The blue line is the interpretation that was made in the field, the pink line is the interpretation made using the TLS-derived terrain model, the green line is the interpretation made using the photogrammetrically-derived terrain model, and the yellow line is the interpretation made using the registered photogrammetrically-derived terrain model of the Noonday Structure. All interpretations appear to follow the same trend in map view, except on the east side where the terrain model-derived interpretations deviate.

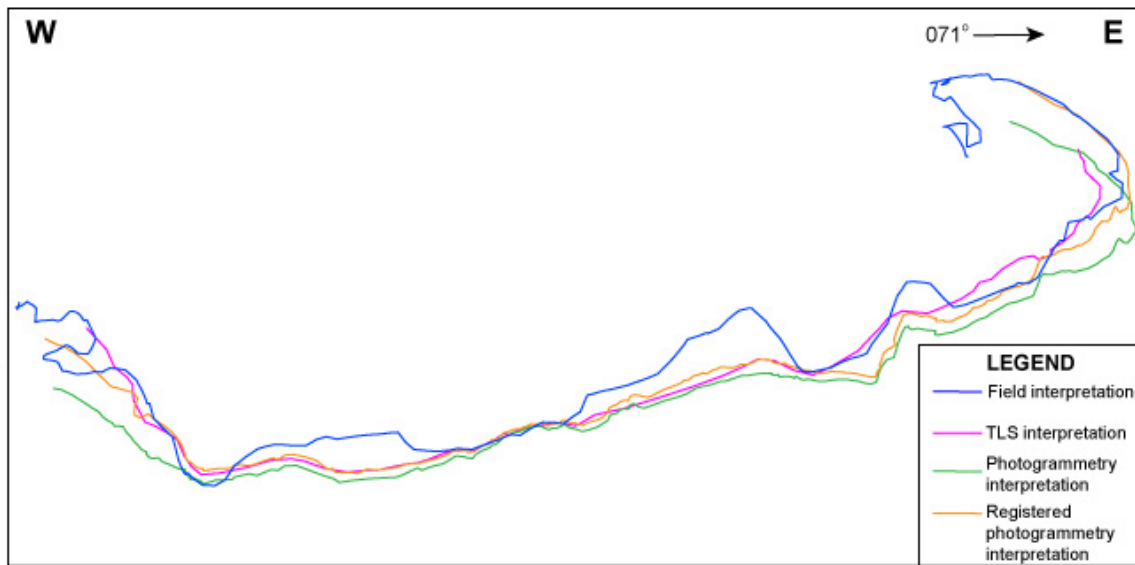


Figure 34. Cross-section of interpretations from the Noonday Structure made using *MOVE*. All interpretations represent the base of the Noonday Dolomite. The blue line is the interpretation that was made in the field, the pink line is the interpretation made using the TLS-derived terrain model, the green line is the interpretation made using the photogrammetrically-derived terrain model, and the yellow line is the interpretation made using the registered photogrammetrically-derived terrain model of the Noonday Structure. All of the terrain model-derived interpretations appear to follow the same trend, but the field interpretation has a unique character. The reason the field interpretation is different from the terrain model interpretations is most likely due to the limitations of mapping contacts on cliff faces using a 2D map.

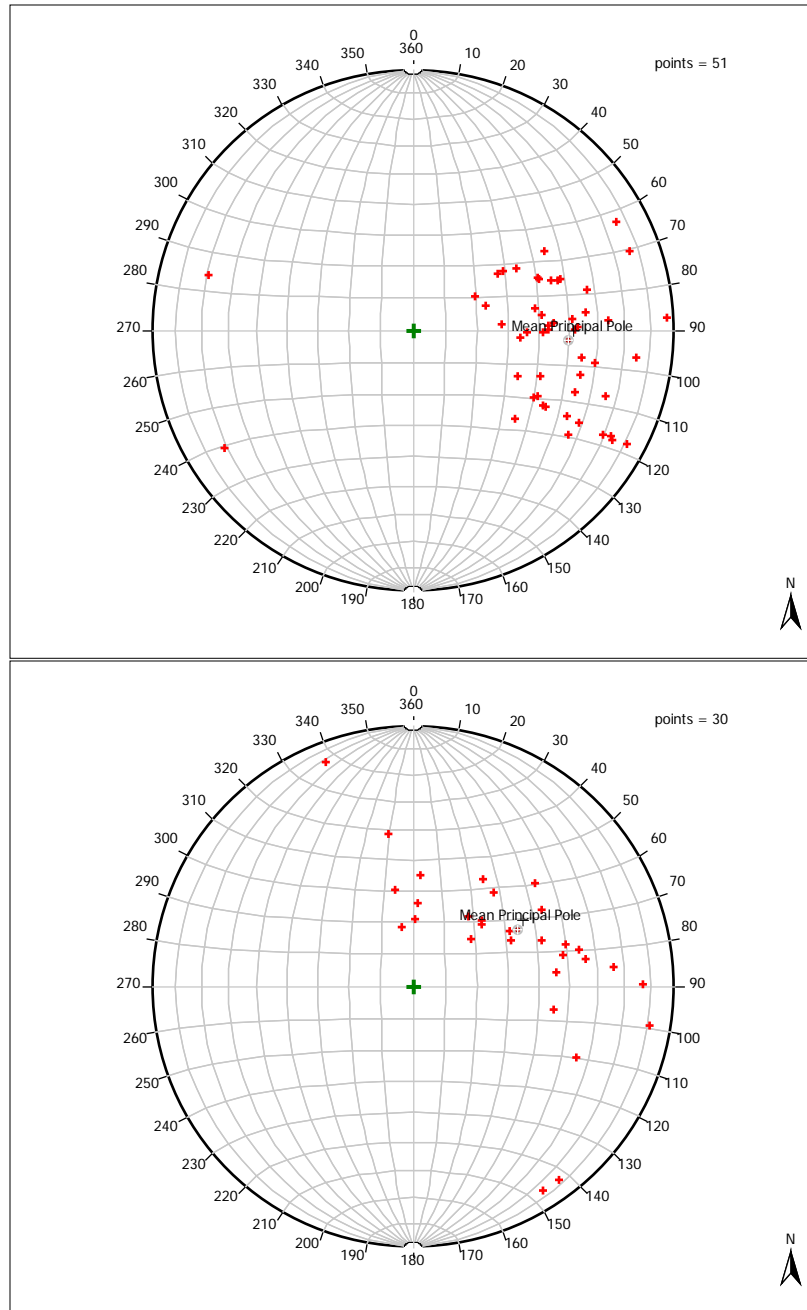


Figure 35. Stereonets of poles to planes of the S1 strike and dip orientations collected in the field (top) and extracted from the TLS-derived terrain model (bottom) of the Clair Camp Structure. Both stereonet show dominantly west dipping foliation that scatters from shallow to steep dips as a result of the fold in foliation. The mean principal pole for the orientations obtained from the TLS-derived terrain model plunges 65° toward 075° , whereas the mean principal pole from the field orientations plunges 40° toward 090° . The stereonet of terrain model-derived orientations from the Clair Camp Structure (bottom) is more scattered along a great girdle than the orientations from the field, providing a clearer definition of the fold orientation for this structure.

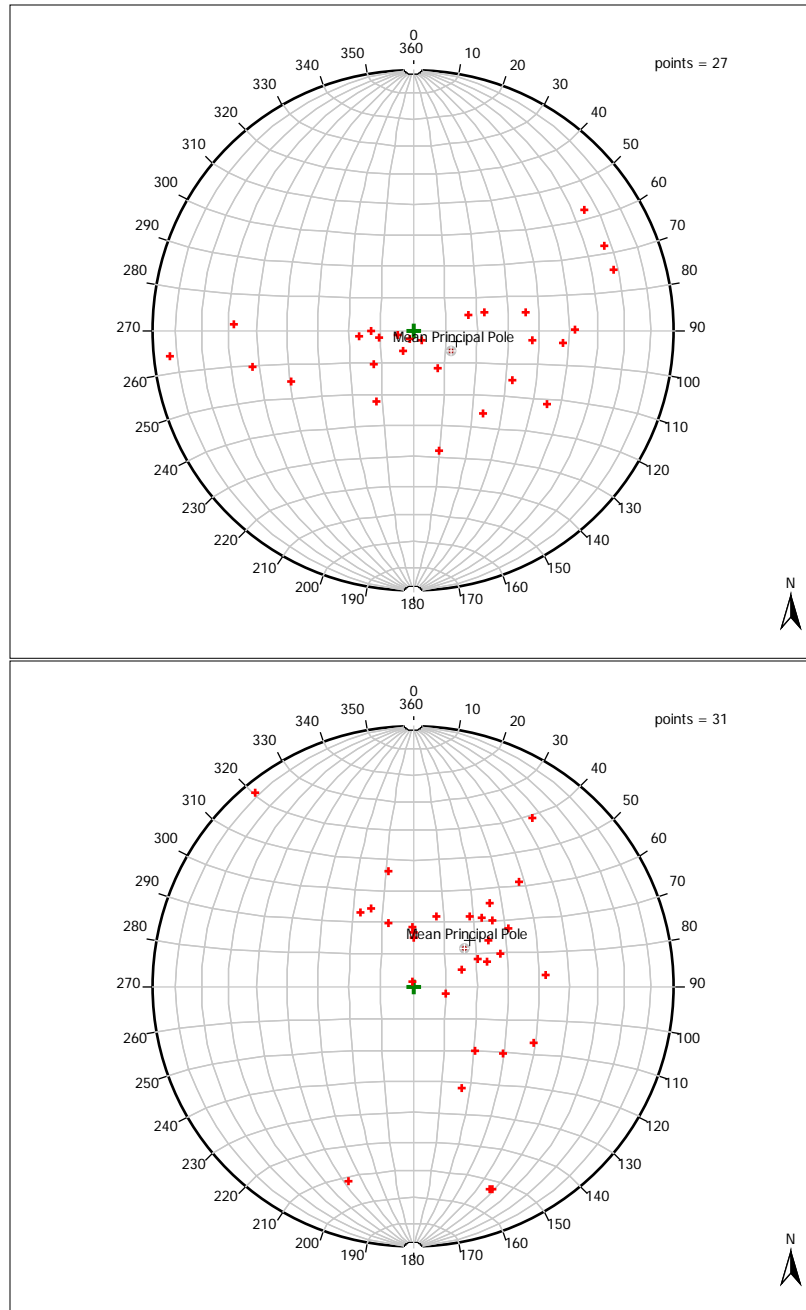


Figure 36. Stereonets of poles to planes of the S1 strike and dip orientations collected in the field (top) and extracted from the TLS-derived terrain model (bottom) of the Noonday Structure. The mean principal pole from the field orientations from the Noonday Structure is similar to the mean principal pole of the terrain model-derived orientations. The field orientations plunge 75° toward 090 while the terrain model-derived orientations show a mean principal pole that plunges 75° toward 080. The TLS-derived measurements deviate significantly from the field orientations. Independent measurements of small scale folds and fabrics through the area demonstrate that the field data give the proper fold orientation, raising questions on the source of errors in the TIN analysis.

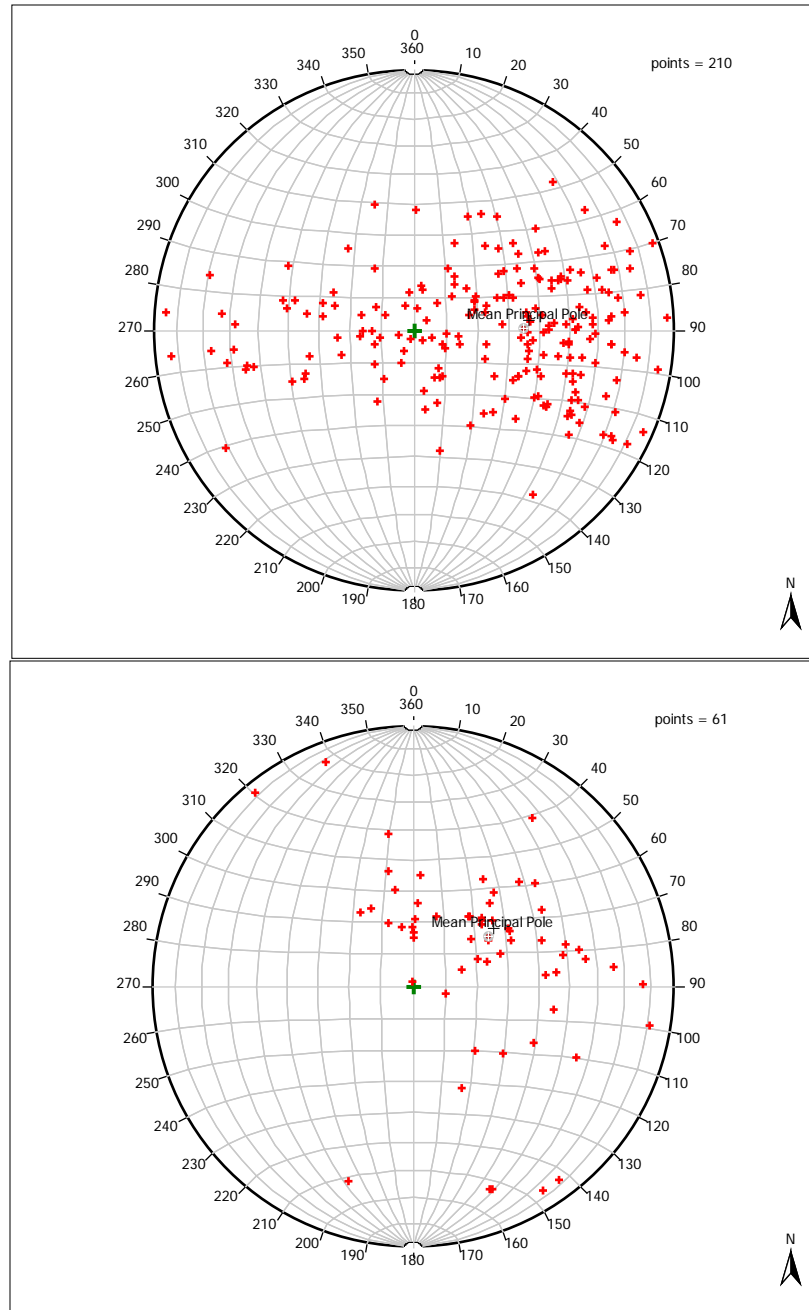


Figure 37. Stereonets of poles to planes of the S1 strike and dip orientations collected in the field (top) and extracted from the TLS-derived terrain model (bottom) representing the entire mapped area of Pleasant Canyon. The mean principal pole from the field orientations is similar to the mean principal pole of the terrain model-derived orientations. The field orientations plunge 55° toward 090 while the terrain model-derived orientations show a mean principal pole that plunges 65° toward 075. The TLS-derived measurements deviate significantly from the field orientations may reflect measurement bias in the field and attempting to obtain measurements on cliff faces from the terrain models.

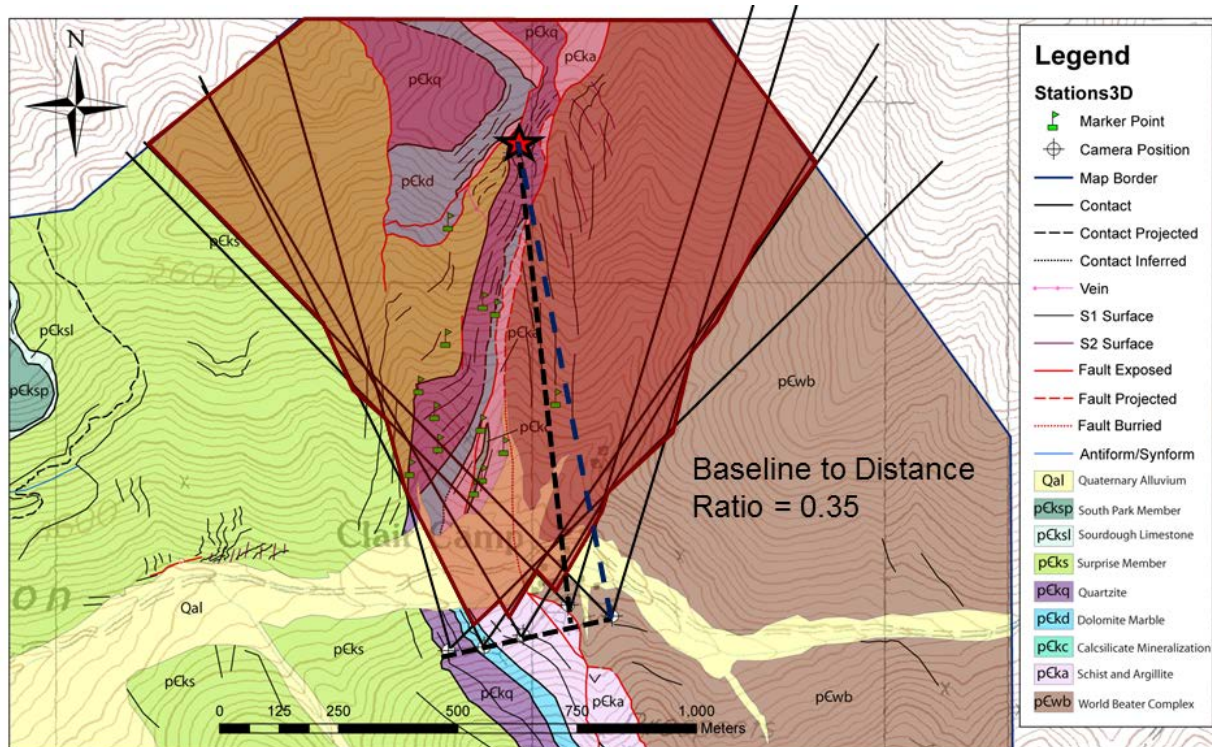


Figure 38. Geologic map of the Clair Camp Structure showing the baseline-to-distance ratio for the photogrammetric array. The angular field of view for each camera position is assumed to be 60° for a 35 mm focal length. Each field of view is oriented so that the optic axis (dashed blue line) is aligned to the farthest feature in the scene (represented by a star). The shaded red area represents the stereo coverage of the array. The baseline is a black dashed line connecting the two most distance camera positions (white circles with crosses) in the array, and a black dashed line is drawn perpendicular to the baseline to the farthest feature producing a baseline-to-distance ratio of 0.35.

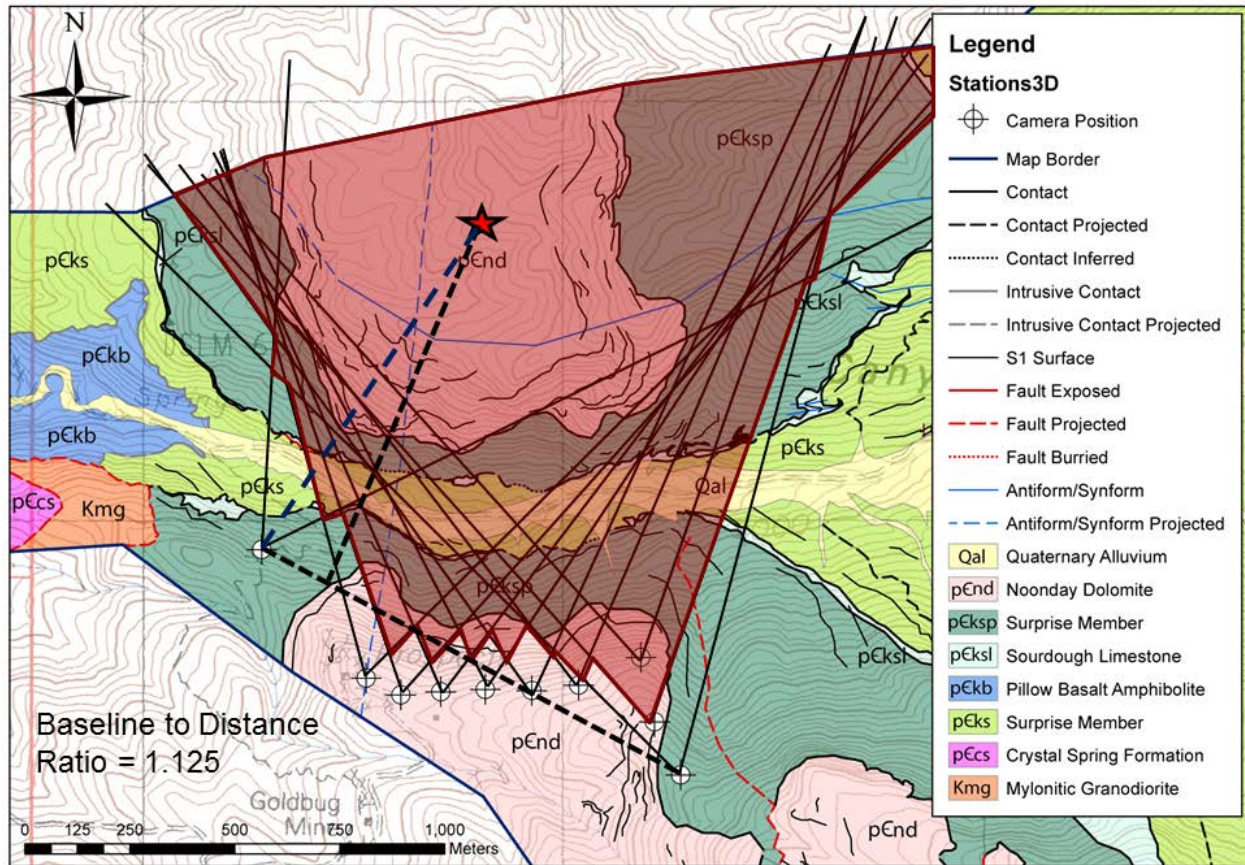


Figure 39. Geologic map of the Noonday Structure showing the baseline-to-distance ratio for the photogrammetric array. The angular field of view for each camera position is assumed to be 60° for a 35 mm focal length. Each field of view is oriented so that the optic axis (dashed blue line) is aligned to the farthest feature in the scene (represented by a star). The shaded red area represents the stereo coverage of the array. The baseline is a black dashed line connecting the two most distance camera positions (white circles with crosses) in the array, and a black dashed line is drawn perpendicular to the baseline to the farthest feature producing a baseline-to-distance ratio of 1.125.

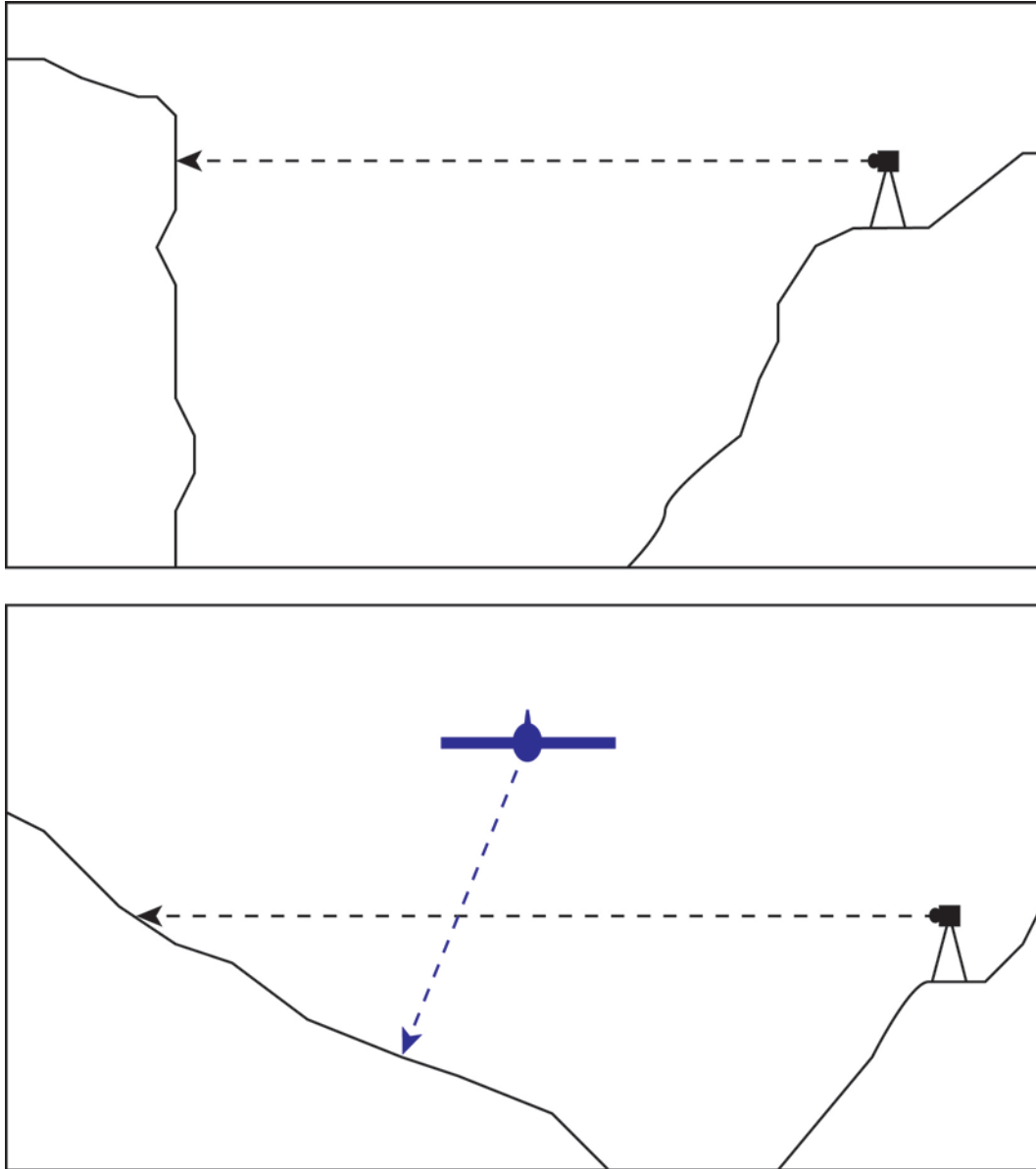


Figure 40. Diagrams showing simplified camera orientations for the Noonday Structure (top) and the Clair Camp Structure (bottom). For the Noonday Structure the optic axis of the camera (dashed black line) was generally oriented perpendicular to the feature being captured. For the Clair Camp Structure, the optic axis of the camera was oriented oblique to the feature being captured. In order to orient the optical axis of a camera perpendicular to the surface of features, such as the Clair Camp Structure, the photographs (or LiDAR scans) must be taken from the air as shown by the blue dashed line.

Plates

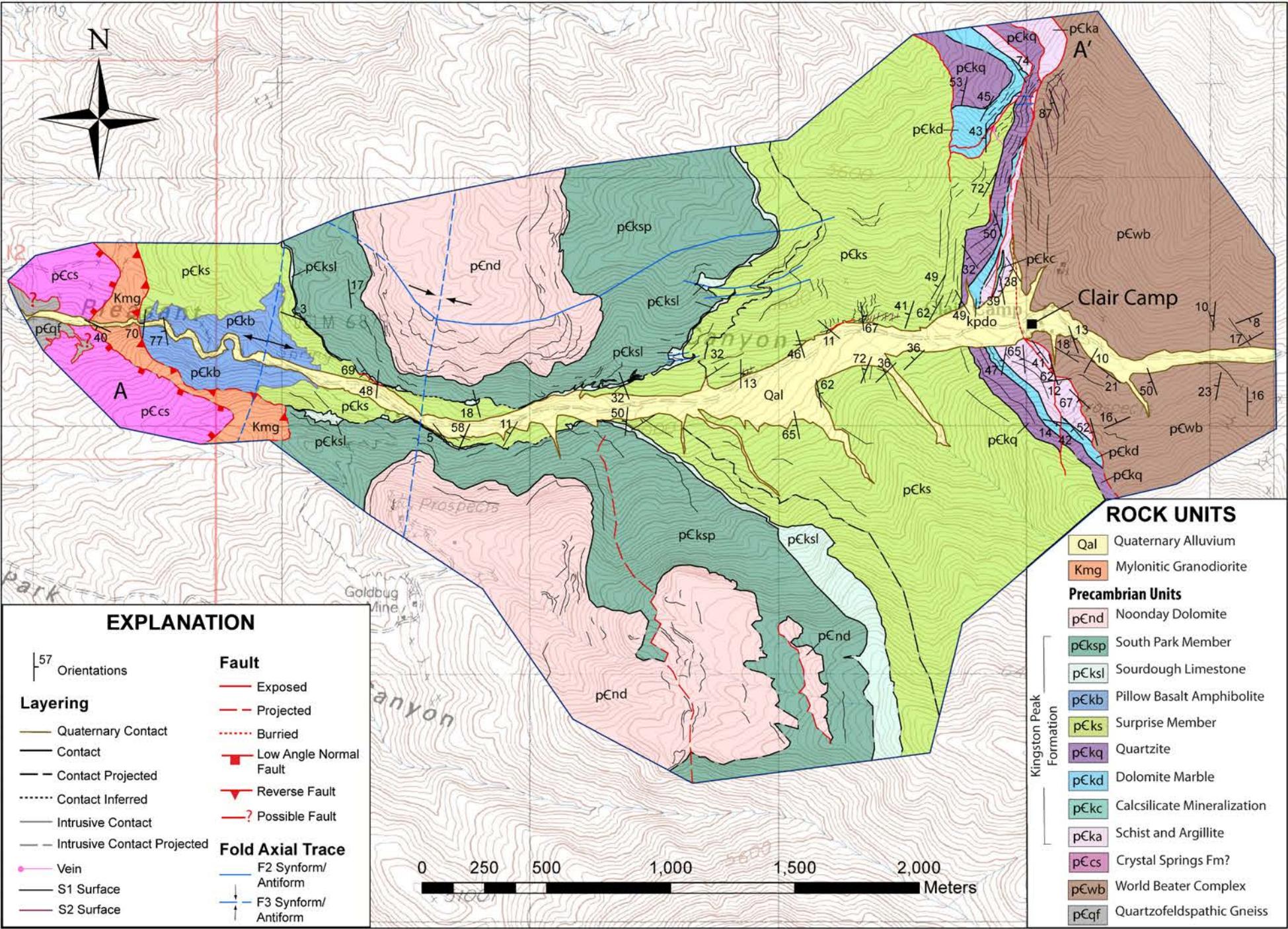


Plate 1. Geologic map of Pleasant Canyon created using the digital mapping techniques described in the text and finalized using ArcGIS. Refer to text for a detailed description of map units and structure.

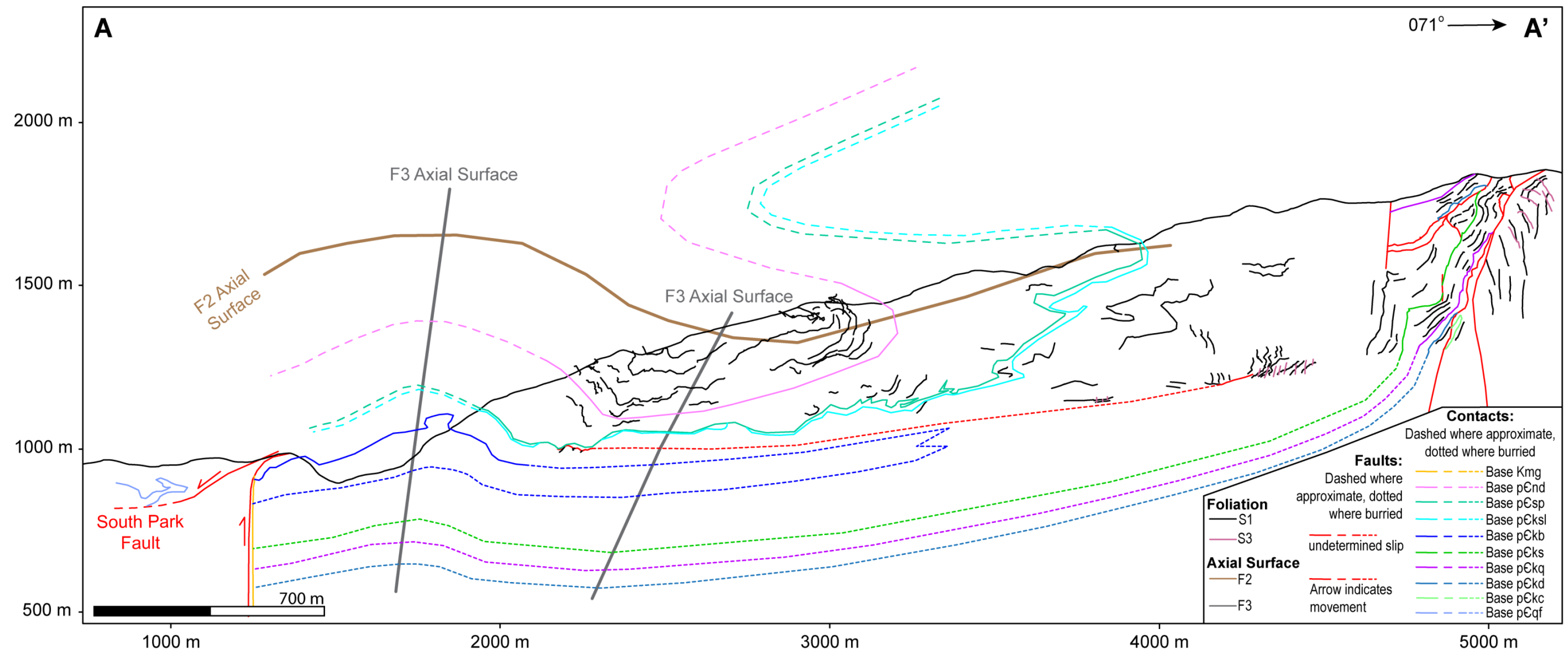


Plate 2. Cross-section of Pleasant Canyon from A-A' on the map (Plate 1). All contacts represent the base of units and the colors of these contacts are the same as the colors on the map (Plate 1). F2 and F3 axial surfaces are labeled and S1 and S3 foliation traces (thin black lines and dark pink lines, respectively) are also present. Kmg = Mylonitic granodiorite, pCnd = Noonday Dolomite, pCksl = Sourdough Limestone Member of the Kingston Peak Formation, pCkb = Basalt Amphibolite unit within the Kingston Peak Formation, pCks = Surprise Member of the Kingston Peak Formation, pCkq = Quartzite unit within the Kingston Peak Formation, pCkd = Dolomite Marble unit within the Kingston Peak Formation, pCkc = Calc-silicate Mineralization within the Kingston Peak Formation, pCqf = Quarzofeldspathic Gneiss.

Appendix 1

Animation 1. Video of the photogrammetrically-derived terrain model of the Clair Camp Structure with 3D interpretations viewed in *I-Site*. Refer to Figure 20 for the legend. File name: Animation1.avi. YouTube link: <https://youtu.be/BYi0PzCl-v8>.

Animation 2. Video of the TLS-derived terrain model of the Clair Camp Structure with 3D interpretations viewed in *I-Site*. A field photograph is draped onto the TIN in order to make these interpretations. Refer to Figure 21 for the legend. File name: Animation2.avi. YouTube link: <https://youtu.be/yRCICZiS54M>.

Animation 3. Video of the photogrammetrically-derived terrain model of the Noonday Structure with 3D interpretations viewed in *I-Site*. Refer to Figure 22 for the legend. File name: Animation3.avi. YouTube link: <https://youtu.be/QXkPY0QwHR8>.

Animation 4. Video of the TLS-derived terrain model of the Noonday Structure with 3D interpretations viewed in *I-Site*. Two field photographs are draped onto the TIN in order to make these interpretations. Refer to Figure 23 for the legend. File name: Animation4.avi. YouTube link: <https://youtu.be/ZomnQzm6cGc>.

Animation 5. Video of the visual comparison between the marker-less photogrammetrically-derived TIN of the Clair Camp Structure (blue), the TLS-derived TIN (pink), and the photogrammetrically-derived TIN of the Clair Camp Structure that utilized marker points (green). The TLS-derived TIN is used as a reference. The marker-less photogrammetrically-derived TIN is located well above the TLS-derived TIN, while the photogrammetrically-derived TIN that utilized marker points is situated slightly underneath the TLS-derived TIN of the Clair Camp Structure. This video was made using *I-Site*. File name: Animation5.avi. YouTube link: https://youtu.be/V01I2_21agY.

Appendix 2

Instructions for making shapefiles from geoclino data:

1. Make an Excel spreadsheet with latitude, longitude, strike, dip, station number, etc.
2. Select “Print Area” and only include the values in the table that you want imported into *ArcMap*. SAVE.
3. Open *ArcMap* add your shapes to set the projection for the dataframe.
4. File → Add Data → Add XY Data → Select your excel file, define longitude as “X” and latitude as “Y”. NOTE: lat/long needs to be converted to decimal degrees before doing this (the geoclino stores lat/long in degrees and minutes; decimal degrees = degree + (minute/60). Keep in mind that longitude (X) is negative in the NW hemisphere.
5. Click “edit” to select coordinate the system that *ArcMap* is going to read from your table. Geoclino data is in WGS1984 so click the GCS folder → “World” folder → WGS1984
6. Click “OK” on all windows.
7. The table shows up in the table of contents in *ArcMap*. Right click on it → data → Export Data as a shapefile and click “use the same coordinate system as **the data frame**” and this will ensure that your new shapefile is in the same coordinate system as the rest of your data. Click “OK”.
8. A window will pop up asking you if you want to add the shapefile to the data frame, click “yes” and it should show up correctly on the map.

Agisoft PhotoScan notes

General information:

1. When taking photographs, set your camera so that it stays at the same zoom, 35 mm is the best option.
2. Take lots of overlapping photographs.
3. Do NOT take panoramic photographs. They can generate unpredictable or even bad results. To cover a large area, take overlapping photographs scanned across a scene, making certain that each photograph has at least 50% overlap with the preceding photograph in the group. Similarly, if vertical relief exceeds the camera field of view, suites of photographs taken at a site should also overlap vertically 50% or more.
4. All major operations in *PhotoScan* are found in the “Workflow” section of the toolbar.

Ground control and markers:

1. GPS positions for where you were standing when you took the photographs (Camera Positions) can be added into your *PhotoScan* project by going to panes → ground control. NOTE: If you used a camera that records the GPS location of where you took the photograph, then the GPS coordinates will automatically be placed in the “ground control” tab when the photos are added (I highly recommend one of these cameras if you are doing photogrammetry as it will save time).

- a. The “Markers” pane is where you enter the GPS coordinates for the marker points collected in the field using the laser rangefinder (must tell the program where each marker point is in every single picture you added).
- b. Open photograph → right click → create marker, input its GPS and place the marker point at its proper location in the photograph.
 - i. Please refer to the “Orthophoto DEM Ground Control Agisoft Tutorial” for more detailed instructions on how to add markers and place markers properly.
 - ii. Set reference frame in *PhotoScan* to your coordinate system (for example, NAD83 Zone 11).

The general process for creating a dense point-cloud:

1. Add photos.
2. Input camera information/settings (select “Camera Calibration” from the Tools menu).
3. Mask the sky and unwanted foreground out of photos (‘add selection’ to complete the mask). Use the lasso tool to do detailed masking.
4. Add GPS for the camera positions and marker points.
5. “Workflow” → align photos and chose setting appropriate for your project.
6. Quality-check (QC) marker points and camera positions at this stage. If there are any marker points with an error >100 m (or significantly greater than the rest of the errors) eliminate those marker points and redo the alignment. Similarly, if there are any camera positions with significant error, correct the error or delete the position and redo the alignment. Removing erroneous camera positions are marker points will improve the total error of the model.
7. ‘Workflow’ → build dense point cloud, here you may want a high resolution, but the higher you make it the longer the process will take (depending on the machine being used, this process can take as long as 8 days).
8. Save project and export your dense point cloud as a TXT file (XYZ points in the drop down in the bottom right corner of the window). NOTE: you MUST add “.txt” at the end of your file name in the file name bar for it to save properly. Make sure to save the TXT file with the correct coordinate system selected.

Other operations can be performed in *PhotoScan* such as building meshes, DEMs, etc. For more detailed descriptions see the *Agisoft PhotoScan* Tutorials.

ArcMap tips:

Reprojecting the coordinate system for images:

1. In *ArcMap* go to the red toolbox → Data Management → Projections and Transformations → Raster → Project to raster.

2. To select the correct coordinate system for the output click “select” → projected coordinate systems → UTM → your coordinate system (example, NAD1983) → click on your projection (example, NAD1983 UTM zone 11.prj). Make sure that the file name in the output has “.tif” at the end.

Strike/dip symbology:

1. Go to “Symbology” for your strike/dip shape → advanced → rotation → in drop down select “strike”.
2. Label feature by “dip”.

Exporting points to ASCII:

1. Go to the red tool box → utilities → export feature attribute to ASCII and then select the point shape you want and name it (selection is actually from a file not from the map itself).

Obtaining ArcWeb images:

1. Open *ArcMap* and go to ArcGIS online → world imagery → add
2. Zoom to your area of interest. Zoom in as much as you can just before the resolution starts to look fuzzy (1:10,000 recommended) → export map as TIF and set home view on world imagery to the same view you just exported → input your TIF you just made. This will overlay the image you just exported as a TIF on top of the world image you took it from. This is for georeferencing purposes. Essentially, you are georeferencing the image to itself.
3. Open the georeferencing tool bar and begin picking points on the image to use as markers starting with a point on your TIF. Choose at least 5 points, you can make due with less, but I find that it is more accurate if you put a marker in each of the 4 corners and then one in the center of the TIF. When you are finished you must ‘rectify’ the image (this can be found in the georeferencing drop down menu). By rectifying you will save the image, but as a precaution I recommend exporting your now georeferenced TIF just in case.
4. Open a new *ArcMap* and bring in your georeferenced TIF and convert it to the coordinate system you need (currently it is in WGS19854 world). Instructions for reprojecting coordinate systems for a raster is described above.

These images have good resolution (resolution varies across the globe) and can be used as an alternative to aerial photos for mapping.

RiScan Version 1.8.0 notes:

1. I tiled the TLS data following instructions in a video prepared by K. Williams of UNAVCO. Tiling allows you to split the data into manageable tiles that are sized however big you want them. My data was 500 m X 500 m, which cut down the file size enough for *Maptek I-Site* to handle with ease. After the tiles are created, export them as an ASCII file using “global

coordinates” and select “RGB” information to be maintained. This will ensure that coordinates and color of your tiles are exported properly. If your coordinate system is UTM make sure your export units are in meters.

- a. I did not use *RiScan* to build TINs for this study because it was too slow (only 32 bit).

Maptek I-Site notes:

Basic procedure for building a 3D model from scans and/or point-clouds:

1. Import data (LiDAR tiled scans and/or Photogrammetry point-clouds of an outcrop). They will be saved in a folder called “Scrapbook” for point-clouds and “Scans” for scans. If your data is in UTM coordinates make sure you select meters as your units for this data.
2. Clean up data using the lasso select tool which allows you to free-hand select points you do not want such as floating/stray points and sky. Hold mouse button 1 and draw a polygon around the points you want to delete → press “delete” on keyboard once all the objects you selected turn yellow (which signifies that they are selected).
3. Filter data. NOTE: this will decrease the resolution of your data, but it will also decrease the file size and make the data more manageable. If your data has excessive vegetation or the file size is too large to manipulate effectively on the machine you are using, then this step may be necessary. However, if your data does not include vegetation and the machine you are working on is capable of handling large files, then this step is not necessary.
 - a. You can filter the data by any size square you want and it depends on your data, so this may require some tinkering. I used a size of 1.5 m, the lowest setting recommended by the “Help” menu, and it worked well in maintaining enough resolution but also cutting down file size. This will cut down the number of points by an order of magnitude and will help eliminate any stray points you may have missed during freehand editing.
4. Build a surface model by running a topographic triangulation found under the “Model” tab on the toolbar. This will triangulate by looking at your model in map view. For cliffy overhanging outcrops use spherical triangulation, which allows you to set the look point and look direction by clicking in the viewing window to denote where each point goes. You can modify this by highlighting the input box within the triangulation dialog box and clicking a new point in the view.
5. Despike the model by running a despiker, found in “Edit” on the toolbar. If it cannot remove the spikes because there are too many, you may want to remove them manually with the lasso or filter the data by a larger size filter.
6. Fill holes, this will fill any holes created after spikes were removed (also found in “Edit”).

7. Now you are done and you can go on to draping images on your model or drawing contacts right away if the point cloud resolution was good enough. The model is saved in the folder called “Surfaces”.

NOTE: The time triangulation takes depends on the size of the model, but expect it to take at least an hour for point-clouds or scans that contain 10s of millions of points. Despiking takes about as much time as triangulation.

Draping images:

1. Import the image you want to drape. NOTE: Draping permanently attaches a picture to a model, so I suggest making a copy of your model before doing this.
2. If it is a regular photograph (not panoramic) use the multipoint option and you must choose at least 8 points. First select the point you want to match on the photo, then go to the model and select that same point. Keep doing this until you have 8. Try to pick on prominent features such as ridges or boulders, because those can easily be found on the surface model even if the image quality of the model is poor. Try to get a good spread across the area that the photograph will cover. You may need more than 8 points depending on whether or not *I-Site* successfully drapes the photograph in the proper location. This can be verified before finalizing the drape by turning the view points on and all the points you selected should converge on a single point that represents where the photograph was taken. If these lines do not converge, then you may have to add more points and/or delete some points that you already placed if they have large errors.
3. When satisfied, apply the drape. NOTE: the photograph will appear skewed at oblique angles, this is normal because the photograph is 2D.
4. To adjust the color of the image go to the “color” tab → adjust image color → check the box for “enhance detail” and make any other adjustments that you wish → OK.
5. You can drape multiple photographs on the same model to cover different areas of the surface. You just have to go through the process above one photograph at a time.

NOTE: Depending on how difficult it is to get the points to converge, this process should take about 20 min.

NOTE: If your model is derived from photogrammetry you may not have to drape a photograph on it because it maintains the detail from the photographs used to create the point-cloud.

Generating strike/dips from a TIN:

1. Go to the “geotechnical” tab → query strike/dip. Then to actually obtain the strike and dip you need to select some points (at least three since this is essentially a 3 point problem).

2. Use the point select tool and select points that represent a surface → hit enter and it will create a strike and dip. NOTE: QC the orientation to make sure it took a strike dip of the bedding surface and NOT the façade surface of the bed.
3. Strike/dips will be saved in the “CAD” folder in the data pane.

Drawing linework:

1. Go to the “Create” tab and select “line”. This will allow you to draw lines on your model.
2. Start drawing a new line by clicking along (just like digital mapping). To finish a line press enter on the keyboard and it will be saved in the folder called “CAD”.
3. Rename the line you just created so that you know what it is.
4. This line is NOT projected onto your surface. If you move the model around you will notice that the line appears to weaves in and out of the surface while still following your drawn path. Depending on how many vertices you drew, the line may stay relatively close to the surface, enough to not have to project the line to the surface. If you decide to project it, keep in mind that this program only projects in the ‘Z’ direction, so if your lines are drawn on a façade with a lot of cliff overhangs then projecting the lines tend to not project accurately and it generates a zig-zag pattern.
5. If you want to export your lines to be viewed in another 3D program like *MOVE* or in *ArcGIS*, then export them as DXF files.
6. To change the color of your lines go to “Color” tab on the toolbar → uniform and change the selected lines to the color you want.
7. To increase the thickness of the lines drawn, go to “File” → Preferences → View window → Properties → here you have the option to set the line width for all lines in the view. NOTE: the “Properties” menu is also where you can change the units (e.g. feet, meters, etc.), the background color in the viewing window, etc.

Analyzing two surfaces:

1. Try cropping the 2 surfaces you want to compare down the same size and covering about the same area. Depending on the situation you may have to eye-ball it by tiling two views each containing one of the surfaces you want to compare. If they are already sitting on top of each other, then you can open them in the same view and crop them.
2. Go to the “Geotechnical” tab in the toolbar → ‘set acquisition date’ you want to select your surface and give it an acquisition date. The surface that you are using as the reference should have an older date, the younger surfaces is the one being analyzed for surface change (for our purposes these dates are arbitrary, but they need to be set older and younger for this to work). NOTE: make a copy of the surface you are analyzing because the result is going to color code that surface permanently.

3. Go to “Geotechnical” tab → ‘analyze surface change’ → select your two surfaces then run it. Should take about 20 min to an hour depending on the size of these surfaces.
4. The result is a colored surface that shows the \pm difference between the older surface and the younger surface. The color is projected onto the younger surface and you can change the settings for the contour of these colors in the result pane. NOTE: the \pm difference is in the Z direction only; this is not an absolute surface change analysis.

Registering point-clouds:

1. To register one point-cloud to another, go to the “Registration” tab. Under this tab you can register the data by dragging and dropping the reference point-cloud into the reference section, and the dragging and dropping the point-cloud you want to move into the registration section. This process should take 20 min to an hour depending on the size of the point-cloud.

NOTE: this process only works on point-clouds, scans and surfaces cannot be registered.

Views:

2. To view multiple windows at once go to the “View” tab on the toolbar and select ‘tile’.
3. To view multiple windows and tie their motions together (so if you rotate or zoom in one window you will rotate and zoom by the same amount in the tied window) go to the “View” tab and select ‘tile and tie’.

Other information:

1. In order to do some of the *Maptek I-Site* work, a machine with a good amount of RAM and processing power as well as a good graphics card is required.
2. You can make movies in *I-Site* by animating key frames.
3. Selections are made by highlighting an object in the data viewing window. Selections for certain processes require you to click and drag into an input bar in the dialog box. To do this you must click and drag using the scroll button (mouse button 2).
4. If you are constantly freezing the program, then only work on prepping and editing the data for about an hour and then close the program. This program has an autosave which overloads the memory cache quickly. The best way to keep it running at a decent speed is every time you finish a major edits or operations (certainly before you run any type of triangulation or analysis operation) close the program first and re-open the project to clear the memory cache. Once it is open again, perform the operation.

MOVE notes:

1. *MOVE* is a good program for making cross-sections. Shapefiles can be imported as well as DEMs (for this project I downloaded a DEM from the USGS website). Shapes can be draped onto the DEM and cross-sections (the process of making cross-sections uses the DEM to create the topographic profile). The accuracy of draping lines will depend on the resolution of the DEM used.
2. Faults and intrusions are generally projected normal to the section. Bedding is projected using the overall trend/plunge of the area obtained from stereonet plots.
3. Strike/dips and trend/plunge from digital mapping can be imported into *MOVE* with correct positions and orientations as an ASCII file, which can be exported from *ArcMap*. Once the ASCII file is imported, set the data attribute columns to correspond to strike, dip, latitude, longitude, etc. by clicking on the column header and selecting the proper column heading.
4. Stereonet analysis is in the “data/analysis” tab on the toolbar → “SCAT”. Use the red free selection tool (left of map view window) to select the orientations you want. You must hold down the “shift” key as you draw select. The selection tool looks like an arrow with a “+” sign.

Appendix 3

The MATLAB script used to calculate total vector offset between photogrammetrically-derived TINs and TLS-derived TINs. The code requires the user to load the CSV files that contains the coordinates for the points located on the photogrammetrically-derived TIN and the TLS-derived TIN. There are four CSV files total, two for each structure in this study. The example script below is for the Clair Camp Structure.

Clair Camp Structure files:

1. TLS Coordinates = ClairCampLidarm.csv
2. Photogrammetry Coordinates = ClairCampPhotogrammetrym.csv

Noonday Structure files:

1. TLS Coordinates = NoondayLidarm.csv
2. Photogrammetry Coordinates = NoondayPhotogrammetrym.csv

MATLAB code file:

1. Clair Camp Structure = offset_jab_ClairCamp.m
2. Noonday Structure = offset_jab_Noonday.m

```
%Clear previous operations and command window
clear
clc
clf
load('ClairCampLidarm.csv')
load('ClairCampPhotogrammetrym.csv')
%simplify variable names
L = ClairCampLidarm
P = ClairCampPhotogrammetrym
%The following calculations will result in a 10x1 matrix that represents
%the distance between each of the 10 points selected from Lidar and
%Photogrammetry in 3D space
%Column 1 is the easting, column 2 is the northing, and column 3 is
%elevation for both L and P, the units are feet for all values

%Take the difference between L and P to get the coordinates of the vector
%between each point
difference = L-P
%Square each individual slot in "difference" matrix
squared = (difference.^2);
%add each row in "squared" together, the result will be a 10x1
%matrix
```

```

added = (squared(:,1)) + (squared(:,2)) + (squared(:,3));
%Take the square root of "added"
distance = sqrt(added)
%Take the average of the distance data to get a general answer for how far
%off the photogrammetry surface is from the Lidar surface. Get the max and
%min offset distance as well
average = mean(distance)
maximum = max(distance)
minimum = min(distance)
%plot data in 3D, start with a scatter of the points
scatter3((P(:,1)),(P(:,2)),(P(:,3)), 'r'); hold on
scatter3((L(:,1)),(L(:,2)),(L(:,3)), 'b'); hold on
xlabel('Easting (m)');
ylabel('Northing (m)');
zlabel('Elevation (m)');
%connect the photogrammetry point to the corresponding lidar point. Do this
%for all 10 points using a loop
marker = length(P);
for step = 1:marker
x = [(P(step,1)), (L(step,1))];
y = [(P(step,2)), (L(step,2))];
z = [(P(step,3)), (L(step,3))];
plot3(x,y,z)
hold on
end
print -dpdf Jades_3DPlot_ClairCamp_new.pdf
%The next set of calculations will obtain the direction of the distance
%vector expressed as an angle instead of coordinates (components), which is
%what the variable "difference" represents

```

Curriculum Vita

Jade Brush graduated from California State University, Fullerton in 2011 with a Bachelor's degree in Geological Science. As an undergraduate student, Jade studied exhumation of the Chugach Mountains in southern Alaska using zircon fission-track ages and wrote an undergraduate thesis on the subject. Her undergraduate research was incorporated into a paper by Arkle and others (2013) published in *Geological Society of America Bulletin* entitled, "Focused exhumation in the syntaxis of the western Chugach Mountains and Prince William Sound, Alaska". During her senior year as an undergraduate, Jade received the Outstanding Academic Achievement Award for having the highest GPA in the Department of Geological Science. In the fall of 2012, Jade continued her studies by pursuing a Master of Science degree at The University of Texas at El Paso, and in 2013 received the Chevron Earth Sciences Scholarship to support her graduate studies. Over the next two years, Jade has had two summer internships in the oil and gas industry. The first internship was with ConocoPhillips in the summer of 2013, and second was with Anadarko Petroleum Corporation in the summer of 2014. Upon graduation from The University of Texas at El Paso Jade will be working as a summer intern for the mining company FreePort-McMoRan Copper and Gold.

Permanent address: 13753 Fremont Street
Trona, CA 93562

This thesis was typed by Jade Ashley Brush.